# WAVE PROPAGATION IN HETEROGENEOUS MEDIA:MATHEMATICAL AND NUMERICAL MODELING

André Nachbin

# WAVE PROPAGATION IN HETEROGENEOUS MEDIA: MATHEMATICAL AND NUMERICAL MODELING*

ANDRÉ NACHBIN§

**Abstract.** These notes focus on water waves in heterogeneous media, namely pulse shaped waves propagating over a region of highly variable depth. Through the mathematical modeling, at the level of equations, we show how diferent types of waves can arise: hyperbolic, dispersive, linear or nonlinear. The applications for these types of long waves are usually from Geophysics: in particular oceanography and meteorology. Here the emphasis is on coastal waves related to Physical Oceanography. The complete mathematical formulation is presented together with different asymptotic simplifications at the level of the partial differential equations (PDEs). The asymptotic analysis of solutions is also described for the regime where long waves propagate over rapidly varying topographic heterogeneities, which are modeled through rapidly varying coefficients in the PDEs. Finally numerical models are described together with scientific computing simulations related to the asymptotic theory presented. In particular these experiments exhibit fascinating physical phenomena such as the **apparent diffusion** and **time-reversed refocusing** for waves in a randomly varying environment. We briefly indicate how probabilistic modeling comes into playing an important role.

**Key words.** Linear and nonlinear waves, inhomogeneous media, asymptotic theory, apparent diffusion, time reversal.

**AMS subject classifications.** 76B15, 35Q99, 60F05.

## 1. MODELING: ASYMPTOTICS AT THE LEVEL OF EQUATIONS.

**1.1. Introduction.** These notes were assembled from several articles published in the last few years [57, 51, 52, 53, 28, 29, 30, 2, 3]. It is a great pleasure to start by acknowledging the collaboration of two former students W. Artiles (Institute of Theoretical Physics, São Paulo, Brazil), J.C. Muñoz (Dept. of Mathematics, Universidad del Valle, Cali, Colombia) and of two great friends J.P. Fouque (Dept. of Mathematics, North Carolina State University, USA) and J. Garnier (Jussieu, Paris VII, France).

Waves in heterogeneous media is a field of great mathematical interest and, not surprisingly, applicable to many technological and environmental problems. If we keep our attention to Geophysics we have applications in the atmosphere, hydroshpere and lithosphere. In the lithosphere one may think of acoustic waves, regarding the seismic probing of the Earth's subsurface [11]. This is of interest to the oil industry. In the atmosphere and hydrosphere we may take the heterogeneous medium as being the topography. These physical applications, for long wave interactions with topography, range from coastal surface waves [49] to atmospheric flows over mountain ranges [5, 23].

In these lectures notes we will focus on surface coastal waves. Waves on the surface of an ideal fluid, under the force of gravity are governed by the Euler equations. Nevertheless in both engineering applications as well as laboratory scales, the full Euler equations appears more complex than necessary. Very often this system, for the entire fluid body, can be simplified to more tractable reduced surface models, when restricted to specific physical regimes. Under this modeling strategy Boussinesq-type equations, which include the lowest order terms regarding nonlinearity and dispersive effects, have been shown to provide an accurate description for wave evolution in

*Instituto de Matemática Pura e Aplicada, Est. D. Castorina 110, Jardim Botânico, Rio de Janeiro, RJ 22460-320, Brazil, nachbin@impa.br

coastal regions. The first set of equations valid for variable depth was derived by Peregrine [63] in 1967. The model is valid under the mild slope hypothesis.

Very recently there has been a great amount of research regarding additional modeling issues, namely in improving Boussinesq-type models as for example in [40, 44, 45, 60, 67, 46]. But all of these consider flat or slowly varying topographies. For very general topographies a terrain-following Boussinesq model was developed by Nachbin [57] in 2003. The model allows for multiply-valued topography profiles. This model was analyzed in [51, 52, 28, 30]. Existence and uniqueness for a variable coefficient Boussinesq system of equations was first given by Quintero and Muñoz in 2004 [65].

We also use ideas from Nwogu [60] and generalize the model given in [57]. We show how small (higher order) changes in the linear dispersion relation (over a flat bottom) become dramatically important in the presence of a highly-fluctuating topography. We present a linear dispersion analysis and validate the corresponding results both for a flat bottom and also in the presence of a variable propagation medium. In order to fully validate dispersive properties of several possible truncations, that can be made for these Boussinesq-type models, we compare them with the corresponding complete (non-truncated) model, namely linear potential theory. For the numerical validation we use a new, highly efficient numerical scheme developed by Artiles and Nachbin [2, 3]. Discrepancies observed become even more important in the *waveform inversion problem* [64], an application for determining (for example) a **tsunami's initial profile**. Here we adopt the *time reversal technique* for recompressing a long fluctuating signal, representing a highly scattered wave that has propagated for very long distances. Time reversed recompression means that, if properly backpropagated (through a numerical model), the scattered signal will refocus into a smooth profile representing the original waveform, namely that which would have been observed at the onset of the ocean disturbance.

We also outline asymptotic solution techinques for obtaining an effective behavior along the wavefront. In particular for observing the **apparent diffusion** due to disordered multiple scattering.

These notes are organized as follows:

- **Modeling: asymptotics at the level of equations**
  - Introduction
  - Formulation and background of the problem
  - Improved Boussinesq systems
  - Linear dispersive properties
- **Modeling: a fully dispersive system**
  - Introduction
  - The inviscid and incompressible free boundary problem
  - The Dirichlet-to-Neumann ($DtN$) operator
  - The Dirichlet problem on a halfplane
  - The Dirichlet problem on a corrugated strip
  - Evolution equations for weakly nonlinear surface gravity waves
- **Solution asymptotics: deterministic approach**
  - Introduction
  - The linearized terrain-following Boussinesq model
  - The linear pulse-shaping theory
  - Numerical illustration of the generalized ODA theory

- **Solution asymptotics: random approach**
  - The propagating modes of the homogeneous Boussinesq equation
  - Propagator formulation
  - Mode propagation in the fequency domain
  - Boundary values
  - Propagator
  - Probabilistic modeling and tools
  - Quantities of interest
  - Transmitted wavefront
- **Numerical models**
  - Numerical scheme for the Boussinesq models
  - Preconditioning through complex variables
  - Numerical schemes for the linear potential theory equations
  - Full versus reduced model
  - Waveform inversion by time reversal refocusing

**1.2. Formulation and background of the problem.** In this section we derive the family of reduced governing equations analised in these lectures.

When the fluid, where surface waves are propagating, can be considered as being inviscid the Navier-Stokes equations reduce to the Euler equations [49, 70]. When the free surface flow can be taken as being incompressible and irrotational it is interesting to recast the Euler equations into a potential theory framework [70]. For example in a two-dimensional flow, we can study the evolution of the velocity potential (one object) as opposed to the evolution of two objects, the horizontal e vertical velocities. As will be seen below, we can also take advantage of many theoretical aspects of harmonic functions as well as the associated complex analysis.

Let variables with physical dimensions be denoted with a tilde. Then the formulation through the velocity potential $\tilde{\phi}$, where $(u, v) \equiv \nabla\phi$ is the velocity vector, is given as

$$\tilde{\phi}_{\tilde{x}\tilde{x}} + \tilde{\phi}_{\tilde{y}\tilde{y}} = 0 \quad \text{for} \quad -\tilde{H}(\tilde{x}) < \tilde{y} < \tilde{\eta}(\tilde{x}, \tilde{t}), \qquad -\infty < \tilde{x} < \infty,$$

subject to

$$\tilde{\eta}_{\tilde{t}} + \tilde{\phi}_{\tilde{x}}\tilde{\eta}_{\tilde{x}} - \tilde{\phi}_{\tilde{y}} = 0,$$

$$\tilde{\phi}_{\tilde{t}} + \frac{1}{2}\left(\tilde{\phi}_{\tilde{x}}^2 + \tilde{\phi}_{\tilde{y}}^2\right) + g\tilde{\eta} = 0$$

at the free surface $\tilde{y} = \tilde{\eta}(\tilde{x}, \tilde{t})$. At the impermeable bottom topography we have a Neumann condition.

We introduce the length scales $\ell_p$ (a typical pulse width or wavelength), $h_0$ (a typical depth), $a_o$ (a typical wave amplitude), $\ell$ (the horizontal length scale for bottom irregularities) and L (the total length of the rough region or the total propagation distance). The acceleration due to gravity is denoted by $g$ and the reference shallow water speed is $c_0 = \sqrt{gh_0}$. Dimensionless variables are then defined in a standard fashion [66, 70] by having

$$\tilde{x} = \sigma x \qquad \tilde{y} = h_0\, y \qquad \tilde{t} = \left(\frac{\sigma}{c_0}\right) t$$

$$\tilde{\eta} \;=\; a\;\eta \qquad \tilde{\phi} \;=\; \left(\frac{g\sigma a}{c_0}\right)\phi \qquad\qquad \tilde{h} \;=\; h_0\;H\left(\frac{\tilde{x}}{l_b}\right).$$

The dimensionless form of the potential theory formulation for Euler's equations with a free surface and an impermeable bottom topography [70] is

$$\beta\;\phi_{xx} + \;\phi_{yy} \;=\; 0 \quad \text{for} \quad -H(x/\gamma) < y < \alpha\eta(x,t), \qquad -\infty < x < \infty, \tag{1.1}$$

subject to

$$\eta_t + \alpha\phi_x\eta_x - \frac{1}{\beta}\phi_y = 0, \tag{1.2}$$

$$\eta + \phi_t + \frac{\alpha}{2}\left(\phi_x^2 + \frac{1}{\beta}\phi_y^2\right) = 0 \tag{1.3}$$

at the free surface $y = \alpha\eta(x,t)$. The function $\phi(x,y,t)$ denotes the dimensionless velocity potential, $\eta(x,t)$ the dimensionless wave elevation measured with respect to the undisturbed free surface $y = 0$. The dimensionless parameters $\alpha = a_o/h_o$ and $\beta = h_o^2/\ell_p^2$ measure the strength of nonlinear and dispersive effects, respectively, and the parameter $\gamma = \ell/\ell_p$ measures the ratio inhomogeneities/wavelength. We recall that in the potential theory model the fluid is assumed to be inviscid, incompressible and irrotational.

At the impermeable bottom the Neumann condition

$$\phi_y + \frac{\beta}{\gamma}\;H'(x/\gamma)\phi_x = 0 \tag{1.4}$$

is satisfied. We assume that the boundary at the bottom is described by the function $y = -H(x/\gamma)$ where

$$H(x/\gamma) \;=\; \begin{cases} 1 + n(x/\gamma) & \text{when } \; 0 < x < L \\ 1 & \text{when } \; x \le 0 \;\text{ or }\; x \ge L. \end{cases} \tag{1.5}$$

The bottom profile is described by the (possibly rapidly varying) function $n(x/\gamma)$. We point out that the topography is rapidly varying when $\gamma \ll 1$. The undisturbed depth is given by $y = -1$ and the topography can be of large amplitude provided that $|n| < 1$. The fluctuations $n$ are not assumed to be small, nor continuous, nor slowly varying.

Our main interest is to order the parameters $\alpha$, $\beta$ and $\gamma$ as powers of $\varepsilon$ and analyse the solution in the limit $\varepsilon \downarrow 0$. For example for $\alpha = \beta = O(\varepsilon) \ll 1$ we may consider solitary waves. Moreover when also $\gamma = O(\varepsilon)$ we have long waves interacting with rapidly varying heterogeneities, in this case the topography. The problem in its present form is extremely complicated. Hence simplifying the mathematical model (namely the PDE) is of interest in order to perform an asymptotic ($\varepsilon \to 0$) analysis. A key issue is not to oversimplify the model and eliminate phenomena of physical and mathematical interest.

Thus in order to simplify the geometry of the problem and enable the asymptotic analysis of equations (1.1)-(1.5), we define a symmetric flow domain by reflecting the original one about the undisturbed free surface. In this symmetric domain (figure

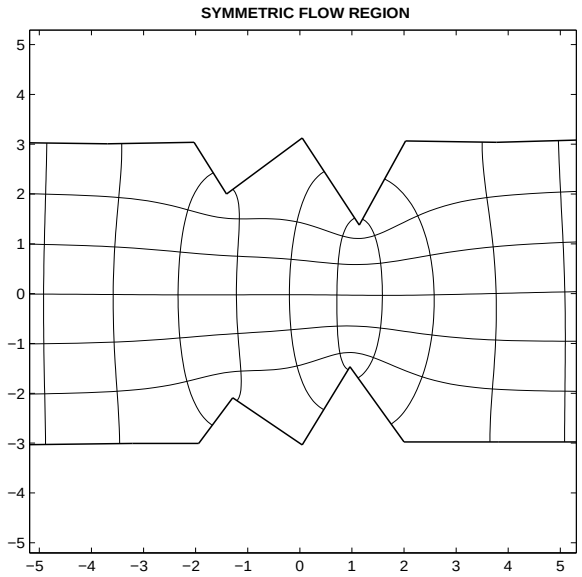


FIG. 1.1. *The symmetric domain in the complex z-plane, where* $z = x(\xi, \tilde{\zeta}) + i\tilde{y}(\xi, \tilde{\zeta})$. *The lower half* ($x \in [-5, 5]$, $y \in [-3, 0]$) *is the physical channel with* $y = \tilde{\zeta} = 0$ *indicating the undisturbed free surface. Superimposed in this complex z-plane domain are the (curvilinear) coordinate level curves from the w-plane system* $\xi\tilde{\zeta}$. *The polygonal line at the bottom of the figure is a schematic representation of the topography (where* $\tilde{\zeta} = \pm\sqrt{\beta}$*). This figure was generated using SC-Toolbox [21].*

1.1) we use curvilinear coordinates defined through the conformal mapping of this region. This strategy was already employed in [36] and [57]. For completeness we summarize the main ingredients of the asymptotic analysis in curvilinear coordinates. The symmetric domain is denoted by $\Omega_z$ where $z = x + i\sqrt{\beta}y$ and it can be considered as the conformal image of the strip $\Omega_w$ where $w = \xi + i\tilde{\zeta}$ with $|\tilde{\zeta}| \leq \sqrt{\beta}$. Note that the topography is defined along the curve $\tilde{\zeta} \equiv -\sqrt{\beta}$. Then $z = x(\xi, \tilde{\zeta}) + i\sqrt{\beta}y(\xi, \tilde{\zeta}) = x(\xi, \tilde{\zeta}) + i\,\tilde{y}(\xi, \tilde{\zeta})$ where $x$ and $\tilde{y}$ are a pair of harmonic functions on $\Omega_w$. In figure 1.2, we present a scheme which explains the changes of variables to be introduced in the sequel.

The scaled water wave equations in the fixed orthogonal curvilinear coordinates $(\xi, \tilde{\zeta})$ are:

$$\phi_{\xi\xi} + \phi_{\tilde{\zeta}\tilde{\zeta}} = 0, \qquad -\sqrt{\beta} < \tilde{\zeta} < \alpha\sqrt{\beta}N(\xi, t), \tag{1.6}$$

with free surface conditions

$$|J|N_t + \alpha\phi_\xi N_\xi - \frac{1}{\sqrt{\beta}}\phi_{\tilde{\zeta}} = 0 \tag{1.7}$$

and

$$\phi_t + \eta + \frac{\alpha}{2|J|}\left(\phi_\xi^2 + \phi_{\tilde{\zeta}}^2\right) = 0 \tag{1.8}$$

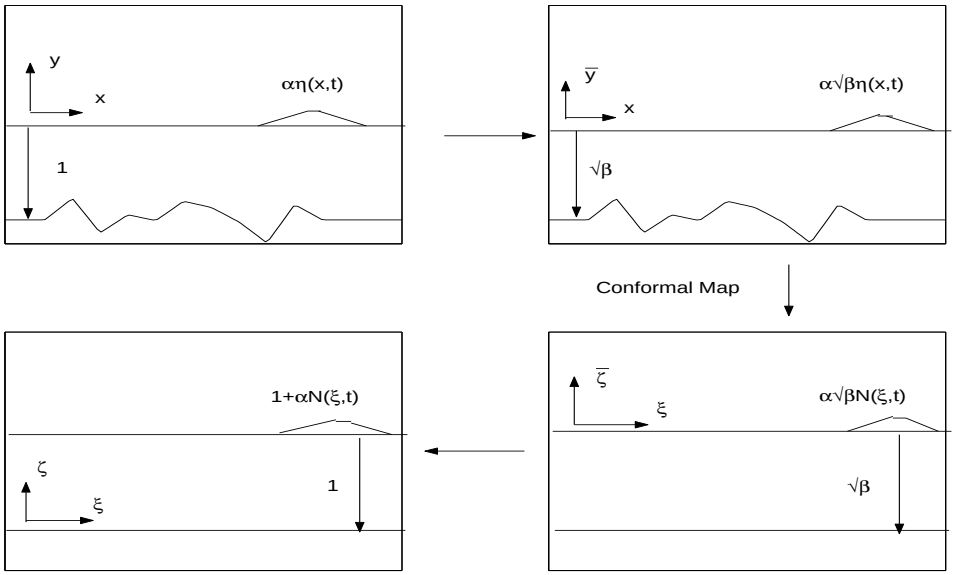


FIG. 1.2. *Schematic plot which explains the changes of variables introduced in the derivation of the extended Boussinesq equations. The conformal map transforming the rectangular coordinates* $(x, \tilde{y})$ *onto the curvilinear coordinates* $(\xi, \tilde{\zeta})$ *is indicated in this plot.*

at $\tilde{\zeta} = \alpha\sqrt{\beta}N(\xi, t)$. The bottom boundary condition (1.4) transforms into the trivial condition

$$\phi_{\tilde{\zeta}} = 0 \qquad \text{at} \quad \tilde{\zeta} = -\sqrt{\beta}. \tag{1.9}$$

The function $N(\xi, t)$ denotes the position of the free surface in the new coordinate system and $|J|$ denotes the Jacobian of the change of coordinates:

$$|J| = x_\xi \tilde{y}_{\tilde{\zeta}} - \tilde{y}_\xi x_{\tilde{\zeta}} = \tilde{y}_{\tilde{\zeta}}^2 + \tilde{y}_\xi^2.$$

At this point, it is convenient to let the origin of the curvilinear coordinate system be at the bottom and define $\tilde{\zeta} = \sqrt{\beta}(\zeta - 1)$. See the last picture in the scaling sequence given in figure 1.2. In the system of coordinates $(\xi, \zeta)$, equations (1.6)-(1.9) transform into

$$\beta\phi_{\xi\xi} \; + \; \phi_{\zeta\zeta} \; = \; 0, \qquad \text{at} \quad 0 < \zeta < 1 + \alpha N(\xi, t), \tag{1.10}$$

with free surface conditions

$$|J|N_t + \alpha\phi_\xi N_\xi - \frac{1}{\beta}\phi_\zeta = 0, \tag{1.11}$$

$$\eta + \phi_t + \frac{\alpha}{2|J|}\left(\phi_\xi^2 + \frac{1}{\beta}\phi_\zeta^2\right) = 0 \tag{1.12}$$

at $\zeta = 1 + \alpha N(\xi, t)$ and

$$\phi_\zeta = 0 \qquad \text{at} \quad \zeta = 0. \tag{1.13}$$

As in Whitham [70], consider a power series expansion near the bottom of the channel in the form

$$\phi(\xi,\zeta,t) = \sum_{n=0}^{\infty} \zeta^n \ f_n(\xi,t). \tag{1.14}$$

Asymptotic analysis will be performed at the level of the equations in terms of the small parameters $\alpha$ and $\beta$.

By substituting this expression in the scaled Laplace equation (1.10) and using the Neumann condition (1.13) at the bottom we can express the potential as a power expansion in $\beta$

$$\phi(\xi,\zeta,t) = \sum_{n=0}^{\infty} \frac{(-\beta)^n}{(2n)!}\zeta^{2n}\frac{\partial^{2n} f(\xi,t)}{\partial \xi^{2n}} \tag{1.15}$$

where, for simplicity, $f(\xi,t) = f_0(\xi,t)$.

Now using that at the smooth free surface $\tilde{\zeta}_{FS} = \alpha\sqrt{\beta}N(\xi,t)$ the Jacobian is

$$|J|(\xi,t) = \tilde{y}^2_{\xi}(\xi,\tilde{\zeta}_{FS}) + \tilde{y}^2_{\tilde{\zeta}}(\xi,\tilde{\zeta}_{FS}),$$

and the Taylor polynomial formula leads to

$$|J|(\xi,t) = \tilde{y}^2_{\tilde{\zeta}}(\xi,0) + \alpha^2 R_J(\xi,\tilde{\zeta}_M) = M(\xi)^2 + O(\alpha^2), \quad 0 < |\tilde{\zeta}_M| < |\tilde{\zeta}_{FS}|. \tag{1.16}$$

The metric term $M(\xi)$ is defined below. Thus, the Jacobian can be well approximated by an $O(1)$ time independent coefficient. The time dependent correction term is $O(\alpha^2)$ due to the fact that the curvilinear coordinate system is symmetric about $\tilde{y} = \tilde{\zeta} = 0$. There are no $O(\alpha)$ terms. For the same reason, approximating $\tilde{\zeta}(x,\tilde{y}_{FS})$ in $\tilde{y}$ leads to

$$N(\xi,t) = \frac{1}{M(\xi)}\eta(x(\xi),t) + \alpha^2\beta R_N(\xi,\tilde{y}_M), \quad 0 < |\tilde{y}_M| < |\tilde{y}_{FS}|, \tag{1.17}$$

and we establish a relation between the free surface representation in curvilinear coordinates ($N(\xi,t)$) and in cartesian coordinates ($\eta(x,t)$).

At the undisturbed level we define the **variable free surface coefficient** [57]

$$M(\xi) \equiv \tilde{y}_{\tilde{\zeta}}(\xi,0) = 1 + m(\xi)$$

where

$$m(\xi;\sqrt{\beta},\gamma) \equiv \frac{\pi}{4\sqrt{\beta}} \int_{-\infty}^{\infty} \frac{n(x(\xi_0,-\sqrt{\beta})/\gamma)}{cosh^2\frac{\pi}{2\sqrt{\beta}}(\xi_0-\xi)} d\xi_0 \ = \ (K * (n \circ x))(\xi). \tag{1.18}$$

Recall that the square of the metric term $M(\xi)$ is the leading order term of the Jacobian. Note also that the coefficient $M(\xi)$ is smooth even when the function describing the bottom is discontinuous or non differentiable. Moreover the metric coefficient is time independent and becomes identically one in the case of a constant depth. These features are important when implementing a numerical solver for the Boussinesq formulation.

Introducing the approximations (1.16), (1.17) in the equations (1.10)-(1.13), it gives

$$\beta\phi_{\xi\xi} \ + \ \phi_{\zeta\zeta} \ = \ 0, \qquad \text{at} \ \ 0 < \zeta < 1 + \alpha\frac{\eta(\xi,t)}{M}, \tag{1.19}$$

with free surface conditions

$$M\eta_t + \alpha\phi_\xi \left(\frac{\eta}{M}\right)_\xi - \frac{1}{\beta}\phi_\zeta = 0, \tag{1.20}$$

$$\eta + \phi_t + \frac{\alpha}{2M^2}\left(\phi_\xi^2 + \frac{1}{\beta}\phi_\zeta^2\right) = 0 \tag{1.21}$$

at $\zeta = 1 + \alpha(\eta(\xi,t)/M(\xi)$ and

$$\phi_\zeta = 0 \qquad \text{at} \;\; \zeta = 0. \tag{1.22}$$

Using the power series expansion for the potential the free surface conditions (1.20)-(1.21) can be further approximated as

$$\eta + f_t - \frac{\beta}{2} f_{\xi\xi t} + \frac{\alpha}{2M^2(\xi)} f_\xi^2 = O(\alpha\beta, \beta^2), \tag{1.23}$$

$$M(\xi)\ \eta_t + \left[\left(1 + \frac{\alpha}{M(\xi)}\eta\right) f_\xi\right]_\xi - \frac{\beta}{6} f_{\xi\xi\xi\xi} = O(\alpha^2, \alpha\beta, \beta^2). \tag{1.24}$$

Remark that the variable coefficients in the system above are time independent and depend only on $\tilde{y}_{\tilde{\zeta}}(\xi, 0)$. This is a consequence of equations 1.16-1.17. Moreover, the transversal curvilinear coordinate $\zeta$ does not appear in the equations above.

In [57] it is shown that equations (1.23)-(1.24) lead to the **terrain-following system**

$$M(\xi)\eta_t + \left[\left(1 + \frac{\alpha\ \eta}{M(\xi)}\right) U_o\right]_\xi = 0, \tag{1.25}$$

$$U_{o,t} + \eta_\xi + \alpha\left(\frac{U_o^2}{2M^2(\xi)}\right)_\xi - \frac{\beta}{3} U_{o,\xi\xi t} = 0, \tag{1.26}$$

where $U_o$ is the depth averaged velocity

$$U_o(\xi, t) = \frac{1}{\zeta_{FS}} \int_0^{\zeta_{FS}} \phi_\xi(\xi, \zeta, t) d\zeta. \tag{1.27}$$

As pointed out in Nachbin [57] these are weighted averages along ($\xi \equiv$constant)-curves connecting the undisturbed free surface to the topography (c.f. figure 1.3). It turns out that the conformal mapping gives more weight near the free surface, than to the regions in the deep valleys, where the topography is rapidly varying. The fact that the ($\zeta = constant$) level curves accumulate more near the free surface has a very positive impact. As mentioned above, physically this means that more emphasis is given to the flow field near the free surface, exactly where the physical model is more accurate. Recall that we are discarding viscous effects, and for example, vorticity generated at the bottom. Also, as will be shown in the numerical modeling section, the curvilinear coordinates precondition the system of PDEs leading to an underlying eigenvalue representation more amenable for computer simulations.

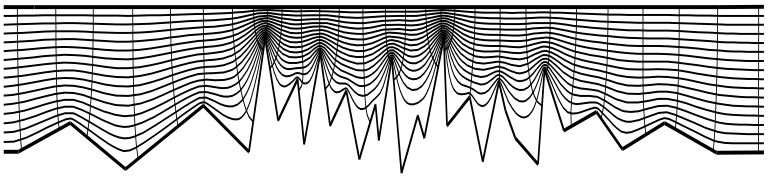

FIG. 1.3. *Multiscale topography with the $\xi - \zeta$ curvilinear coordinate system.*

**1.3. Improved Boussinesq systems.** Now instead of using the depth averaged velocity, we will express the evolution equations in terms of the fluid velocity measured at **an intermediate depth**, say at $\zeta = Z_0(\xi)$, with $u(\xi,t) = \phi_\xi(\xi, Z_0(\xi), t)$, where $0 < Z_0(\xi) < 1$. This idea was already applied by Nwogu [60] to obtain a formally equivalent Boussinesq approximation, in the case where the depth is slow-varying. The purpose was to improve the dispersive characteristics of the resulting reduced model. Recall that we are interested in the case where the topography dependent coefficient $M(\xi)$ is allowed to (also) vary on a fast scale denoted by $\ell$ [30, 28, 29, 34, 51, 52, 57]. In the sequel we will show how, by using curvilinear coordinates, we are able to extend Nwogu's strategy to more general topography profiles.

Differentiating equation (1.15) with respect to $\xi$ and evaluating at $\zeta = Z_0(\xi)$, we find that to leading order

$$u(\xi,t) = \phi_\xi(\xi, Z_0, t) = f_\xi - \frac{\beta}{2} Z_0^2 f_{\xi\xi\xi} + O(\beta^2) = \tilde{u} - \frac{\beta}{2} Z_0^2 \tilde{u}_{\xi\xi} + O(\beta^2), \tag{1.28}$$

where for simplicity, we let $\tilde{u} = \tilde{u}(\xi,t) = f_\xi(\xi,t)$ be the "slip velocity" along the bottom of the channel. As a consequence,

$$\tilde{u} = u(\xi,t) + \frac{\beta}{2} Z_0^2 \tilde{u}_{\xi\xi} + O(\beta^2). \tag{1.29}$$

Substituting the expression for $\tilde{u}$ (given by the equation above) into equations (1.23)-(1.24) and retaining only terms up to $O(\alpha)$, $O(\beta)$, we arrive at the system

$$M(\xi)\eta_t + \left[\left(1 + \frac{\alpha\,\eta}{M(\xi)}\right) u\right]_\xi + \frac{\beta}{2}\left[\left(Z_0^2 - \frac{1}{3}\right) u_{\xi\xi}\right]_\xi = 0, \tag{1.30}$$

$$u_t + \eta_\xi + \alpha\left(\frac{u^2}{2M^2(\xi)}\right)_\xi + \frac{\beta}{2}(Z_0^2 - 1) u_{\xi\xi t} = 0. \tag{1.31}$$

An interesting observation is that the system above reduces to the terrain-following system (1.25)-(1.26) when we set $Z_0 = \sqrt{1/3}$. Namely by monitoring the velocity at this intermediate depth the system is exactly the same as using the ($\zeta$) depth-averaged velocity.

Several Boussinesq formulations can be derived from equations (1.30)-(1.31) depending on where the terrain-following velocity ($\phi_\xi$) is monitored. In particular, by letting $Z_0 = \sqrt{2/3}$, system (1.30)-(1.31) reads

$$M(\xi)\eta_t + \left[\left(1 + \frac{\alpha\,\eta}{M(\xi)}\right) u\right]_\xi + \frac{\beta}{6} u_{\xi\xi\xi} = 0, \tag{1.32}$$

$$u_t + \eta_\xi + \alpha \left( \frac{u^2}{2M^2(\xi)} \right)_\xi - \frac{\beta}{6} u_{\xi\xi t} = 0. \tag{1.33}$$

Equation (1.32) implies in

$$u_\xi(\xi, t) = -M(\xi)\eta_t + O(\alpha, \beta). \tag{1.34}$$

By putting this relationship into system (1.32)-(1.33), and retaining only terms of order $O(\alpha, \beta)$, we obtain the model

$$(M(\xi)\eta)_t + \left[ \left( 1 + \frac{\alpha\ \eta}{M(\xi)} \right) u \right]_\xi - \frac{\beta}{6} (M(\xi)\eta)_{t\xi\xi} = 0, \tag{1.35}$$

$$u_t + \eta_\xi + \alpha \left( \frac{u^2}{2M^2(\xi)} \right)_\xi - \frac{\beta}{6} u_{\xi\xi t} = 0. \tag{1.36}$$

System (1.35)-(1.36) was presented by Quintero and Muñoz in [65]. The main property of this particular Boussinesq formulation is the existence of a conserved energy-type functional which enables the use of classical tools to demonstrate the global existence of its solutions [65]. We remark that the existence of this conserved quantity is unclear for the Boussinesq model (1.25)-(1.26). Of equal importance is the presence of symmetric dispersive terms in both equations of the system (1.35)-(1.36), expressed through the operator $\partial_t - \beta/6\partial_{\xi\xi t}$. This operator can be inverted [65] and the system cast into an integro-differential form, so that the fixed point principle can be applied in order to establish local existence of solutions.

Note that the dispersive terms of the model above are modified when we change the level at which the fluid velocity $u$ is measured, i.e. the parameter $Z_0$. We remark that this degree of freedom (to select the parameter $Z_0$) allows us to match the linear dispersion relation, corresponding to the Boussinesq approximation (1.30)-(1.31), with that of the original potential theory equation (1.19)-(1.22) up to a higher order. This will be explained in section 1.4.

Furthermore, recall that all variable coefficients in the model are smooth even when the physical topography profile is described by a discontinuous or even a multi-valued function. We point out that Nwogu [60] obtained a set of equations with dispersive terms similar to those in system (1.30)-(1.31) However, the applicability of Nwogu's formulation is restricted to slowly-varying bottom profiles, which is a common feature of other Boussinesq-type formulations, as for instance [63, 44, 45, 67, 71, 40]. The reason is that in cartesian coordinates the neglected terms of order $O(\alpha^2, \alpha\beta, \beta^2)$ in the Boussinesq model turn out to be large when the detailed features of the topography are small compared to the typical wavelength [36].

In contrast, in the present Boussinesq formulation (1.30)-(1.31), the neglected terms of order $O(\alpha^2, \alpha\beta, \beta^2)$ remain small **even when the topography is rapidly varying**. This is due to the use of terrain-following (curvilinear) coordinates [57]. Thus, we expect that the solutions of equations (1.19)-(1.22) and system (1.30)-(1.31) coincide with good accuracy even when dispersion is significant. When the bottom is described by a complicated function numerical experiments, to be presented in subsequent sections, will provide strong numerical evidence on this regard within the range $0 < \beta < 0.05$, $\alpha = 0.001$. To be specific, in a laboratory scale this regime is such that for example, if $h_o = 10m$ (characteristic depth), $a_o = 0.01m$, (characteristic wave amplitude) and the typical pulse width is $\ell_p \approx 44.7214m$. In the ocean these are *at*

*least* scaled by a factor of 100. For example a tsunami has a few meters of amplitude and several kilometers of length. It can be generated in regions one thousand meters deep.

**1.4. Linear dispersive properties.** To perform an analysis regarding the dispersive terms in equations (1.30)-(1.31) it is sufficient to consider the intermediate depth $Z_0$ to be a constant.

It is important to remark what is expected from the asymptotically simplified Boussinesq model (1.30)-(1.31). It would be desirable that its solution approximates, in some sense, the solution of the original potential theory equations (1.19)-(1.22), provided that $0 < \alpha \ll 1$, $0 < \beta \ll 1$. Within this regime the high-order terms $O(\alpha^2, \alpha\beta, \beta^2)$ are expected to be negligible with respect to the first order terms retained in the Boussinesq model (1.30)-(1.31).

The analytical, dispersion relation, consistency between the Boussinesq system (1.30)-(1.31) and the potential formulation of the Euler equations (1.19)-(1.22) is a necessary condition so that the new model is able to capture the same (long wave) physical phenomena as the original fluid equations.

To start, consider the linear dispersion relation which leads to the phase velocity

$$C^2 = \frac{\omega^2}{k^2} = \frac{1-(\beta/2)(Z_0^2-\frac{1}{3})k^2}{1-(\beta/2)(Z_0^2-1)k^2} \tag{1.37}$$

for model (1.30)-(1.31). Also we have the (full model's) phase velocity for Airy waves given by

$$\begin{aligned} C^2_{\text{Airy}} &= \frac{\omega^2}{k^2} = \frac{1}{\sqrt{\beta}k} tanh(\sqrt{\beta}k) \\ &\approx 1 - \frac{1}{3}(\sqrt{\beta}k)^2 + \frac{2}{15}(\sqrt{\beta}k)^4 - \frac{17}{315}(\sqrt{\beta}k)^6 + O((\sqrt{\beta}k)^8), \end{aligned} \tag{1.38}$$

corresponding to equations (1.19)-(1.22). The approximations above correspond to the Taylor series expansions for $\sqrt{\beta}k$ small. Observe that, according to equation (1.37), the velocity of propagation of solutions to models (1.30)-(1.31) and (1.19)-(1.22) depend on the wave number $k$, indicating their dispersive nature. Furthermore the phase speed is affected by depth $Z_0$ selected in the Boussinesq model. We remark that the dispersion relation (1.37) corresponds to a Padé approximation of the exact dispersion relation (1.38).

As mentioned above, the interesting point here is that we can use this degree of freedom (by selecting the parameter $Z_0$) in order to match the Taylor series expansion of the dispersion relation (1.38) up to terms of $O((\sqrt{\beta}k)^4)$. This will be shown below. By using a particular value of the intermediate depth variable $Z_0$ we can decrease the errors in the phase velocity introduced when the high-order terms $O(\alpha^2, \alpha\beta, \beta^2)$ are neglected in the asymptotic analysis used to derive the equations (1.30)-(1.31).

In constant depth, this fact can be established rigorously by using the Fourier transform technique [53]. We show that the difference in $L^2$–norm of the solutions of models (1.19)-(1.22) and the Boussinesq system (1.30)-(1.31) with $\alpha = 0$ (linear regime) and constant depth ($M \equiv 1$) is smallest when $Z_0 = \sqrt{1/5}$ within a time interval which tends to infinity when $\beta \to 0$. The analysis extends that presented in [9] which considered KdV-type models. For this value of the parameter $Z_0$, the dispersion relation (1.37) transforms into

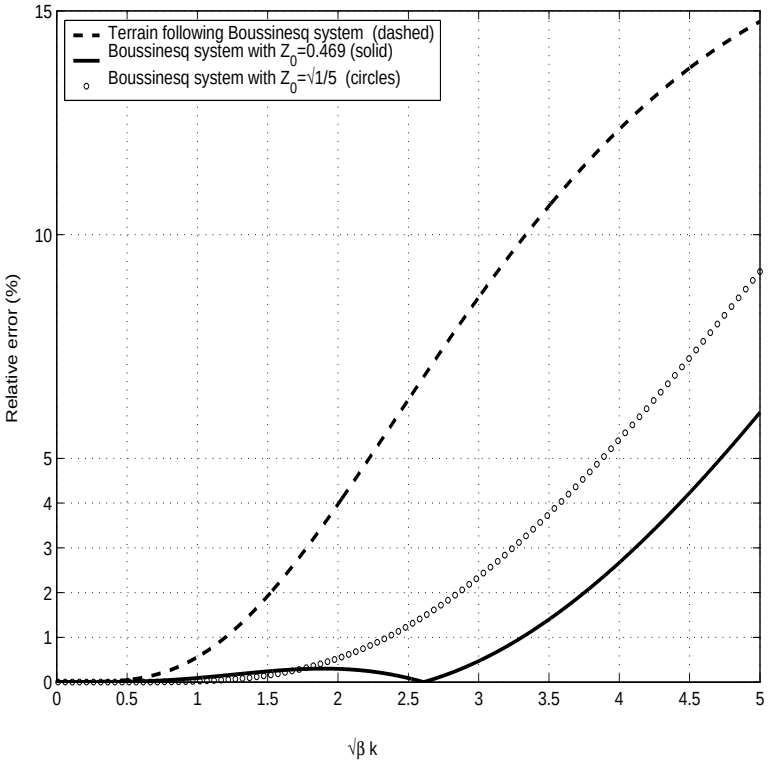


FIG. 1.4. *Relative error of the phase velocity as a function of* $\sqrt{\beta}k$ *for the Boussinesq-type system (1.30)-(1.31) with* $Z_0 = \sqrt{1/3}$ *(the terrain-following system),* $Z_0 = 0.469$ *and* $Z_0 = \sqrt{1/5}$.

$$\frac{\omega^2}{k^2} = \frac{1+(\beta/15)k^2}{1+2(\beta/5)k^2}$$
$$\approx 1 - \frac{1}{3}(\sqrt{\beta}k)^2 + \frac{2}{15}(\sqrt{\beta}k)^4 - \frac{4}{75}(\sqrt{\beta}k)^6 + O((\sqrt{\beta}k)^8). \tag{1.39}$$

This result is beyond expected since the Boussinesq model is only accurate up to order $O(\alpha, \beta)$. Thus, we get a significant improvement in accuracy of the dispersion relation of the Boussinesq approximation (1.30)-(1.31), in contrast to system (1.25)-(1.26) which is based on the depth averaged velocity. We remark that the linear dispersion corresponding to the terrain-following system (1.25)-(1.26) is only accurate up to order $O(\beta)$.

However, we can obtain an optimal value of the depth parameter $Z_0$, by minimizing the relative error of the phase velocity for instance, over the waveband interval $0 < \sqrt{\beta}k < 5$. The result of this process is the value $Z_0 = 0.469$ [60]. It gives a maximum error of 6% for the entire range. In contrast, for the terrain-following system (1.25)-(1.26), we obtain a maximum relative error in the same interval of 15%. This is shown in figure 1.4 where we compare the dispersion relations for the terrain-following system (1.25)-(1.26), with the one for formulation (1.30)-(1.31) having either $Z_0 = \sqrt{1/5}$ or $Z_0 = 0.469$. The relative error is computed with respect to the linear potential equations (1.19)-(1.22).

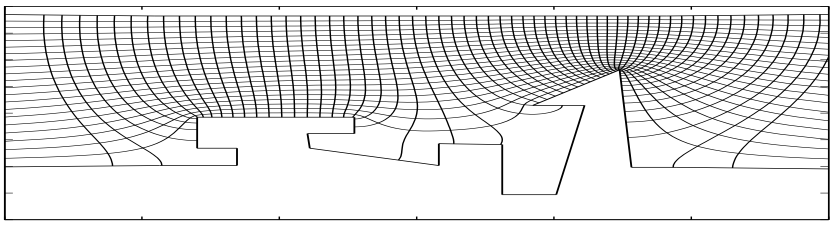

FIG. 2.1. *Topography profile together with the level curves of the $\xi\zeta$ coordinate system.*

## 2. MODELING: a FULLY DISPERSIVE MODEL.

**2.1. Introduction.** Now we will take a further step in our modeling, in such a way that we will not need to truncate the dispersion relation. In a recent paper Matsuno [46] derived a Boussinesq-type model that arises from an expansion in a steepness parameter and not in the dispersion parameter corresponding to a long wave regime as done above. Matsuno develops a method based on the theory of complex functions and a systematic perturbation theory with respect to the steepness parameter $\varepsilon \equiv a_o/\ell_p$ ($a_o$ is the amplitude scale and $\ell_p$ is a wavelength scale). We start by using dimensionless parameters such as before: let $\alpha = a_o/h_o$ be the nonlinearity parameter (with the typical, say average depth denoted by $h_o$) and $\beta = h_o^2/\ell_p^2$ be the dispersion parameter. As pointed out in [46] the formulation naturally suggests combining these parameters as $\alpha\sqrt{\beta} \equiv \varepsilon$. Hence the characteristic depth $h_o$ cancels out and the free surface perturbations are controlled through $\varepsilon$. The starting point for the asymptotic analysis are the dimensionless potential theory equations.

The novelty in the present formulation is that we can still accommodate the asymptotic modeling to consider very general topographic profiles, as for example the one presented in Fig. 2.1. As before we start from the nonlinear, dimensionless potential theory equations but follow an analytical route that is somewhat different from Matsuno's. Naturally some of the transforms used are similar, but they are "brought into the picture" by different means. In particular the Fourier analysis presented naturally suggests the use of FFT based methods to generate efficient numerical schemes.

We again use an orthogonal curvilinear coordinate system for the potential theory equations. Within this frame we are able to write a Dirichlet-to-Neumann ($DtN$) operator which automatically reduces the entire dynamics to the free surface. This formulation is possible in the presence of complex multi-valued profiles, or even rapidly varying topographies. Our transforms not only resemble, but are clearly related to, those in Matsuno [46] and in Byatt-Smith [15]. Some of the differences are that we work in Fourier space while Matsuno uses complex functions. In our formulation we work in the physical domain, through the curvilinear coordinate system and we arrive at Fourier-type transforms which are easily incorporated into a numerical method. The final result is a, variable coefficient, weakly nonlinear evolution equation of the Boussinesq-type. Our generalization of Matsuno's Boussinesq-type system has, as its (weakly dispersive) leading order approximation the terrain-following system presented in Nachbin [57]. This is a nice consistency check since here we do not use a power series expansion for the potential, but rather we do asymptotics with the Fourier operators.

Other very recent work include that of Craig and Sulem [18] which formulated an

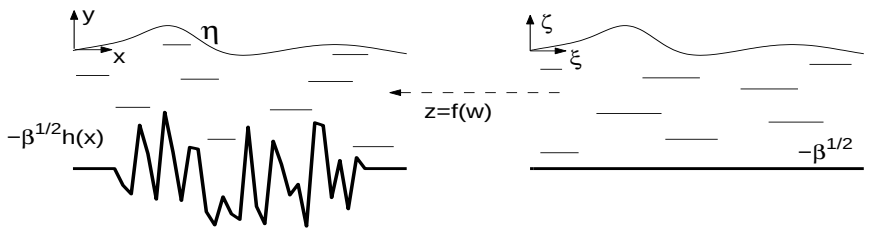


FIG. 2.2. *Setup for the Schwarz-Christoffel transformation where* $z = x + iy$ *and* $w = \xi + i\zeta$. *The mapping is defined for the undisturbed configuration (i.e. with* $\eta \equiv 0$*).*

efficient spectral method based on the $DtN$ operator. Their analysis differs from ours and Matsuno's but some resulting transforms are similar, in particular the Hilbert transform on a strip: namely equation (2.28) in the present paper, which appears as (18) in Matsuno [46] and as (27) in Craig and Sulem [18]). We recall that Matsuno's [46] as well as Craig and Sulem's analysis [18] are restricted to flat bottoms. Along these lines Zakharov *et al.* [72] using a Hamiltonian structure deduced exact (nonlinear) free surface equations in a fluid of infinite depth. The free surface is conformally mapped and Hilbert-differential equations are obtained along the free surface. The presence of Hilbert transforms has a clear connection with the three strategies mentioned above (including the present one). This is explicitly mentioned by Zakharov *et al.* [72] in a reference to the work of Craig and Sulem [18]. In the presence of highly variable topographies we point out the very recent work by Keller [39]. A shallow water (hyperbolic) model is derived from the Euler equations by using curvilinear coordinates. This curvilinear coordinate system is based on smooth topographies or a smooth curve near the topography. We recall that in the present work our curvilinear coordinate system arises from a conformal transformation and therefore is valid for polygonal bottom profiles which need not be single-valued. Moreover the resulting dispersive system can be reduced to a shallow water (hyperbolic) system by only keeping $O(\sqrt{\beta})$ terms (in the metric term $M(\xi)$ to be defined in the next subsection). This has been discussed in more detail in Nachbin [57].

This section is organized as follows. In subsection 2.2 we present a brief introduction to the free boundary problem formulated through the nonlinear potential theory. In subsection 2.3 we recall Guidotti's (time independent) formulation of the Dirichlet-to-Neumann operator on a corrugated halfplane and apply it to a corrugated strip. Its time dependent extension for nonlinear gravity waves is done in subsection 2.4 where a new (variable coefficient) Boussinesq-type system is derived. In the numerical section we will briefly outline a numerical application of the $DtN$ operator. Namely we present a very efficient spectral method for the linear potential theory problem.

**2.2. The inviscid and incompressible free boundary problem.** As before, using the Schwarz-Christoffel transformation [21, 22] we define a mapping from a uniform strip in the $\xi\zeta$-plane onto the undisturbed ($\eta \equiv 0$) corrugated strip in the physical $xy$-plane (c.f. Fig. 2.2). In the mapped domain we have $\zeta \equiv S(\xi, t) = \varepsilon N(\xi, t)$, while in the physical domain it is defined by $y(\xi, S(\xi, t)) = \alpha\eta(x(\xi, S(\xi, t)), t)$, with $\eta$ denoting the surface gravity wave. When the free surface (FS) has a small steepness (as indicated by $\varepsilon N$ above) the Jacobian can be approximated as $|J| \approx y_\zeta^2(\xi, 0) + O(\varepsilon^2)$ [57].

As presented earlier the nonlinear potential theory equations in curvilinear $\xi\zeta$

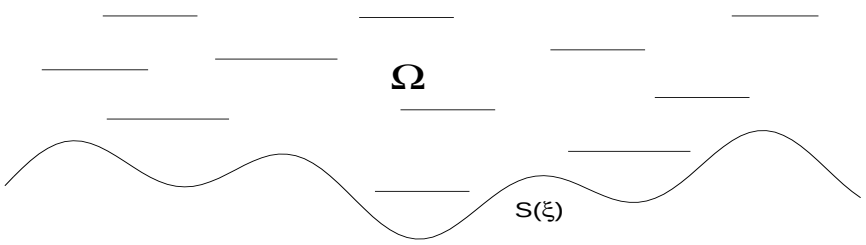


FIG. 2.3. *Upper halfplane bounded by a corrugated curve* $S(\xi)$.

coordinates, as presented in Nachbin [57] are

$$\phi_{\xi\xi} + \phi_{\zeta\zeta} = 0, -\sqrt{\beta} < \zeta < S(\xi, t). \tag{2.1}$$

where at the FS the free boundary conditions are

$$N_t + \frac{\alpha}{|J|}\phi_\xi N_\xi - \frac{1}{|J|\sqrt{\beta}}\phi_\zeta = 0 \tag{2.2}$$

$$\phi_t + \frac{\alpha}{2|J|}(\phi_\xi^2 + \phi_\zeta^2) + \eta = 0. \tag{2.3}$$

We have a trivial Neumann condition along the impermeable topography $\zeta \equiv -\sqrt{\beta}$: $\phi_\zeta = 0$. The scaling here corresponds to the third stage in the scaling sequence presented in figure 1.2. No approximation has been made up to this point.

**2.3. The Dirichlet-to-Neumann ($DtN$) operator.** In this subsection we start with a brief review on Guidotti's time independent strategy [35] to formulate a $DtN$ operator for a halfplane configuration as in Fig. 2.3. Then we will adapt this strategy to a time independent problem for a corrugated strip. Once this has been achieved we will, in a following subsection, migrate this formulism to the nonlinear wave evolution problem and reduce the entire dynamics to the free surface.

**2.3.1. The Dirichlet problem on a halfplane.** In this subsubsection, following [35], attention is given to periodic problems (say of period one) such that

$$\varphi(\xi),\ S(\xi) \in C_{per}([0,1]).$$

The notation is such that Guidotti considers Laplace's equation in the domain $\Omega$, above the curve $\Gamma \equiv (\xi, S(\xi))$, with Dirichlet data $\varphi(\xi)$ imposed along $\Gamma$. By using periodicity we are preparing our asymptotic models for FFT based numerical schemes. Obviously there is no loss of generality when we normalize the period. Let $(\xi, S(\xi))$ be a parametrization of the halfplane's (lower) boundary curve $\Gamma$. We adopt the following notation along the boundary: the mapping that takes the Dirichlet data onto its corresponding Neumann data we denote as

$$DtN[\varphi](\xi) = \partial_n \phi(\xi, S(\xi)), \tag{2.4}$$

where

$$\partial_n := \vec{n} \cdot (\partial_\xi, \partial_\zeta), \quad \vec{n} = |\Gamma_\xi|^{-1}(-S_\xi(\xi), 1) \quad \text{and} \quad |\Gamma_\xi| = \sqrt{1 + S_\xi^2(\xi)}.$$

As in classical potential theory, Guidotti suggests an integral representation for the potential, in the form

$$\phi(w) = \int_\Gamma G(w-\tilde{w})\, f(\tilde{w}) d\Gamma, \tilde{w} \in \Gamma. \tag{2.5}$$

The unknown function $f$ will be determined by the potential's Dirichlet data along $\Gamma$. The kernel is chosen so that this representation satisfies Laplace's equation and also so that FFTs are applicable. This will lead to efficient numerical schemes with exact dispersive properties for a wide class of initial data. As mentioned above, recently this has been exploited numerically by other authors [18, 72]. By $d\Gamma$ we represent an infinitesimal boundary element and by $w = (\xi, \zeta)$ an interior point of our domain $\Omega$. The 1-periodic version of the integral representation (2.5) is

$$\phi(\xi,\zeta) = \int_0^1 G(\xi-\tilde{\xi}, \zeta - S(\tilde{\xi}))\, f(\tilde{\xi}) |\Gamma_{\tilde{\xi}}| d\tilde{\xi}. \tag{2.6}$$

The periodic kernel proposed by Guidotti [35] has logarithmic singularities, in the form

$$G(\xi,\zeta) = \frac{1}{2\pi} \ln(1 + e^{-4\pi\zeta} - 2e^{-2\pi\zeta}\cos(2\pi\xi)), \tag{2.7}$$

and can also be represented by the Fourier series

$$G(\xi,\zeta) = -\sum_{\kappa\neq 0} \frac{1}{2\pi|\kappa|} e^{-2\pi|\kappa|\zeta} e^{2\pi i\kappa\xi} \qquad \text{if} \qquad \zeta \geq 0. \tag{2.8}$$

Hence the kernel is a harmonic function in the halfplane $\xi,\ \zeta > 0$, and 1-periodic in its first variable with the property that [35]

$$\lim_{\zeta\to 0^+} \partial_\zeta G(\xi,\zeta) = \lim_{\zeta\to 0^+} \frac{-2e^{-4\pi\zeta} + 2e^{-2\pi\zeta}\cos(2\pi\xi)}{1 + e^{-4\pi\zeta} - 2e^{-2\pi\zeta}\cos(2\pi\xi)} = \delta(\xi) - 1.$$

The Dirac delta is denoted by $\delta(\xi)$. Therefore one needs to be careful when deducing the $DtN$ operator since an interior point will approach a boundary curve. This result is summarized in the following lemma proved in [35]:

*Lemma*: Let $G$ be the Green's functions given above. Suppose that $S(\xi) \in C^1_{per}([0,1])$ represents a corrugated curve along the boundary of $\Omega$. Then the following limit holds as an interior point approaches this boundary:

$$\lim_{w\to w_o} \int_\Gamma \partial_{n(w)} G(w-\tilde{w}) f(\tilde{w})\, d\Gamma_{\tilde{w}} = -f(w_o) + \fint_\Gamma \partial_{n(w_o)} G(w_o - \tilde{w}) f(\tilde{w})\, d\Gamma_{\tilde{w}}$$

$$\text{when} \qquad w \to w_o = (\xi_o, S(\xi_o)) \in \Gamma.$$

The limiting integral is given as a Cauchy Principal Value (indicated by a dash). The interior point can not approach the boundary curve in the tangential direction. The dummy variable of integration is indicated in the element $d\Gamma_{\tilde{w}}$.

Clearly from the potential's integral representation (2.5) along the boundary we obtain

$$\varphi(w_o) = \int_\Gamma G(w_o - \tilde{w})\, f(\tilde{w}) d\Gamma_{\tilde{w}}, \tag{2.9}$$

where $w_o$ is also along the boundary. Its periodic counterpart leads to the following Fredholm equation of the first kind in the source density $f$:

$$\varphi(\xi) = \int_0^1 G(\xi - \tilde{\xi}, \zeta - S(\tilde{\xi}))\, f(\tilde{\xi}) |\Gamma_{\tilde{\xi}}| d\tilde{\xi}. \tag{2.10}$$

Technical details on integral equations can be found in Taylor [68].

Once we find the singularity density $f(\xi)$ we use (2.5) (or its periodic counterpart (2.6)) and the lemma above to deduce an integral representation for the Dirichlet-to-Neumann operator $DtN(\phi) = \partial_n \phi$:

$$DtN(\varphi)(w_o) = \lim_{w \to w_o} \int_\Gamma \partial_{n(w)} G(w - \tilde{w}) f(\tilde{w})\, d\Gamma_{\tilde{w}},$$

where $w_o \in \Gamma$. In the periodic regime we have

$$DtN(\varphi)(\xi_o) = -f(\xi_o) + \int_0^1 \partial_{n(\xi_o)} G(\xi_o - \tilde{\xi}, S(\xi_o) - S(\tilde{\xi})) f(\tilde{\xi}) |\Gamma_{\tilde{\xi}}|\, d\tilde{\xi}. \tag{2.11}$$

Formally this completes the calculation of the $DtN$ operator, assuming that at this stage the density $f$ is known.

Summarizing what we have presented up to this point: in order to find the (consistent) Neumann condition for the periodic Dirichlet problem we use the integral representation (2.6) for the potential. Then

1. we find $f(\xi)$, the logarithmic singularity's density distribution, by inverting the integral equation (2.10), with the kernel (2.7) and
2. we evaluate equation (2.11) using the corresponding expression for $f(\xi)$.

Recall that the Dirichlet data was denoted as $\phi(\xi, S(\xi)) = \varphi(\xi) \equiv \varphi(w)$ according to (2.9). In the next subsection we will see how to invert expression (2.10) for $f(\xi)$ in an exact fashion for the linear problem, and approximately in the weakly nonlinear regime.

**2.3.2. The Dirichlet problem on a corrugated strip.** We now prepare the formulation of the $DtN$ operator for the finite depth wave problem based on Guidotti's [35] work (for a time independent harmonic function on a corrugated half-plane) as was presented above. To simplify the presentation we first analyze the harmonic problem at a frozen instant of time:

$$\phi_{\xi\xi} + \phi_{\zeta\zeta} = 0 \quad \text{in} \quad -\sqrt{\beta} < \zeta < S(\xi) \tag{2.12}$$

$$\phi(\xi, S(\xi)) = \varphi(\xi) \quad \text{at the FS} \quad \zeta = S(\xi) \tag{2.13}$$

$$\phi_\zeta(\xi, -\sqrt{\beta}) = 0 \quad \text{at the topography} \quad \zeta = -\sqrt{\beta}. \tag{2.14}$$

Our goal is to express the Neumann data directly from its corresponding Dirichlet data $\varphi(\xi)$. By reflecting our domain about the topographic level curve $\zeta \equiv -\sqrt{\beta}$ (as in Fig. 2.4) we convert the mixed Dirichlet-Neumann problem above into a (pure) Dirichlet problem in the form

$$\phi_{\xi\xi} + \phi_{\zeta\zeta} = 0 \quad \text{in} \quad -2\sqrt{\beta} - S(\xi) < \zeta < S(\xi) \tag{2.15}$$

$$\phi = \varphi(\xi) \quad \text{at} \quad \zeta = S(\xi) \tag{2.16}$$

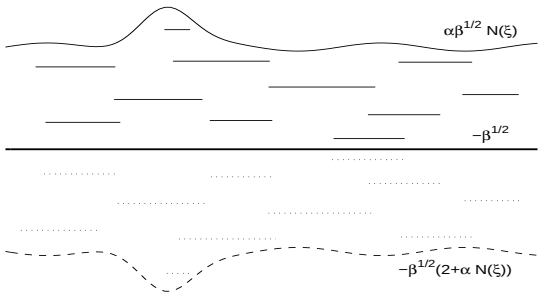


FIG. 2.4. *Reflected $\xi\zeta$-domain in order to give rise to a Dirichlet problem. The FS, in the water wave problem, is described by $S(\xi) = \varepsilon N(\xi)$; $\varepsilon \equiv \alpha\sqrt{\beta}$. The dashed curve is the FS's reflected image.*

$$\phi = \varphi(\xi) \quad \text{at} \quad \zeta = -S(\xi) - 2\sqrt{\beta}. \tag{2.17}$$

Therefore, due to the symmetry about $\zeta \equiv -\sqrt{\beta}$ we will see that the Neumann condition $\phi_\zeta(\xi, -\sqrt{\beta}) = 0$ is automatically satisfied. We proceed in obtaining an integral representation for the solution of problem (2.15)-(2.17). We again extend our domain periodically and normalize it to having period one. The time independent potential is cast into the integral representation

$$\phi(\xi,\zeta) = \int_0^1 K(\xi,\tilde{\xi},\zeta,S(\tilde{\xi}))\; f(\tilde{\xi})|\Gamma_{\tilde{\xi}}|\, d\tilde{\xi}, \tag{2.18}$$

where now the kernel has the form $K(\xi,\tilde{\xi},\zeta,S(\tilde{\xi})) = G(s,-\zeta+\tilde{S})+G(s,\zeta+\tilde{S}+2\sqrt{\beta})$. We are basically using the Method of Images for the Green's function's logarithmic singularity. In the curvilinear coordinate system this image reflection, about the highly corrugated topography, can be easily written. Our notation is such that $f(\tilde{\xi})$ is the symmetric source distribution over the top and bottom boundary curves, $|\Gamma_\xi|^2 \equiv 1+S_\xi^2(\xi)$, $s = \xi - \tilde{\xi}$ and $\tilde{S} = S(\tilde{\xi})$. One can then verify that the integral representation satisfies $\phi_\zeta(\xi,-\sqrt{\beta}) = 0$ and $\phi(\xi,\zeta) = \phi(\xi,-\zeta-2\sqrt{\beta})$ as expected. Thus we have formally solved the potential problem (2.12)-(2.14) once we find the source distribution $f(\xi)$.

Before presenting an approximate strategy for finding the source distribution $f(\xi)$ we recall the setup for defining the $DtN$ operator. The integral representation in (2.18) can be written as

$$\begin{aligned}\phi(\xi,\zeta) = &\int_0^1 K(\xi,\tilde{\xi},0,0)\; f(\tilde{\xi})|\Gamma_{\tilde{\xi}}|\, d\tilde{\xi} + \\ &+ \int_0^1 \{K(\xi,\tilde{\xi},\zeta,S(\tilde{\xi})) - K(\xi,\tilde{\xi},0,0)\}\; f(\tilde{\xi})|\Gamma_{\tilde{\xi}}|\, d\tilde{\xi}.\end{aligned} \tag{2.19}$$

The first term, containing $K(\xi,\tilde{\xi},0,0)$, is the linear (singular) term corresponding to infinitesimal perturbations about the undisturbed water surface. In this way the nonlinear term arises as a *desingularized correction term*. Taking the normal derivative of the potential in (2.19) and letting the interior point approach the top boundary we obtain, in the limit, the Dirichlet-to-Neumann operator $DtN(\varphi)(\xi) \equiv \partial\phi/\partial n(\xi, S(\xi))$, which gives the Neumann data along the FS.

Now we go back to calculating the source distribution $f(\xi)$ along the FS. Motivated by (2.19) we decompose the Dirichlet data into its linear and nonlinear parts: $\varphi(\xi) \equiv \varphi_L(\xi) + \varphi_{NL}(\xi)$.

**The linear contribution.** Using the Fourier representation of the Green's function $G$ in the linear term of (2.19), and carefully computing the limit as we approach the top boundary, we have that $\varphi_L(\xi) = \mathbf{P}[f|\Gamma_\xi|\,]$ where

$$\mathbf{P}[f|\Gamma_\xi|\,] \equiv -\sum_{\kappa\neq 0} \frac{1+e^{-2\pi|\kappa|2\sqrt{\beta}}}{2\pi|\kappa|}\,\mathbf{F}_\kappa[f|\Gamma_\xi|\,]e^{2\pi i\kappa\xi}. \tag{2.20}$$

By $\mathbf{F}_\kappa[g]$ we denote the k-th Fourier coefficient of the one-periodic function $g(\xi)$. The contribution from the linear part is easily computed through $f|\Gamma_\xi| = \mathbf{P}^{-1}[\varphi_L]$. This is equivalent to the (linear) flat FS case, but recall that for weakly nonlinear waves $S(\xi) = O(\varepsilon)$. Hence we will seek an $O(\varepsilon)$ approximation of $f(\xi)$ from the full representation (2.19).

**The nonlinear contribution.** The integral equation (2.19), evaluated along the boundary curve $\zeta = S(\xi)$, can be written in a more compact (operator) notation

$$\varphi(\xi) = \mathbf{P}[f|\Gamma_\xi|\,] + \mathbf{Q}_S[f|\Gamma_\xi|\,]. \tag{2.21}$$

The nonlinear ($S$-dependent) contribution is identified by the operator $\mathbf{Q}_S[\cdot]$. Applying $\mathbf{P}^{-1}$ at both sides and assuming that $(\mathbf{I}+\mathbf{P}^{-1}\mathbf{Q}_S)$ has an inverse, we formally arrive at

$$f|\Gamma_\xi| = (\mathbf{I}+\mathbf{P}^{-1}\mathbf{Q}_S)^{-1}\mathbf{P}^{-1}[\varphi], \tag{2.22}$$

where $\mathbf{I}$ denotes the identity. Existence conditions for the solution of equations as (2.21) are discussed in [68]. For example let $\varphi$ be continuous with period one. We observe that along the top boundary $S(\xi)$ the second part of the kernel $K$, namely $G(\xi-\tilde{\xi},\zeta+\tilde{S}+2\sqrt{\beta})$, is continuous and therefore the lemma above applies in the exact same way as before.

The main difficulty resides on inverting (2.19) and computing the source distribution $f(\xi)$ along the nonlinear FS, in the presence of a kernel depending on $S$. This was formally indicated in (2.22) but in reality we will perform an $O(\varepsilon)$ approximation in (2.21) so that $\phi(\xi,S) = \varphi(\xi) \approx \mathbf{P}[f|\Gamma_\xi|\,] + \mathbf{R}_S[f|\Gamma_\xi|\,]$. As will be shown below, the operator $\mathbf{R}_S$, which still depends on the FS profile $S$, is an $O(\varepsilon)$ approximation to the full nonlinear operator $\mathbf{Q}_S$.

As presented in detail in [3], we can characterize the leading order approximation $\mathbf{R}_S$ to the fully nonlinear operator $\mathbf{Q}_S$. Namely we have that

$$\mathbf{R}_S[f|\Gamma_\xi|\,] = S\sum_{\kappa\neq 0}\{-1+e^{-2\pi|\kappa|2\sqrt{\beta}}\}\mathbf{F}_\kappa[f|\Gamma_\xi|\,]e^{2\pi i\kappa\xi} +$$

$$+\sum_{\kappa\neq 0}\{1+e^{-2\pi|\kappa|2\sqrt{\beta}}\}\mathbf{F}_\kappa[Sf|\Gamma_\xi|\,]e^{2\pi i\kappa\xi}.$$

By using the approximate operator $\mathbf{P^{-1}}(\mathbf{I}-\mathbf{R_S}\mathbf{P^{-1}})$, to leading order, we obtain

$$f(\xi)|\Gamma_\xi| = \mathbf{P}^{-1}[\varphi] - \mathbf{P}^{-1}\mathbf{R}_S\mathbf{P}^{-1}[\varphi] + O(\varepsilon^2). \tag{2.23}$$

Using the Fourier representation of $\mathbf{R}_S$, and the inversion formula as we did above for the linear analysis, we arrive at

$$\mathbf{R}_S\mathbf{P}^{-1}[\varphi] = S\sum_{\kappa\neq 0} 2\pi\kappa\tanh(2\pi\kappa\sqrt{\beta})\mathbf{F}_\kappa[\varphi]e^{2\pi i\kappa\xi} + \\ + \sum_{\kappa\neq 0}\{1+e^{-2\pi|\kappa|2\sqrt{\beta}}\}\mathbf{F}_\kappa[S\,\mathbf{P}^{-1}[\varphi]]e^{2\pi i\kappa\xi}.$$

Then for the approximate (weakly nonlinear) inversion procedure (2.23), we have that

$$f(\xi)|\Gamma_\xi| = \mathbf{P}^{-1}[\varphi] - \mathbf{P}^{-1}[S\,DtN_0[\varphi]\,] + \sum_{\kappa\neq 0} 2\pi|\kappa|\mathbf{F}_\kappa[S\,\mathbf{P}^{-1}[\varphi]\,]e^{2\pi i\kappa\xi} + O(\varepsilon^2). \tag{2.24}$$

This approximation for the weakly nonlinear source distribution $f(\xi)$ is expressed by a linear contribution (inverting (2.20)) composed with ($S(\xi)$-dependent) iterates of linear objects: namely the linear ($S\equiv 0$) Dirichlet-to-Neumann operator $DtN_0$ and again $\mathbf{P}^{-1}[\varphi]$. In the sequel we will confirm this interpretation for the $DtN_0$ operator, which is defined by the first sum in the expression for $\mathbf{R}_S\mathbf{P}^{-1}$. Thus we have approximated the calculation of the source distribution by straightforward Fourier transforms (namely FFTs) of smooth functions. We will now show how the nonlinear $DtN$ operator can be approximated by straightforward compositions of the linear $DtN_0$ operator. This is achieved by using the approximation given in (2.24).

**2.4. Evolution equations for weakly nonlinear surface gravity waves.** In the context of nonlinear surface gravity waves, the Neumann data is needed at the second FS condition. Writing the norm (squared) of the velocity in terms of its tangential and normal components, implies that we need to find the $\xi$ and $\zeta$ derivatives as in

$$DtN[\varphi](\xi) \equiv \partial_n\phi(\xi,S) = \left[-\frac{S_\xi}{|\Gamma_\xi|}\phi_\xi + \frac{1}{|\Gamma_\xi|}\phi_\zeta\right]_{(\xi,S)}. \tag{2.25}$$

First we differentiate (2.19) with respect to $\zeta$ and use (2.24) having $\zeta = S$. After a lengthy calculation we obtain the compact expression

$$\phi_\zeta = DtN_0[\varphi - S\,DtN_0[\varphi]\,] - S\varphi_{\xi\xi} + O(\varepsilon^2). \tag{2.26}$$

When $S\equiv 0$, $\zeta$ is the normal direction and (2.26) is exact, confirming the interpretation given to $DtN_0$. There are other ways of representing the $DtN_0[\varphi]\equiv\mathbf{T}[\varphi_\xi]$:

$$\mathbf{T}[\varphi_\xi] = -i\sum_{\kappa\neq 0}\tanh[2\pi\kappa\sqrt{\beta}]\mathbf{F}_\kappa[\varphi_\xi]e^{2\pi i\kappa\xi}. \tag{2.27}$$

Note that the dispersion relation appears as the symbol of the linear $DtN_0$ operator. For example in Berger and Milewski [7] a Fourier-type integral transform, also having the dispersion relation as its symbol, is used in studying surface gravity wave interaction and wave-turbulence. This also appears in the work by Craig and Sulem [18]. As mentioned in the Introduction, we point out that $\mathbf{T}$ is the periodic counterpart of the (singular) integral operator used by Matsuno [46] and also referred to in Craig and Sulem [18] as the *Hilbert transform on the strip*:

$$\tilde{\mathbf{T}}[\varphi_x] = \frac{1}{2\sqrt{\beta}}\int_{-\infty}^{\infty}\frac{\varphi_x(x')}{\sinh[\frac{\pi}{2\sqrt{\beta}}(x-x')]}dx'. \tag{2.28}$$

Moreover it is important to notice that the operator acts on, slightly different, velocity components. Here we have a terrain-following ($\phi_\xi$) velocity component along the FS, which clearly is not tangent neither to the undisturbed, nor the perturbed FS. On the other hand Matsuno uses the horizontal ($\phi_x$) velocity component at the FS (see (18) in [46]).

Recalling that the surface wave profile is denoted by $S(\xi,t)\equiv\varepsilon N(\xi,t)$ we put together equations (2.25) and (2.26), and use the operator $\mathbf{T}$, to write the asymptotic expression

$$|\Gamma_\xi| DtN[\varphi](\xi) = \mathbf{T}[\varphi_\xi] - \varepsilon\{\mathbf{T}[(N\,\mathbf{T}[\varphi_\xi])_\xi] - (N\varphi_\xi)_\xi\} + O(\varepsilon^2).$$

Define $U\equiv\phi_\xi$ as the "horizontal" terrain-following velocity component. Then

$$\varphi_\xi = U + \varepsilon N_\xi \mathbf{T}[U] + O(\varepsilon^2)$$

and the *normal derivative approximation* reads as

$$|\Gamma_\xi|\partial_n\phi = \mathbf{T}[U] - \varepsilon\mathbf{T}[N\,\mathbf{T}[U]_\xi] - \varepsilon(NU)_\xi + O(\varepsilon^2). \tag{2.29}$$

The kinematic condition, in terms of the normal derivative to $\zeta{=}\varepsilon N$, is written as

$$N_t - |\Gamma_\xi|\partial_n\phi/(M(\xi)^2\sqrt{\beta}) = 0.$$

Substituting (2.29) and using the fact that $\eta(x,t) = M(\xi)N(\xi,t) + O(\varepsilon^2)$ [57], we obtain a fully dispersive evolution equation for the wave elevation:

$$\eta_t - \frac{1}{M\sqrt{\beta}}\big\{\mathbf{T}[U] + \varepsilon\big((\frac{\eta U}{M})_\xi + \mathbf{T}[\frac{\eta}{M}\,\mathbf{T}[U]_\xi]\big)\big\} = O(\varepsilon^2). \tag{2.30}$$

For the dynamic FS condition we start by taking its $\xi$-derivative. We should keep in mind that $\phi(\xi, S(\xi,t),t) = \varphi(\xi,t)$ is such that $d\phi/dt = \varphi_t = \phi_t + \phi_\zeta S_t$ and $\phi_t = \varphi_t - \phi_\zeta S_t$. Moreover $d(\phi_t)/d\xi = \varphi_{t\xi} - \phi_{\zeta\xi}S_t - \phi_\zeta S_{t\xi}$. Using approximations given above, together with (2.26), we have

$$\begin{aligned}\frac{d}{d\xi}\phi_t =& U_t + \varepsilon N_{\xi t}\mathbf{T}[U] + \varepsilon N_\xi \mathbf{T}[U]_t - \phi_{\zeta\xi}S_t - \phi_\zeta S_{t\xi} + \\ +O(\varepsilon^2) =& \quad U_t + \varepsilon N_\xi \mathbf{T}[U]_t - \varepsilon\mathbf{T}[U]_\xi N_t + O(\varepsilon^2).\end{aligned}$$

Going back to the dynamic condition and using the fact that we are working with the velocity components $\phi_\xi \equiv U$ and $\phi_\zeta = \mathbf{T}[U] + O(\varepsilon)$, after some computation, we arrive at

$$U_t + \eta_\xi + \varepsilon\left(\frac{1}{2\sqrt{\beta}}\Big((\frac{U^2}{M^2})_\xi + (\frac{1}{2M^2})_\xi\mathbf{T}[U]^2\Big) - (\frac{\eta}{M})_\xi\mathbf{T}[\eta_\xi]\right) = O(\varepsilon^2). \tag{2.31}$$

Dropping the $O(\varepsilon^2)$ terms in equations (2.30) and (2.31) we get a *fully dispersive terrain-following Boussinesq system*. For a flat bottom (i.e. $M(\xi)\equiv 1$) this system reduces to system (19)-(20) in Matsuno [46]. Also by expanding in $\beta$, for the weakly dispersive regime, we can recover the terrain-following Boussinesq system as in [57], when using the vertically averaged terrain-following velocity component (equation (5.12) in [57]). Moreover for $\beta > 0.25$ it is known [19], from the linear potential theory, that the surface wave does not feel the bottom anymore. Therefore beyond a

certain value of $\beta$ there is no point in generalizing Matsuno's formulation. We should also point out that linearizing system (2.30) and (2.31) (by setting $\varepsilon = 0$) we have that

$$\eta_t - \frac{1}{M\sqrt{\beta}}\big\{\mathbf{T}[U] = 0,$$

$$U_t + \eta_\xi = 0.$$

Eliminating $\eta$ from this system and performing a Fourier transform of the resulting second order equation (in the flat bottom case; $M \equiv 1$) clearly leads to the full dispersion relation. Hence we say that system (2.30)-(2.31) is fully dispersive.

Following Matsuno [46] system (2.30)-(2.31) can be transformed into a, variable coefficient, second order Boussinesq equation:

$$\sqrt{\beta}M\eta_{tt} + \mathbf{T}[\eta_\xi] + \varepsilon\left\{-\frac{1}{2}\big(\frac{(\eta^2)_\xi}{M}\big)_\xi + \sqrt{\beta}\big(\frac{\eta_t}{M}\mathbf{T}^{-1}[M\eta_t]\big)_\xi +\right.$$

$$\left. +\frac{\sqrt{\beta}}{2}\mathbf{T}\Big[\eta_t^2 + \mathbf{T}^{-1}[M\eta_t]^2\frac{1}{M^2}\Big]_\xi - \mathbf{T}\big[\frac{\eta}{M}\,\mathbf{T}[\eta_\xi]\big]_\xi\right\} = 0.$$

We point out that derivatives of the metric term $M(\xi)$ produce $O(\beta^{-1/2})$ terms [57, 52]. For the flat bottom case ($M \equiv 1$), using the identity $\mathbf{T}[\mathbf{T}^{-1}[f]^2] = \mathbf{T}[f^2] + 2\mathbf{T}[f]f$ given in [46], this equation reduces to Matsuno's main result (namely equation (22); c.f. definition of $\delta$ and $\kappa$ in [46] page 609). In the presence of the metric term the simplification of the equation, through the above identity, does not apply.

## 3. SOLUTION ASYMPTOTICS: DETERMINISTIC APPROACH.

**3.1. Introduction.** Our focus now changes from the PDEs and concentrates on the solutions. Namely we consider the regime of large propagation distances for pulse shaped waves and the corresponding effect of small-scale orographic features, which we call the *microstructure*. Mathematically we want to study (asymptotically) the effective properties of solutions to PDEs having highly oscillatory (disordered) coefficients. For example the PDEs' coefficients may vary on the microscale, the initial data is set on a (intermediate) mesoscale and the (entire) space/time solution domain is the macroscale. A mathematical theory is described and its robustness validated numerically. As surface gravity waves propagate from deep to shallow waters, they are transformed due to shoaling, refraction, diffraction and reflection. In order to concentrate on the main scattering mechanism connected with the pulse shaping phenomenon to be described, we consider the normal incidence of surface pulse shaped waves. These waves propagate over topographies containing a smooth slowly varying profile together with disordered small-scale features. As pointed out, our goal is to capture the wave-microstructure interaction.

The main result is that the disordered medium fluctuations cause the propagating pulse to broaden as it travels. Due to multiple scattered energy, the pulse **appears to diffuse** about a moving center. The amount of broadening and attenuation is proportional to the traveling distance and depends on the disorder's correlation function. In the sequel we refer to the transformation of the pulse, due to the medium's microscale fluctuations as *pulse shaping*.

The theory for pulse shaping was originally derived in the context of acoustic wave propagation in the earth's crust [61]. It is known as the O'Doherty–Anstey (ODA) approximation. In the acoustic wave applications several authors have analyzed the spreading of a pulse due to the microscale variations in the medium parameters (c.f. for example the work by Clouet and Fouque [16], Papanicolaou and Sølna [62] and Lewicki *et al.* [41]). The motivation for modeling in terms of a random medium (as briefly outlined in the next section) is that a detailed description of microscale medium fluctuations are often not known. Using a stochastic model uncertainties about a specific medium are translated into uncertainties about a transmitted pulse shape in a systematic way [4].

In the interest of clarity we start with the deterministic approach and then, in the next section, indicate how the stochastic modeling follows. The work presented in these sections generalize the one-dimensional ODA theory for linear weakly dispersive water waves, when forced by a disordered orography. The analysis is performed through the terrain-following Boussinesq system [57]. This is achieved by applying the invariant imbedding method. As a result dispersion alters the medium's correlation function which controls the apparent attenuation mechanism. On the other hand, orography affects the dispersive mechanism for the Airy function-like formation. The theoretical results presented here are in very good agreement with small amplitude computer simulations. This amounts to solving the nonlinear Boussinesq system with data on a small amplitude-to-depth ratio.

**3.2. The linearized terrain-following Boussinesq model.** The goal of this section is to obtain the effective behavior along the wavefront when the long pulse shaped wave interacts with rapidly varying disordered topographic features. By disordered we mean without a specific structure, in contrast for example, with the case of a periodic medium. The term disorder also naturally suggests that a probabilistic modeling may be useful. But the first goal through the deterministic modeling is to show that this conservative system (which started with potential theory), to leading order, appears to be under the effect of diffusion.

In order to do asymptotics at the level of solutions, we will rewrite our reduced system in terms of right and left propagating modes and perform its Fourier transform. A system of ODEs will arise and its solution characterized in an approximate fashion. The approximate integral representation of the transmitted wave is given by the convolution of the initial pulse with a Gaussian (heat-like) kernel, hence characterizing the **apparent diffusion**

Recall that by asymptotically reducing the full potential equations we arrived at the weakly nonlinear, weakly dispersive terrain-following Boussinesq system, here repeated in the form

$$M(\xi)\eta_t + \left(\left(1 + \frac{\alpha\eta}{M(\xi)}\right)u\right)_\xi = 0,$$
$$u_t + \eta_\xi + \frac{\alpha}{2}\left(\frac{u^2}{M(\xi)^2}\right)_\xi - \frac{\beta}{3}u_{\xi\xi t} = 0.$$

When $\alpha = 0$ the system above reduces to

$$M(\xi)\eta_t + u_\xi = 0, \tag{3.1}$$
$$u_t + \eta_\xi - \frac{\beta}{3}u_{\xi\xi t} = 0.$$

Also recall that $\eta = \eta(\xi, t)$ is the wave elevation and $u = u(\xi, t)$ is the weigthed depth-averaged terrain-following velocity [57].

We will analyse the linear ($\alpha = 0$) Boussinesq system for a large range of dispersive effects, expressed through the parameter $\beta$. It is very important to note that for $\beta > 0.25$ we are in the *deep water* regime. The particle-orbits decay exponentially with depth as shown in Dean and Dalrymple [19] (chapter 4; on linear potential theory). Hence in this regime there is no wave-topography interaction. Thus the fact that the Boussinesq system is an $O(\beta)$ approximation to the potential theory is not much of a limitation for dispersive wave-topography interaction. Moreover for large time intervals dispersive effects will be strongly displayed in the solutions even for small values of $\beta$ (c.f. appendix A). Even though the theory we have developed is linear, in our numerical experiments we will consider nontrivial values of $\alpha$ as will be shown in the corresponding subsections.

**3.3. The linear pulse-shaping theory.** In this subsection we generalize the O'Doherty-Anstey (ODA) approximation from linear acoustic waves to the linear weakly dispersive system (3.1). The weakly dispersive Boussinesq system is forced by a rapidly varying orography expressed through the variable coefficient $M(\xi)$. We consider a technique analogous to Berlyand and Burridge's acoustic work [8], which we apply successfully to dispersive waves due to two reasons. First, system (3.1) can be written equivalently as two coupled KdV-type equations for the transmitted and reflected fields. These linearized KdV-type equations can be viewed as a dispersive perturbation to those obtained by Berlyand and Burridge. Namely a propagating pulse will slowly disperse with a given (known) rate (c.f. appendix A, equation (A.4)). Second, the pulse's effective propagation velocity is bounded and all Fourier modes have positive phase speeds bounded by 1. These two properties described allow us to apply the *invariant imbedding approach* [50], taking the propagation distance as the *imbedding parameter*. The key physical idea is that by having a finite propagation speed the wave will not reach very deep into the medium in a finite time interval. For acoustic waves the dimensionless phase speed is identical to one. For dispersive waves the phase speed is bounded by one. Hence the invariant imbedding applies. This means that we can imbed the disorded medium into a medium which is homogeneous, to the right and the left, beyond a certain interval. This allows for appropriate boundary conditions at the extremes of the interval of interest. Then this boundary value ODE problem can be transformed into an initial value problem which can be solved for the reflection kernel. This is an outline of the strategy adopted below.

In what follows solutions $u, \eta$ to (3.1) will be assumed to be smooth enough and absolutely integrable. This requirement is necessary to justify the use of the Fourier transform and the Fourier inversion formula.

We start by performing the change of variables

$$x = \int_0^\xi \frac{1}{C_o(s)} ds, \quad t' = t,$$

in system (3.1). Here $C_o(s) = \sqrt{1/M(s)}$ is the *local wave speed* and $x$ is the *travel time*. Dropping the primes system (3.1) becomes

$$\begin{aligned} & C_o^{-1/2}\ \eta_t + C_o^{1/2}\ u_x = 0, \\ & C_o^{1/2}\ u_t + C_o^{-1/2}\ \eta_x - \frac{\beta}{3C_o^{1/2}} \left( u_{xxt}\ \frac{1}{C_o} + \left( \frac{1}{C_o} \right)_x u_{xt} \right) = 0. \end{aligned} \tag{3.2}$$

We adopt the *wave mode splitting*

$$R = C_o^{1/2}u + C_o^{-1/2}\eta, \tag{3.3}$$

$$L = -C_o^{1/2}u + C_o^{-1/2}\eta. \tag{3.4}$$

Differentiating (3.3) and (3.4) with respect to $x$ and $t$, using (3.2) and the fact that $u = (R-L)/(2C_o^{1/2})$, leads to the coupled wave mode system

$$\begin{aligned} R_t + R_x &= p(x)\left(\frac{R-L}{2C_o^{1/2}}\right)_{xxt} + q(x)\left(\frac{R-L}{2C_o^{1/2}}\right)_{xt} - r(x)L, \\ L_x - L_t &= p(x)\left(\frac{R-L}{2C_o^{1/2}}\right)_{xxt} + q(x)\left(\frac{R-L}{2C_o^{1/2}}\right)_{xt} - r(x)R, \end{aligned} \tag{3.5}$$

where the variable coefficients are

$$p(x) = \frac{\beta}{3C_o^{3/2}(x)}, \quad q(x) = -\frac{\beta C_{o,x}(x)}{3C_o^{5/2}(x)}, \quad \text{and} \quad r(x) = \frac{C_{o,x}(x)}{2C_o(x)}.$$

The initial conditions for system (3.5) are

$$R(x,0) = R_o(x), \quad L(x,0) = 0.$$

Note that when the bottom is flat ($r \equiv 0$) and $\beta = 0$ (no dispersion) equations (3.5) identify $R$ with a wave propagating to the right (transmitted wave) and $L$ with a wave propagating to the left (reflected wave). For variable depths we adopt the same terminology. Moreover, this terminology is also consistent for system (3.5), in the weakly dispersive regime ($0 < \beta \ll 1$) and $r \equiv 0$, since the left propagating signal $L$ is negligible if the initial data corresponds to a rightgoing wave (see appendix A). In the next section (for the random modeling) we will show how exact right and left going modes can be generated.

Several decompositions of the Boussinesq equations into a pair of KdV equations are introduced by Mattioli in [47] and [48]. We point out that system (3.5) has some advantages with respect to those decompositions presented by Mattioli. First, unlike system (3.5), the Boussinesq equations used by Mattioli are not valid as an asymptotic approximation of the potential theory equations for arbitrary rapidly-varying or non-differentiable orographies. Second, in contrast to system (3.5), the linear dispersion relation for Mattioli's model results in unstable short waves.

In order to set our forthcoming results in a wave propagating frame let us introduce the change of variables

$$\tau = t - x, \quad x' = x,$$

where $\tau$ is the time-delay variable. Again abandoning the primes, equations (3.5) become

$$\begin{aligned} R_x &= p\left(\frac{R-L}{2C_o^{1/2}}\right)_{\tau\tau\tau} - 2p\left(\frac{R-L}{2C_o^{1/2}}\right)_{x\tau\tau} + p\left(\frac{R-L}{2C_o^{1/2}}\right)_{xx\tau} \\ &\quad -q\left(\frac{R-L}{2C_o^{1/2}}\right)_{\tau\tau} + q\left(\frac{R-L}{2C_o^{1/2}}\right)_{x\tau} - rL, \\ L_x - 2L_\tau &= p\left(\frac{R-L}{2C_o^{1/2}}\right)_{\tau\tau\tau} - 2p\left(\frac{R-L}{2C_o^{1/2}}\right)_{x\tau\tau} + p\left(\frac{R-L}{2C_o^{1/2}}\right)_{xx\tau} \\ &\quad -q\left(\frac{R-L}{2C_o^{1/2}}\right)_{\tau\tau} + q\left(\frac{R-L}{2C_o^{1/2}}\right)_{x\tau} - rR. \end{aligned} \tag{3.6}$$

One of the advantages of this form is that the left hand, first order terms, are in triangular form. This allows for making one dependent variable a passive variable namely, passively depending on the other dependent variable. Once the dominant variable has been solved for, the passive variabe is readily obtained.

Let $\widehat{f}(\omega)$ denote the Fourier Transform of $f(\tau)$ in the time-delay variable $\tau$:

$$\widehat{f}(\omega) = \int_{-\infty}^{\infty} e^{-i\omega\tau} f(\tau)\, d\tau.$$

Take the Fourier Transform in $\tau$ of equations (3.6). Manipulate the resulting system in order to obtain first order equations for the travel time-evolution of the Fourier modes. This goal is achieved by first subtracting the two equations giving

$$\widehat{R}_x - \widehat{L}_x = r\widehat{R} - 2i\omega\widehat{L} - r\widehat{L}. \tag{3.7}$$

Moreover, by differentiating this equation with respect to $x$ we find

$$\begin{aligned}\widehat{R}_{xx} - \widehat{L}_{xx} = {} & r'(x)\widehat{R} - r'(x)\widehat{L} - 2iw\widehat{R}_x + 2iwr(x)\widehat{R} \\ & +4w^2\widehat{L} - 4iwr(x)\widehat{L} + r^2(x)\widehat{R} - r^2(x)\widehat{L}.\end{aligned} \tag{3.8}$$

This expression can be used to eliminate the second order $x-$derivatives in the first Fourier transformed equation arising from (3.6). This is a crucial step in order to apply the invariant imbedding approach, which requires a first order system of ordinary differential equations (ODE). Using the fact that the time frequency range $|\omega| < C_o(x)\sqrt{3/\beta}$ (see appendix A) we solve for $\widehat{R}_x$ to obtain

$$\widehat{R}_x = \zeta(x,\omega)\widehat{L} + \gamma(x,\omega)\widehat{R}, \tag{3.9}$$

where

$$\zeta(x,\omega) = \frac{id(x)\omega^3 + e(x)\omega^2 - 2r(x)}{2(1 - d(x)\ \omega^2)}, \quad \gamma(x,\omega) = \frac{\frac{-i\beta\omega^2}{3C_o^2(x)}(\omega - 4ir(x))}{2\left(1 - \frac{\beta\omega^2}{3C_o^2(x)}\right)},$$

$$d(x) = \frac{\beta}{3C_o^2(x)} \quad \text{and} \quad e(x) = -\frac{\beta}{3C_o^3(x)}C_{o,x}(x).$$

Putting equation (3.9) into equation (3.7) and solving for $\widehat{L}_x$ results in

$$\widehat{L}_x = (2i\omega + \bar{\gamma}(x,\omega))\widehat{L} + \bar{\zeta}(x,\omega)\widehat{R}, \tag{3.10}$$

where $\bar{\zeta}(x,w)$ and $\bar{\gamma}(x,w)$ denote the complex conjugates of $\zeta(x,w)$ and $\gamma(x,w)$, respectively. As claimed above, equations (3.9) and (3.10) give the evolution in $x$ (travel time) of each Fourier mode, corresponding to the transmitted and reflected fields.

Next, suppose that we want to calculate $L(x_o,\tau) = L(x_o,\tau;T)$ for $0 \le \tau \le T$. At this step we apply the *invariant imbedding approach* [50] to system (3.9) and (3.10). To do so we imbed the relevant inhomogeneous region inside a homogeneous medium so that we can give appropriate boundary conditions at the border of the medium's slab $[x_o, x_o + X]$, say

$$\widehat{R}(x_o,\omega;T) = \widehat{h}(\omega), \tag{3.11}$$

$$\widehat{L}(x_o + X,\omega;T) = 0. \tag{3.12}$$

Boundary condition (3.12) means that no reflection is expected at the downstream travel time location $x_o+X$ when $0 < \tau = t-x_o < T$. In other words, the signal did not have enough time to arrive at this point and to produce a medium's response. This is true at least for some $X > 0$ large enough (depending on $T$) due to the pulse's finite (effective) velocity mentioned earlier. Linearity of ODE system (3.9)-(3.10) and the invariant imbedding technique [50] guarantees the existence of a function $K(x, \omega; T)$ (called the *reflection kernel*) such that

$$\widehat{L}(x, \omega; T) = \widehat{K}(x, \omega; T)\ \widehat{R}(x, \omega; T) \tag{3.13}$$

and satisfying the Ricatti-type equation

$$\widehat{K}_x = \bar{\zeta}(x, \omega) + 2i\omega\Gamma(x, \omega)\widehat{K} - \zeta(x, \omega)\widehat{K}^2, \tag{3.14}$$

with

$$\Gamma(x, \omega) = \frac{2 - d(x)\omega^2}{2(1 - d(x)\omega^2)}.$$

From equation (3.12) we obtain an appropriate initial condition for equation (3.14):

$$\widehat{K}(x_o + X, \omega; T) = 0. \tag{3.15}$$

Notice that equation (3.13) allows us to solve for the reflected signal $L(x_o, \tau; T)$ in terms of the reflection kernel $K(x_o, \tau; T)$ and the transmitted pulse $R(x_o, \tau; T)$ for $0 \le \tau \le T$. This function $K$ contains all the information about medium's reflection properties. We also remark that the boundary value problem (3.9)-(3.12) has been reduced to solving the initial value problem (3.14)-(3.15) in reversed direction from the travel time location $x_o + X$ up to the time of interest $x_o$.

In general it is not possible to solve explicitly for $\widehat{K}$ from equation (3.14) so we adopt an approximation. To this end we present the following generalization to the lemma given by Berlyand and Burridge [8].

LEMMA 3.1. *Let $y$ satisfy the Ricatti equation*

$$y'(s) = -A(s) - 2i\omega B(s)y(s) + \bar{A}(s)y^2(s), \quad 0 \le s \le s_o, \tag{3.16}$$

*subject to the initial condition $y(0) = 0$. Here $\bar{A}(s)$ denotes the complex conjugate of $A(s)$. Hence the solution can be expressed as*

$$y(s_o) = -\int_0^{s_o} e^{-2i\omega \int_{s'}^{s_o} B(\xi)d\xi} A(s')ds' + E(s_o), \tag{3.17}$$

*where the error term is*

$$E(s_o) = \int_0^{s_o} \bar{A}(s')e^{-2i\omega \int_{s'}^{s_o} B(\xi)d\xi} y^2(s')ds'.$$

*Set*

$$v(s_o) = \sup_{0\le s\le s_o} \left| \int_0^s e^{2iw \int_0^{s'} B(\xi)d\xi} A(s')ds' \right| \quad \textit{and} \quad V(s) = \int_0^s |A(s')|\, ds'.$$

*If $v(s_o)V(s) < 1$ then*

$$|E(s)| \le \frac{v^2(s_o)V(s)}{1 - v(s_o)V(s)}, \quad 0 \le s \le s_o. \tag{3.18}$$

The proof is given in [51]. We now apply these results to our Ricatti equation. For brevity the argument $T$ will be omitted in what follows. We apply the lemma above to the reflection kernel's problem (3.14)-(3.15) by letting $y(s) = \widehat{K}(x(s),\omega)$, $A(s) = \bar{\zeta}(x(s),\omega)$, $B(s) = \Gamma(x(s),\omega)$ and $s = x_o + X - x$, $s_o = X$. We deduce that

$$\widehat{K}(x,\omega) = -\int_x^{x+X} e^{2i\omega \int_{x'}^{x} \Gamma(s,\omega)\, ds} \bar{\zeta}(x',\omega) dx' + E(x,\omega), \tag{3.19}$$

with an error term given by

$$E(x,\omega) = \int_x^{x+X} e^{2i\omega \int_{x'}^{x} \Gamma(s,\omega)\, ds} \zeta(x',\omega) \widehat{K}^2(x',\omega) dx'.$$

Also

$$v(x_o,\omega) = \sup_{x_o \le x \le x_o+X} \left| \int_x^{x_o+X} e^{2i\omega \int_{x'}^{x_o+X} \Gamma(s,\omega)\, ds} \bar{\zeta}(x',\omega) dx' \right|$$

and

$$V(x_o,\omega) = \int_{x_o}^{x_o+X} |\zeta(x',\omega)|\, dx'.$$

Then in the cases where $v(x_o,\omega)V(x_o,\omega) < 1$ the error bound follows.

Now we solve for $\widehat{R}(x_o,\omega)$ at an arbitrary point $x_o$ by using equation (3.19) and (3.13) in equation (3.9). It results that

$$\widehat{R}_x(x,\omega) = \left( \zeta(x,\omega) \left( -\int_x^{x+X} e^{2i\omega \int_{x'}^{x} \Gamma(s,\omega)\, ds} \bar{\zeta}(x',\omega) dx' + E(x,\omega) \right) + \gamma \right) \widehat{R}(x,\omega).$$

Solving this initial value problem with $\widehat{R}(0,\omega) = \widehat{f}(\omega)$ then

$$\widehat{R}(x_o,\omega) = \widehat{f}(\omega)\ \exp\left[ -\int_0^{x_o} \int_x^{x+X} \zeta(x,\omega) e^{2i\omega \int_{x'}^{x} \Gamma(s,\omega)\, ds}\ \bar{\zeta}(x',\omega) dx' + \gamma(x,\omega)\ dx \right]$$

$$\cdot \exp\left[ \int_0^{x_o} \zeta(x,\omega)\ E(x,\omega)\, dx \right]. \tag{3.20}$$

For general rapidly varying orographies and $\beta \ll 1$ the error function $E(x,\omega)$ is small [51], even though the error estimate (3.18) is not useful in this case. It is sharp for instance when the function describing the medium properties (the metric coefficient $M(x)$ in system (3.1)) is taken to be piecewise constant on travel-time intervals with equal length (called a *Goupillaud medium*) [54].

Therefore, equation (3.20) leads to the *generalized O'Doherty-Anstey approximation*

$$\widehat{R}(x_o,\omega) \approx \widehat{f}(\omega) e^{-x_o(a_\beta(x_o,\omega) + b(x_o,\omega))}, \tag{3.21}$$

where

$$a_\beta(x_o,\omega) = \frac{1}{x_o} \int_0^{x_o} \int_x^{x+X} \zeta(x,\omega) e^{2i\omega \int_{x'}^{x} \Gamma(s,\omega)\, ds} \bar{\zeta}(x',\omega) dx'\, dx, \tag{3.22}$$

$$b(x_o,\omega) = -\frac{1}{x_o} \int_0^{x_o} \gamma(x,\omega)\, dx. \tag{3.23}$$

Using approximation (3.21) we can obtain an expression for $R(x_o,\tau)$ (the transmitted field in our applications) by using the Fourier inversion formula. Thus for $0 \le \tau \le T$

$$R(x_o,\tau) \approx \frac{1}{2\pi}\int_{-\infty}^{\infty} \widehat{f}(\omega) e^{-x_o(a_\beta(x_o,\omega)+b(x_o,\omega))} e^{i\omega\tau} d\omega. \tag{3.24}$$

Note that the exponential factor in equation (3.24) accounts for the wave attenuation at travel time $x_o$. It can be shown that, to leading order, this exponential term behaves like a Gaussian kernel, hence characterizing the apparent diffusion. As mentioned above not always the error estimate given above is sharp. For this reason the error term $E(x_o,\omega)$ is calculated numerically in [51]. Furthermore, for dispersion parameter $\beta$ small enough and constant depth ($r(x) \equiv 0$) we have that $a_\beta = O(\beta^2)$ and $b = O(\beta)$. Hence for variable depths, it is reasonable to approximate the medium's dispersive correlation function $a_\beta(x_o,\omega)$ by the medium's hyperbolic correlation function $a_0(x_o,\omega)$, that is,

$$a_\beta(x_o,\omega) \approx \frac{1}{x_o}\int_0^{x_o}\int_x^{x+X} r(x) e^{2i\omega(x-x')} r(x') dx'\, dx \equiv a_0(x_o,\omega). \tag{3.25}$$

This approximation, valid for small values of $\beta$, is not a limitation of the theory but enables numerical efficiency on the evaluation of the Fourier integrals. Note that this hyperbolic version is easier to compute than the dispersive formula (3.22). Note that in the latter the function $\zeta$ depends on the frequency $\omega$. Therefore the Fourier-type integral in $a_\beta$ can not be computed rapidly by using the FFT (Fast Fourier Transform). On the other hand, the integral in equation (3.25) can be easily evaluated by the FFT algorithm because in this case the coefficient $r(x)$ is frequency independent. In appendix B we detail the numerical computation of the Fourier-type integral in coefficient $a_\beta(x_o,\omega)$. The accuracy of approximation (3.25) will be verified in subsection 3.4 showing that the leading order dispersive effects are controlled by coefficient $b(x_o,\omega)$.

The numerical experiments in subsection 3.4 will show that approximation (3.24) captures very well not only the wave front but also part of the forward scattering radiation. The parameter $X$ in equation (3.22) (or (3.25)) regulates to what extent the incoherent signal is recovered.

If $\beta = 0$ then $b(x_o,\omega) \equiv 0$ and the approximation given by (3.21) reduces to

$$\widehat{R}(x_o,\omega) \approx \widehat{f}(\omega) e^{-x_o a_0(x_o,\omega)}, \tag{3.26}$$

where

$$a_0(x_o,\omega) = \frac{1}{x_o}\int_0^{x_o}\int_x^{x+X} r(x) e^{2i\omega(x-x')} r(x') dx'\, dx,$$

as in Berlyand and Burridge's work [8]. We recall that when $\beta \neq 0$ the hyperbolic medium's correlation function $a_0(x_o,\omega)$ (which controls the attenuation mechanism) is altered and an extra attenuation term $b(x_o,\omega)$ appears due to the model's dispersion.

**3.4. Numerical illustration of the generalized ODA theory.** Consider the nonlinear terrain-following Boussinesq system

$$\begin{aligned} &M(\xi)\eta_t + \left(\left(1+\frac{\alpha\eta}{M(\xi)}\right)u\right)_\xi = 0, \\ &u_t + \eta_\xi + \frac{\alpha}{2}\left(\frac{u^2}{M(\xi)^2}\right)_\xi - \frac{\beta}{3}u_{\xi\xi t} = 0. \end{aligned} \tag{3.27}$$

We recall that when $\alpha = 0$ system (3.27) reduces to (3.1). Nevertheless for our numerical validation experiments we will use the nonlinear Boussinesq system in a small $\alpha$ regime. Two types of initial data are considered. We study the propagation of Gaussian-shaped disturbances of the form

$$u(\xi, 0) = \eta(\xi, 0) = e^{-(\xi-\xi_o)^2/\epsilon},$$

where the parameter $\xi_o$ controls the pulse's initial position and $\epsilon > 0$ its effective width. Furthermore, we also consider solitary waves of the form

$$\eta(\xi, 0) = A_1 \text{ sech}^2(B(\xi - \xi_o)) + A_2 \text{ sech}^4(B(\xi - \xi_o)),$$
$$u(\xi, 0) = A \text{ sech}^2(B(\xi - \xi_o)),$$

with $A_1$, $A_2$, $A$ and $B$ constants (to be defined in experiment 2). These are approximate solutions to system (3.27) with $M \equiv 1$ (see [69]).

Except in some special cases (for instance when $M \equiv 1, \alpha = 0$ or $\beta = 0$), finding the solution of system (3.27) is a nontrivial problem. To solve system (3.27) numerically we will use a finite difference solver introduced by Wei and Kirby [69]. This scheme will be used to perform numerical experiments in order to validate the theory developed in the previous subsections. Details will be provided in the numerical modeling section.

We now describe several experiments ilustrating the dispersive pulse-shaping ODA theory.

**Experiment set 1 (Flat channel and effectively linear regime):** In these experiments the pulse is assumed to propagate over a flat bottom ($M \equiv 1$). In appendix A (c.f. equations (A.6) and (A.7)) we show that if in addition $\alpha = 0$ we can solve explicitly system (3.27) by using the Fourier transform technique. Flat channel solutions are employed to verify the numerical method's accuracy regarding dispersive and stability properties.

In figure 3.1 we see that the exact solution $\eta$ (for $\alpha = 0$, $\beta = 0.03$) and the numerical solution (for $\alpha = 0.001$, $\beta = 0.03$) are in very good agreement at $t = 40$. After 40 length-units into the flat channel the right propagating Gaussian has developed an Airy-like oscillatory tail (c.f. appendix A). The dispersive properties of the numerical scheme are very good.

For this experiment the numerical parameters are $J = 4000$ (spatial mesh points; $\Delta\xi = 0.0125$) and $N = 5000$ (time mesh points; $\Delta t = 0.008$). As mentioned above, this test shows that the code is capturing very well the (effectively linear) dispersive regime when $\alpha$ is small enough.

We repeat the experiment above for $\alpha = 0.001$, $\beta = 0.0005$ and $t = 40$. Dispersion has been decreased substantially. Now the effective hyperbolic regime is clearly observed in figure 3.2.

**Experiment 2 (Flat channel and a solitary wave):**

We now study system (3.27) in the case that $M \equiv 1$, $0 < \alpha \ll 1$ (weakly nonlinear regime), and $0 < \beta \ll 1$ (weakly dispersive regime). Under these hypotheses it is possible to obtain an approximate solution of system (3.27) which has the analytical form

$$\eta(\xi, t) = A_1 \text{ sech}^2(B(\xi - Ct - \xi_o)) + A_2 \text{ sech}^4(B(\xi - Ct - \xi_o)), \tag{3.28}$$
$$u(\xi, t) = A \text{ sech}^2(B(\xi - Ct - \xi_o)),$$

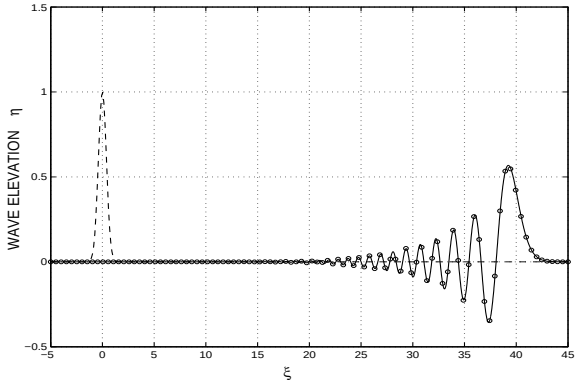


FIG. 3.1. *Dashed line: initial pulse* $\eta(\xi,0) = u(\xi,0) = e^{-\xi^2/0.3}$. *Solid line: numerical solution for* $\alpha = 0.001$, $\beta = 0.03$ *and* $t = 40$. *Dotted line: Exact solution.*

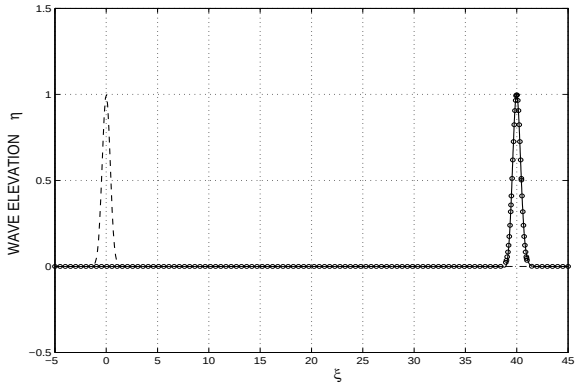


FIG. 3.2. *Dashed line: initial disturbance* $\eta(\xi,0) = u(\xi,0) = e^{-\xi^2/0.3}$. *Solid line: numerical solution for* $\alpha = 0.001$, $\beta = 0.0005$ *and* $t = 40$. *Dotted line: Initial Gaussian pulse translated to* $\xi = 40$.

where

$$A_1 = \frac{C^2-1}{\alpha C^2} = \frac{1}{C^2}, \quad A_2 = \frac{(C^2-1)^2}{\alpha C^2} = \frac{\alpha}{C^2}, \quad C = \sqrt{1+\alpha}, \quad A = \frac{C^2-1}{\alpha C} = \frac{1}{C},$$

and

$$B = \left\{ \frac{C^2-1}{(4/3)\beta C^2} \right\}^{1/2} = \left\{ \frac{\alpha}{(4/3)\beta C^2} \right\}^{1/2}.$$

Note that $A_1 + A_2 = 1$. See Wei and Kirby [69] for details.

In figure 3.3 we show the analytical solution $\eta$ given by equation (3.28) for $\alpha = \beta = 0.03$ and $t = 30$. The initial soliton position is set to be $\xi_o = 0$. The numerical solution is also included in this plot. The numerical parameters are $J = 2000$, $N = 2500$, $\Delta\xi = 0.025$, $\Delta t = 0.012$. Note that we have the same dispersion level as in the first of Experiment set 1. Now weak nonlinearity prevents the formation of an oscillatory tail.

Observe that the pulse's propagation velocity is $C \approx 1.0149$, in agreement with

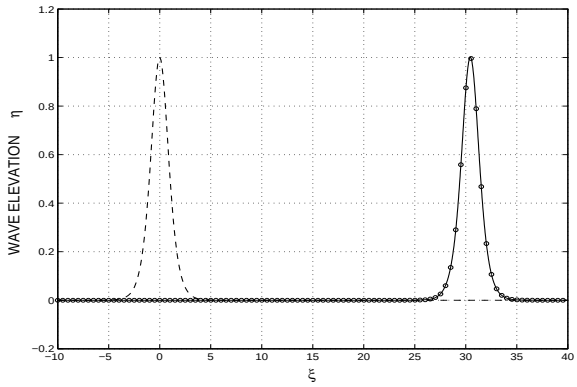


FIG. 3.3. *Solitary wave propagating over a flat bottom. Dashed line: initial disturbance* $\eta(\xi,0) = A_1\ sech^2(B\xi) + A_2\ sech^4(B\xi)$. *Solid line: numerical solution for* $\alpha = 0.03$, $\beta = 0.03$ *and* $t = 30$. *Dotted line: Analytical solution (3.28).*

solution (3.28). The code reproduces very well the weakly dispersive, weakly nonlinear evolution of the soliton.

**Experiment set 3 (Disordered orography/Hyperbolic regime:)** In experiments 1 and 2, in which the channel's bottom was assumed to be flat, the orography-dependent coefficient $M(\xi)$ was taken $M \equiv 1$. For variable depths the computation of function $M(\xi)$ involves the solution of a change of variables problem (conformal mapping) which is not an easy task. For this reason, in next experiments, the smooth orography coefficient $M(\xi)$ will be synthetized directly as a piecewise linear function, ignoring (for the time being) its dependence on the original orography. In [52] we describe in detail how a numerical conformal mapping tool [21] is used in order to obtain a "non-synthetic" $M(\xi)$. Nevertheless, synthetic $M(\xi)$ proves to be useful (i.e. efficient) for observing the phenomena we are interested in and for validating the theory. The synthetized orography coefficient is conceived as

$$M(\xi) = 1 + \delta\mu(\xi/\ell),$$

where $\mu$ is a mean-zero coefficient constructed using a random number generator. The fluctuation level is indicated by $\delta$ and its correlation length by $\ell$. In the following experiments we use $\delta = 0.5$ and $\ell = 0.1$.

The numerical experiments are performed over a channel defined in the interval [-15, 70]. The fluctuations of the synthetic coefficient $M(\xi)$ cover the interval [5, 45]. The data for the right propagating Gaussian is such that $\xi_o = -5$ and $\epsilon = 0.05$. The numerical solution is plotted as a function of the time-delay variable $\tau$ after propagating over 20 units of length and is presented in figure 3.4. Note the wave attenuation due to the orographic forcing. The transmited signal has amplitude 1.5 (smaller than 2.0, the initial amplitude). The agreement between the numerical solution of the full nonlinear equations (with small $\alpha$) and the linear theory is very good (figure 3.4(b)). We also point out an outstanding feature of the theory, not noticed in previous work [8]. The linear hyperbolic ODA approximation is able to capture the forward scattering radiation, which is the incoherent coda behind the transmitted Gaussian. Theory and numerical experiment agree over the delay time interval up to $\tau = 10$ approximately.

To verify the robustness of the theory we increase the size of the disordered

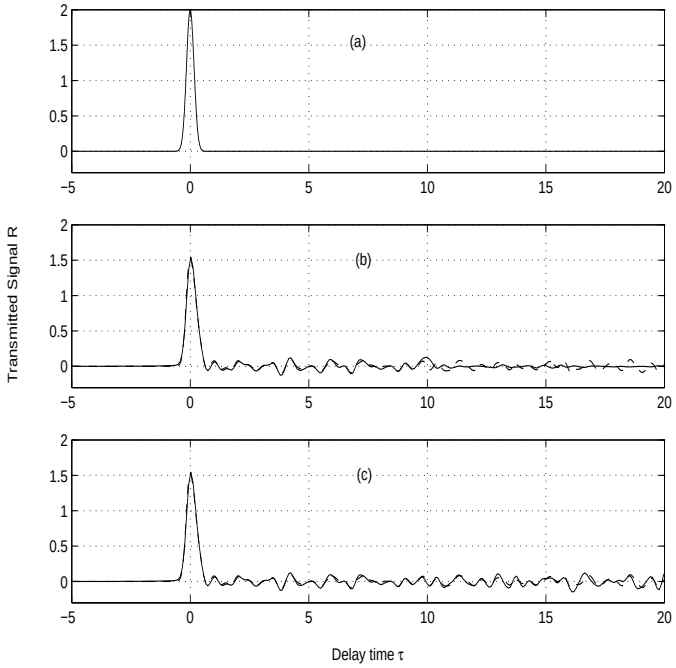


FIG. 3.4. *Pulse propagating over a synthetic disordered rapidly-varying topography. (a) Initial disturbance* $R(0,\tau) = 2e^{-\tau^2/0.05}$. *(b) Solid line: O'Doherty-Anstey approximation (3.26) for* $X = 5$. *Dashed line: Numerical solution for* $\alpha = 0.001$, $\beta = 0$ *at* $\xi = 20$. *(c) Solid line: O'Doherty-Anstey approximation (3.26) for* $X = 20$. *Dashed line: Numerical solution at* $\xi = 20$ *and* $\alpha$, $\beta$ *as in (b).*

medium's slab used in the invariant imbedding theory (namely the variable $X$). In figure 3.4(c) we plot the same numerical solution as above but compared with a theoretical result using an increased slab size (up to $X = 20$). The approximate theory captures an even larger segment of the forward scattering radiation beyond $\tau = 15$.

**Experiment set 4 (Disordered orography/Dispersive regime:)** This set of experiments is important for two reasons: **(A):** it shows that we are able to properly compute the interaction of dispersive water waves with rapidly varying orographies. With previously known Boussinesq models (such as [63]) this was not possible. The classic Boussinesq equation [63] is not valid for orographies with large slopes. Moreover, its variable coefficient multiplies the highest derivative term and this generates numerical noise as the orography's slope increases. This has been shown for a periodic topography in [52]. The same experiment was performed for the terrain-following Boussinesq system where the metric term is positioned away from the third order (dispersive) term. No numerical noise was observed. **(B):** it is also important because we illustrate the theoretical results in the regime for which they were deduced. Hence these linear experiments validate the nonlinear numerical model for the terrain-following Boussinesq equation in the presence of a random orography. This is important also since the code will be used (as a scientific computing tool) beyond the regime of validity of the linear theory.

In the first experiment we consider the dispersion to be very weak ($\beta = 0.0005$). Figure 3.5(a) clearly shows that a very short oscillatory tail develops when the pulse

propagates in a flat channel. The final amplitude of the transmitted pulse is about 1.5. The amplitude decay in this case is entirely due to dispersion as discussed in appendix A through the Airy kernel. But in the presence of orographic forcing an additional attenuation is observed (figure 3.5(b)). In this case the final amplitude is about 1. Note that no Airy-like oscillatory tail develops. This was systematically observed in several experiments and can be explained through the concept of *localization* [56]. The localization length of a Fourier mode is a *characteristic propagation distance* after which the transmission coeficient is negligible. The bulk of the energy is in the reflected signal. Moreover high frequency components have small localization lengths. This means they are quickly filtered (back) by the disordered medium. In the context of the ODA theory this was phrased in a slightly different way by Berlyand and Burridge [8]. They called a layered random medium a *stratigraphic Gaussian filter*. As presented here, the transmitted pulse can be written as the convolution of its initial Fourier content with a Gaussian kernel. The Gaussian kernel is the leading order approximation to the kernel in (3.24) with $\beta = 0$ (see [52, 54]). Applying this notion to our current problem we have that disorder filters the higher part of the Fourier content of the incoming pulse. Hence the oscillatory tail (which is of high frequency content) has been converted into the incoherent part of the wave. Again the agreement between the numerical solution and the ODA theory is very good.

In the next validation experiment the level of dispersion has been increased 4 times ($\beta = 0.002$). In figure 3.6(a) we have the initial pulse profile and the numerical solution after propagation over 40 units of a flat channel. We observe a long oscillatory tail due to the higher dispersion level. Note that dispersion is not as small as the value of $\beta$ might indicate at first sight. After large propagation distances the (small) phase lag (at higher frequencies) has accumulated in a nontrivial fashion.

To compute the theoretical ODA approximation we need the incoming pulse in time at the origin. Actually we need its Fourier content $\hat{f}(\omega)$. To be consistent with our mathematical theory we position the initial Gaussian profile (in space) to left of the origin at time $t_o$, allow it to propagate over a flat portion of the channel and record it in time at the origin. The starting time $t_o$ is chosen so that the resulting pulse $f(\tau)$ be centered at $\tau = 0$. This gives us the correct incoming pulse (in time) for the theoretical formula to be used. Hence the incoming pulse displays a mild oscillatory tail as displayed by figure 3.6(a). In figure 3.6(b) we compare the numerical solution with the generalized ODA approximation. The dispersive wave attenuation can again be observed.

**Experiment set 5 (Disordered orography/Solitary wave:)** We are now in a position to explore the (linear) generalized ODA theory beyond its regime of validity. We consider a weakly nonlinear, weakly dispersive wave, namely a soliton. Using equations (3.28) it is easy to see that we have

$$f(\tau) = \left(\frac{1}{C^2} + \frac{1}{C}\right) \mathrm{sech}^2(B\tau) + \frac{\alpha}{C^2}\mathrm{sech}^4(B\tau),$$

in order to evaluate the ODA approximation (3.24).

In order to slowly push away from the regime of validity of our theory we choose small values for the respective parameters $\alpha = \beta = 0.001$. This amount of dispersion is enough to produce an oscillatory coda as was observed in previous experiments. But now, for the particular data considered, this coda will not appear due to the perfect balance between the $\alpha$ and $\beta$ terms. The oscillatory coda seen at figure 3.7(b) is due entirely to forward scattering of energy generated by the interaction of the soliton with

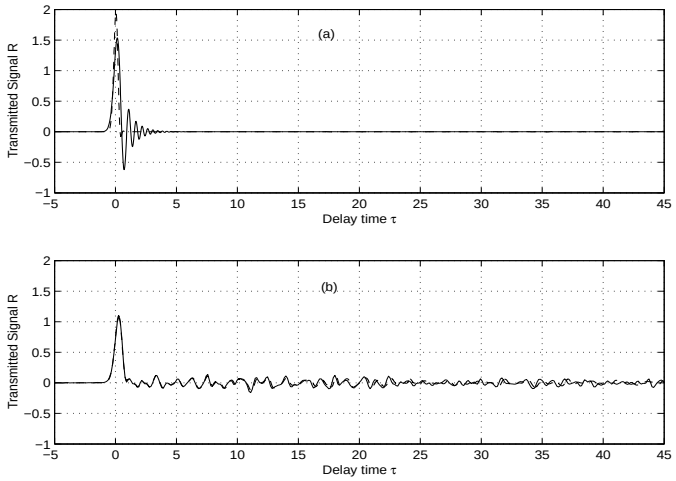


FIG. 3.5. *(a) Dashed line: Initial disturbance. Solid line: Solution for* $M \equiv 1$ *(flat bottom) at* $\xi = 40$. *(b) Pulse propagating over a synthetic disordered rapidly-varying orography. Dashed line: Numerical solution at* $\xi = 40$. *Solid line: Generalized O'Doherty-Anstey approximation (3.24) for* $X = 20$. *In all experiments* $\alpha = 0.001$, $\beta = 0.0005$.

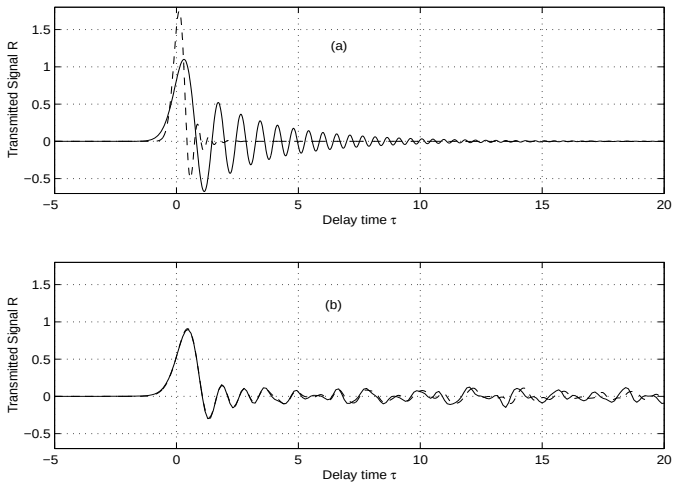


FIG. 3.6. *(a) Dashed line: Initial disturbance. Solid line: Solution for* $M \equiv 1$ *(flat bottom) at* $\xi = 40$. *(b) Pulse propagating over a synthetic disordered rapidly-varying orography. Dashed line: Numerical solution at* $\xi = 40$. *Solid line: Generalized O'Doherty-Anstey approximation (3.24) for* $X = 20$. *In all experiments* $\alpha = 0.001$, $\beta = 0.002$.

the disordered medium. Because the soliton is wider than the Gaussian (used before) we adopt $\ell = 0.6$. This keeps the wave/inhomogeneities ratio equal to approximately 10 ($\gamma = 0.1$) as in all other experiments. The orography coefficient covers the [5, 245] interval and the amplitude of fluctuations is $\delta = 0.5$. In figure 3.7(b) we present the excellent agreement between the theory and the numerical solution.

It is worthwhile recalling that the solitary wave (3.28) is an approximate solution to the Boussinesq equations as presented by Wei and Kirby [69] in their appendix. In [69] (page 255) they discuss solitary-wave propagation over a flat bottom and

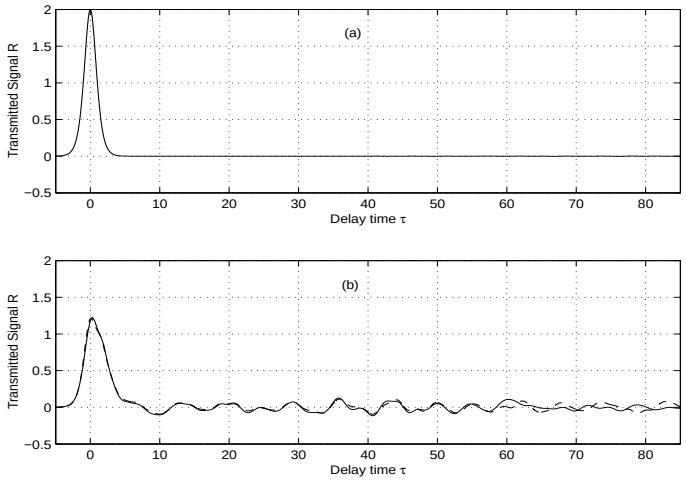


FIG. 3.7. *Soliton propagating over a synthetic disordered rapidly-varying orography. (a) Initial soliton $f(\tau)$. (b) Dashed line: Numerical solution for $\alpha = 0.001$, $\beta = 0.001$ at $\xi = 150$. Solid line: Generalized O'Doherty-Anstey approximation (3.24) for $X = 30$.*

analyse the effects, under the corresponding approximation, of increasing the soliton's amplitude (namely the nonlinearity parameter $\alpha$; there denoted by $\delta$). They observed that for $\alpha = 0.1$ the initial profile specified by (3.28) undergoes a rapid adjustment to a slightly higher solitary wave with a very small dispersive tail. This dispersive tail is not noticeable in their experiment ([69] FIG. 2(a)) after the soliton has propagated over 55 pulsewidths (450 length units). Nevertheless the amplitude of the tail and of the rapid deviation from the initial solitary wave height both increase with increasing $\alpha$. As explained in [69] this is partially because the fourth-order ordinary differential equation used to develop the analytical solution is only asymptotically equivalent to the Boussinesq model used in the computations. In particular for $\alpha = 0.3$ Wei and Kirby show that the corresponding evolution for (3.28) is far from a travelling wave solution.

As pointed out before the ODA theory developed is linear while these experiments are performed beyond the linear regime. Hence in our experiments we will gradually increase the values of $\alpha$ but we will be far from the "problematic regime" indicated by Wei and Kirby [69]. In our second experiment with solitons, and to further move away from the linear regime, we double the nonlinearity and dispersive parameters accordingly. We will now investigate the effect of different realizations of the medium. In figure 3.8 we present the results for 10 different realizations of the disordered topography. We observe the stabilization of the transmitted pulse: the pulse shaping of the front is independent of the specific realization. This has been proved for the linear hyperbolic case [41]. Stabilization in the linear dispersive regime has been recently proved in [28]. The present framework has been extended, through a stochastic analysis, to include stabilization [28] for the time-reversed refocusing of dispersive waves. No stabilization theory is yet available for solitons though.

As pointed out, the solitary wave profile (3.28) is not an exact travelling wave solution to the corresponding, constant coefficient, Boussinesq system. Nevertheless the balance between weak nonlinearity and weak dispersion is maintained for large time intervals. If dispersion were not present a Burgers-type nonlinearity ($\eta_t + \alpha\eta\eta_x =$

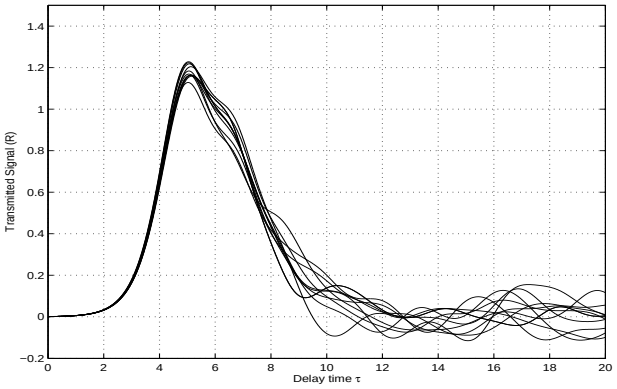


FIG. 3.8. *Transmitted pulse stabilization observed at a fixed medium's station ($\xi = 150$; 25 pulse widths). The same initial soliton ($\alpha = \beta = 0.002$) propagated over ten different realizations of the topography. The transmitted pulse shape is effectively deterministic while the coda is random.*

0) would force the solitary wave profile (3.28) to eventually break. For an initial profile denoted as $\eta(x,0) = f(x)$ the critical time $t_c$ is known to be $t_c = -1/(\alpha f')$, for the maximum value of the negative slope of $f(x)$. For $f(x)$ given by (3.28), with $\alpha = \beta = \varepsilon$, the maximum value of the negative slope is at $\tilde{x}$ such that $\tanh(B\tilde{x}) = -z$, where

$$z = \left(\frac{1 + C + 2\alpha}{3 + 3C + 10\alpha}\right)^{1/2},$$

$$f'(\tilde{x}) = -\left(\frac{3}{(1+\varepsilon)^3}\right)^{1/2}\left[\frac{1-z^2}{z^2}\left((1+C)z + 2\varepsilon(\frac{1-z^2}{z})\right)\right], \quad \text{with} \quad C = \sqrt{1+\varepsilon}$$

and $t_c \approx 1/(4\varepsilon)$. Hence if dispersion was switched off the solitary wave would break after 50 length units (approximately 8.33 pulse widths), when $\varepsilon = \alpha = 0.005$ as will be used in the following experiment.

In our last experiment we further increase nonlinearity and dispersion to be $\alpha = \beta = 0.005$. The result is presented in figure 3.9. As observed in Experiment set 4, disorder attenuates the effect of dispersion. This is again confirmed in this weakly nonlinear experiment. Note the soliton steepening at the wave front due to the attenuation of the dispersive mechanism. The attenuated wave front predicted by the linear theory does not match the nonlinear numerical front as before. Note also that dispersion has not been fully switched off or else a shock would have formed in finite time according to the discussion above. More experiments with solitary waves, including time reversal and refocusing are presented in [52].

The study of solitary waves over disordered topography is of great interest. In this work we have only presented scientific computing results. A complete theoretical understanding is of interest. An article by Garnier, Muñoz and Nachbin is in final preparation. Theoretical results for nonlinear localization and soliton propagation in random media is recent and more focused on the nonlinear Schrödinger (NLS) equation. A very good source of references can be found through the work of Garnier [32, 33].

We have formulated a generalization of the O'Doherty-Anstey theory for linear weakly dispersive waves. The theory has been valited numerically and pushed beyond

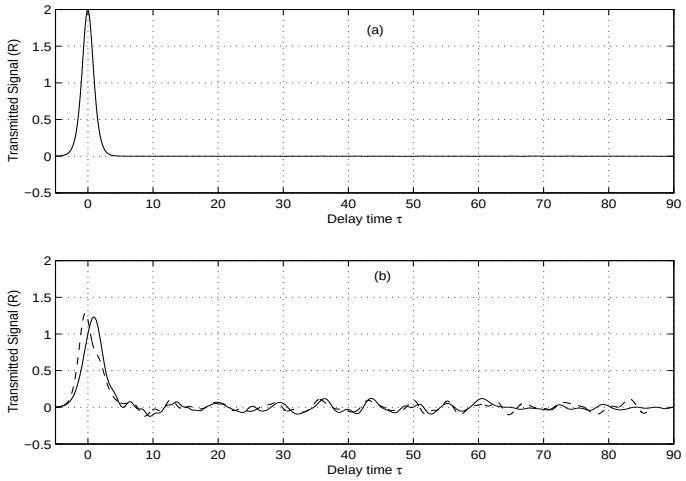


FIG. 3.9. *Soliton propagating over a synthetic disordered rapidly-varying orography. (a) Initial soliton $f(\tau)$. (b) Dashed line: Numerical solution for $\alpha = 0.005$, $\beta = 0.005$ at $\xi = 150$. Solid line: Generalized O'Doherty-Anstey approximation (3.24) for $X = 30$.*

its linear regime of validity. This work has stimulated new theoretical results in the stochastic formulation for time-reversed dispersive wave refocusing [28] and also for the ODA and time-reversed refocusing [29] of weakly nonlinear hyperbolic waves. The authors in [29] have shown that, to leading order, the transmitted pulse is governed by a viscous Burgers equation. The "apparent viscosity" depends on statistics of the random medium. This important result reports on a weakly nonlinear ODA theory for nondispersive waves. Therefore the regularizing effect is entirely due to the "apparent viscosity" promoted by the disorederd orography. Details of the "apparently viscous" theory, including additional nonlinear experiments are presented in [29].

**4. SOLUTION ASYMPTOTICS: RANDOM APPROACH.** As before we consider the linear Boussinesq equation that describes the evolution of surface waves in shallow channels [57]: recall that $\eta$ is the wave elevation and $u$ is the depth-averaged velocity, $\xi$ and $t$ are the space and time coordinates, respectively. The spatial variations of the coefficient $M$ are imposed by the bottom profile

$$M(\xi) = 1 + \varepsilon m(\xi)$$

where 1 stands for the constant mean depth, the dimensionless small parameter $\varepsilon$ characterizes the size of the relative fluctuations of the bottom modeled by the zero-mean stationary random process $m(\xi)$. The process $m$ is assumed to be bounded by a deterministic constant, differentiable, and mixing in a sense that will be precised later on. We may think for instance that $m(\xi) = f(\nu(\xi))$ where $f$ is a smooth bounded function and $\nu$ is a stationary Gaussian process with Gaussian autocorrelation function and we assume that $\mathbb{E}[f(\nu(0))] = 0$. Note that in that case the realizations of the process $\nu$ are of class $\mathcal{C}^\infty$ almost surely. This hypothesis is consistent with the terrain-following coordinate system adopted.

We consider the problem on the finite slab $-L \leq \xi \leq 0$ where boundary conditions will be imposed at $-L$ and 0 corresponding to a pulse entering the slab from the right at $\xi = 0$. The quantities of interest, the transmitted and reflected waves, will be observed in time at the extremities $\xi = -L$ and $\xi = 0$, respectively.

We consider a pulse whose support is comparable to the correlation length of the random medium, that is of order 1. In order to see the effect of the small random fluctuations, we consider a long distance of propagation. As we shall see the interesting regime arises when the propagation distance is of order $1/\varepsilon^2$.

**4.1. The propagating modes of the homogeneous Boussinesq equation.** As mentioned in the previous section we now show how exact right and left propagating modes can be established in the case of a homogeneous medium. Consider the homogeneous Boussinesq equation (with $m \equiv 0$):

$$\frac{\partial \eta}{\partial t} + \frac{\partial u}{\partial \xi} = 0 \tag{4.1}$$

$$\frac{\partial u}{\partial t} + \frac{\partial \eta}{\partial \xi} - \beta \frac{\partial^3 u}{\partial \xi^2 \partial t} = 0 \tag{4.2}$$

with a smooth initial condition

$$u(t=0,\xi) = u_0(\xi), \qquad \eta(t=0,\xi) = \eta_0(\xi).$$

Taking the space Fourier transform

$$\check{u}(t,k) = \frac{1}{2\pi} \int u(t,\xi) \exp(ik\xi) dz, \qquad \check{\eta}(t,k) = \frac{1}{2\pi} \int \eta(t,\xi) \exp(ik\xi) dz,$$

the Boussinesq equation (4.1-4.2) reduces to a set of ordinary differential equations:

$$\frac{\partial \check{\eta}}{\partial t} = ik\check{u} \tag{4.3}$$

$$\left(1 + \beta k^2\right) \frac{\partial \check{u}}{\partial t} = ik\check{\eta}. \tag{4.4}$$

Introducing the pulsation corresponding to the wavenumber $k$ through the *dispersion relation*

$$\omega(k) = \frac{k}{\sqrt{1+\beta k^2}} \tag{4.5}$$

we get closed form expressions for the solutions:

$$\check{u}(t,k) = \frac{1}{2}\left(\check{u}_0(k) + \frac{\omega}{k}\check{\eta}_0(k)\right)\exp(i\omega t) + \frac{1}{2}\left(\check{u}_0(k) - \frac{\omega}{k}\check{\eta}_0(k)\right)\exp(-i\omega t)$$
$$\check{\eta}(t,k) = \frac{1}{2}\left(\frac{k}{\omega}\check{u}_0(k) + \check{\eta}_0(k)\right)\exp(i\omega t) - \frac{1}{2}\left(\frac{k}{\omega}\check{u}_0(k) - \check{\eta}_0(k)\right)\exp(-i\omega t).$$

From these expressions we can conclude that any solution can be decomposed as the superposition of left-propagating modes $(u^{(l)}, \eta^{(l)})$ and right-propagating modes $(u^{(r)}, \eta^{(r)})$:

$$u(t,\xi) = u^{(r)}(t,\xi) + u^{(l)}(t,\xi)$$
$$\eta(t,\xi) = \eta^{(r)}(t,\xi) + \eta^{(l)}(t,\xi)$$

where

$$u^{(r)}(t,\xi) = \int \frac{1}{2}\left(\check{u}_0(k) + \frac{\omega}{k}\check{\eta}_0(k)\right)\exp\left(i\omega(k)t - ik\xi\right) dk$$

$$\eta^{(r)}(t,\xi) = \int \frac{k}{2\omega}\left(\check{u}_0(k) + \frac{\omega}{k}\check{\eta}_0(k)\right)\exp\left(i\omega(k)t - ik\xi\right)dk$$
$$u^{(l)}(t,\xi) = \int \frac{1}{2}\left(\check{u}_0(k) - \frac{\omega}{k}\check{\eta}_0(k)\right)\exp\left(-i\omega(k)t - ik\xi\right)dk$$
$$\eta^{(l)}(t,\xi) = -\int \frac{k}{2\omega}\left(\check{u}_0(k) - \frac{\omega}{k}\check{\eta}_0(k)\right)\exp\left(-i\omega(k)t - ik\xi\right)dk.$$

This decomposition will be used in the non-homogeneous case in the next subsection. In the previous section a hyperbolic mode decomposition was used as an approximation for the right and left propagating modes. Here the mode decomposition is exact for dispersive waves.

**4.2. Propagator formulation.** As in the previous section we first express the scattering problem as a two point boundary value problem in the frequency domain, and then rewrite it as an initial value problem in terms of the propagator. This is the standard approach for acoustic equations [4] that we generalize to the dispersive case using the decomposition introduced in the previous section. Note that here the incident wave (denoted by *inc*) is coming from the right, rather than from the left as in the deterministic modeling. This is only to show that the formulation is independent from either choice.

**4.3. Mode propagation in the frequency domain.** The next two subsections are basically the same of what we presented in the deterministic case. Some minor differences are observed but we repeat the mode decomposition formulation for completeness.

We consider the linearBoussinesq system and take the time Fourier transform

$$\hat{u}(\omega,\xi) = \frac{1}{2\pi}\int u(t,\xi)\exp(-i\omega t)dt, \qquad \hat{\eta}(\omega,\xi) = \frac{1}{2\pi}\int \eta(t,\xi)\exp(-i\omega t)dt$$

so that the system reduces to a set of ordinary differential equations:

$$\left(1-\beta\omega^2(1+\varepsilon m(\xi))\right)\frac{\partial\hat{\eta}}{\partial\xi} + i\omega\hat{u} - \varepsilon\beta\omega^2 m'(\xi)\hat{\eta} = 0 \tag{4.6}$$

$$\frac{\partial\hat{u}}{\partial\xi} + i\omega\left(1+\varepsilon m(\xi)\right)\hat{\eta} = 0 \tag{4.7}$$

where $m'$ stands for the spatial derivative of $m$. We introduce the wavenumber $k$ corresponding to the pulsation $\omega$:

$$k(\omega) = \frac{\omega}{\sqrt{1-\beta\omega^2}} \tag{4.8}$$

so that we can decompose the wave into *right-going modes* $A^\varepsilon$ and *left-going modes* $B^\varepsilon$ over distances of propagation of order $1/\varepsilon^2$. We show explicitly the dependence in the small parameter $\varepsilon$:

$$A^\varepsilon(\omega,\xi) = \frac{1}{2}\left(\hat{\eta}\left(\omega,\frac{\xi}{\varepsilon^2}\right) + \frac{k}{\omega}\hat{u}\left(\omega,\frac{\xi}{\varepsilon^2}\right)\right), \tag{4.9}$$

$$B^\varepsilon(\omega,\xi) = \frac{1}{2}\left(\hat{\eta}\left(\omega,\frac{\xi}{\varepsilon^2}\right) - \frac{k}{\omega}\hat{u}\left(\omega,\frac{\xi}{\varepsilon^2}\right)\right). \tag{4.10}$$

The modes $(A^\varepsilon, B^\varepsilon)$ satisfy:

$$\begin{aligned}\frac{\partial A^\varepsilon}{\partial \xi} &= -\frac{ik}{\varepsilon^2}A^\varepsilon - \frac{ik}{2\varepsilon}m(\xi/\varepsilon^2)(A^\varepsilon + B^\varepsilon) + \frac{\beta k^2}{2\varepsilon}m'(\xi/\varepsilon^2)(A^\varepsilon + B^\varepsilon)\\ &\quad -\frac{i\omega^2}{2k\varepsilon^2}\left(\frac{1}{1-\beta\omega^2(1+\varepsilon m(\xi/\varepsilon^2))} - \frac{1}{1-\beta\omega^2}\right)(A^\varepsilon - B^\varepsilon)\\ &\quad +\frac{\beta\omega^2}{2\varepsilon}m'(\frac{\xi}{\varepsilon^2})\left(\frac{1}{1-\beta\omega^2(1+\varepsilon m(\xi/\varepsilon^2))} - \frac{1}{1-\beta\omega^2}\right)(A^\varepsilon + B^\varepsilon) \qquad (4.11)\\ \frac{\partial B^\varepsilon}{\partial \xi} &= \frac{ik}{\varepsilon^2}B^\varepsilon + \frac{ik}{2\varepsilon}m(\xi/\varepsilon^2)(A^\varepsilon + B^\varepsilon) + \frac{\beta k^2}{2\varepsilon}m'(\xi/\varepsilon^2)(A^\varepsilon + B^\varepsilon)\\ &\quad -\frac{i\omega^2}{2k\varepsilon^2}\left(\frac{1}{1-\beta\omega^2(1+\varepsilon m(\xi/\varepsilon^2))} - \frac{1}{1-\beta\omega^2}\right)(A^\varepsilon - B^\varepsilon)\\ &\quad +\frac{\beta\omega^2}{2\varepsilon}m'(\frac{\xi}{\varepsilon^2})\left(\frac{1}{1-\beta\omega^2(1+\varepsilon m(\xi/\varepsilon^2))} - \frac{1}{1-\beta\omega^2}\right)(A^\varepsilon + B^\varepsilon) \qquad (4.12)\end{aligned}$$

We expand the last terms of the right-hand sides up to $O(\varepsilon^3)$ terms

$$\frac{\omega^2}{1-\beta\omega^2(1+\varepsilon m(\xi/\varepsilon^2))} - \frac{\omega^2}{1-\beta\omega^2} = \varepsilon\beta k^4 m(\xi/\varepsilon^2) + \varepsilon^2\beta^2 k^6 m^2(\xi/\varepsilon^2) + O(\varepsilon^3). \qquad (4.13)$$

We now look at the waves along the *frequency-dependent modified characteristics* defined by

$$a^\varepsilon(\omega,\xi) = A^\varepsilon(\omega,\xi)\exp\left(\frac{ik\xi}{\varepsilon^2}\right)\exp\left(-\frac{\varepsilon\beta k^2}{2}m(\frac{\xi}{\varepsilon^2}) - \frac{\varepsilon^2\beta^2k^4}{4}m(\frac{\xi}{\varepsilon^2})^2\right) \qquad (4.14)$$

$$b^\varepsilon(\omega,\xi) = B^\varepsilon(\omega,\xi)\exp\left(-\frac{ik\xi}{\varepsilon^2}\right)\exp\left(-\frac{\varepsilon\beta k^2}{2}m(\frac{\xi}{\varepsilon^2}) - \frac{\varepsilon^2\beta^2k^4}{4}m(\frac{\xi}{\varepsilon^2})^2\right) \qquad (4.15)$$

which satisfy the linear equation

$$\frac{\partial}{\partial\xi}\begin{pmatrix} a^\varepsilon \\ b^\varepsilon\end{pmatrix}(\omega,\xi) = Q^\varepsilon(\omega,\xi)\begin{pmatrix} a^\varepsilon \\ b^\varepsilon\end{pmatrix}(\omega,\xi). \qquad (4.16)$$

The complex $2\times 2$ matrix $Q^\varepsilon$ is given by:

$$Q^\varepsilon(\omega,\xi) = \begin{pmatrix} Q_1^\varepsilon(\omega,\xi) & Q_2^\varepsilon(\omega,\xi)e^{\frac{2ik\xi}{\varepsilon^2}} \\ \overline{Q_2^\varepsilon}(\omega,\xi)e^{-\frac{2ik\xi}{\varepsilon^2}} & \overline{Q_1^\varepsilon}(\omega,\xi)\end{pmatrix} \qquad (4.17)$$

with

$$Q_1^\varepsilon(\omega,\xi) = -\frac{ik}{2\varepsilon}\left(1+\beta k^2\right)m(\frac{\xi}{\varepsilon^2}) - \frac{i\beta^2k^5}{2}m^2(\frac{\xi}{\varepsilon^2}) + O(\varepsilon) \qquad (4.18)$$

$$\begin{aligned}Q_2^\varepsilon(\omega,\xi) &= -\frac{ik}{2\varepsilon}\left(1-\beta k^2\right)m(\frac{\xi}{\varepsilon^2}) + \frac{\beta k^2}{2\varepsilon}m'(\frac{\xi}{\varepsilon^2}) + \frac{i\beta^2k^5}{2}m^2(\frac{\xi}{\varepsilon^2})\\ &\quad +\frac{\beta^2k^4}{2}m(\frac{\xi}{\varepsilon^2})m'(\frac{\xi}{\varepsilon^2}) + O(\varepsilon). \qquad (4.19)\end{aligned}$$

The small terms of order $\varepsilon$ come from the $O(\varepsilon^3)$ term in the expansion (4.13).


FIG. 4.1. *Scattering problem.*

**4.4. Boundary values.** We assume that a left-going pulse is incoming from the right and is scattered into a reflected wave at $\xi = 0$ and a transmitted wave at $\xi = -L/\varepsilon^2$ (see Figure 4.1).

The incoming pulse shape is given by the elevation function $f(t)$ where $f$ is assumed to be a $L^1$ function compactly supported in the Fourier domain:

$$u_{inc}(t, \xi = 0) = -\int \frac{\omega}{k(\omega)} \hat{f}(\omega) \exp(i\omega t) d\omega$$
$$\eta_{inc}(t, \xi = 0) = \int \hat{f}(\omega) \exp(i\omega t) d\omega$$

with $\text{supp}(\hat{f}) \subset (-1/\sqrt{\beta}, 1/\sqrt{\beta})$. We also impose a radiation condition at $-L/\varepsilon^2$ corresponding to the absence of right-going wave at the left hand-side of the slab $[-L/\varepsilon^2, 0]$. The two-point boundary value problem consisting of the system (4.16) for $\xi \in [0, L]$ together with the conditions:

$$b^{\varepsilon}(\omega, \xi = 0) = \hat{f}(\omega), \quad a^{\varepsilon}(\omega, \xi = -L) = 0$$

is then well-posed.

**4.5. Propagator.** It is convenient to transform the two-point boundary value problem into an initial value problem by introducing the propagator $Y^{\varepsilon}(\omega, -L, \xi)$ which is a complex $2 \times 2$ matrix solution of

$$\frac{\partial Y^{\varepsilon}}{\partial \xi}(\omega, -L, \xi) = Q^{\varepsilon}(\omega, \xi) Y^{\varepsilon}(\omega, -L, \xi), \quad Y^{\varepsilon}(\omega, -L, \xi = -L) = Id_{\mathbb{C}^2}$$

such that

$$Y^{\varepsilon}(\omega, -L, \xi) \begin{pmatrix} a^{\varepsilon}(\omega, -L) \\ b^{\varepsilon}(\omega, -L) \end{pmatrix} = \begin{pmatrix} a^{\varepsilon}(\omega, \xi) \\ b^{\varepsilon}(\omega, \xi) \end{pmatrix}.$$

By the form (4.17) of the matrix $Q^{\varepsilon}$, if the column vector $(a^{\varepsilon}_1, b^{\varepsilon}_1)^T$ is solution of equation (4.16) with the initial conditions:

$$a^{\varepsilon}_1(\omega, -L) = 1, \quad b^{\varepsilon}_1(\omega, -L) = 0, \tag{4.20}$$

then the column vector $(\overline{b^{\varepsilon}_1}, \overline{a^{\varepsilon}_1})^T$ is another solution linearly independent of the first solution, so that the propagator matrix $Y^{\varepsilon}$ can be written as:

$$Y^{\varepsilon}(\omega, -L, \xi) = \begin{pmatrix} a^{\varepsilon}_1 & \overline{b^{\varepsilon}_1} \\ b^{\varepsilon}_1 & \overline{a^{\varepsilon}_1} \end{pmatrix} (\omega, \xi).$$

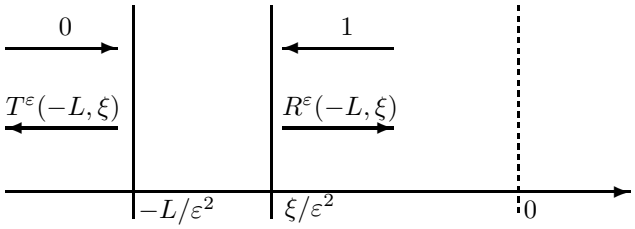


FIG. 4.2. *Reflection and transmission coefficients.*

Note also that the matrix $Q^\varepsilon$ has zero trace, so that the determinant of $Y^\varepsilon$ is conserved and $(a_1^\varepsilon, b_1^\varepsilon)$ satisfies the relation:

$$\det Y^\varepsilon = |a_1^\varepsilon|^2 - |b_1^\varepsilon|^2 = 1. \tag{4.21}$$

We define the *transmission and reflection coefficients* $T^\varepsilon(\omega,-L,\xi)$ and $R^\varepsilon(\omega,-L,\xi)$, respectively, for a slab $[-L,\xi]$ by (see also Figure 4.2):

$$Y^\varepsilon(\omega,-L,\xi)\begin{pmatrix} 0 \\ T^\varepsilon(\omega,-L,\xi)\end{pmatrix} = \begin{pmatrix} R^\varepsilon(\omega,-L,\xi) \\ 1\end{pmatrix}.$$

In terms of the propagator entries they are given by:

$$R^\varepsilon(\omega,-L,\xi) = \frac{\overline{b_1^\varepsilon}}{\overline{a_1^\varepsilon}}(\omega,\xi), \quad T^\varepsilon(\omega,-L,\xi) = \frac{1}{\overline{a_1^\varepsilon}}(\omega,\xi)$$

and they satisfy the closed form nonlinear differential system:

$$\frac{\partial R^\varepsilon}{\partial \xi} = 2Q_1^\varepsilon(\omega,\xi)R^\varepsilon - e^{-\frac{2ik\xi}{\varepsilon^2}}\overline{Q_2^\varepsilon}(\omega,\xi)(R^\varepsilon)^2 + e^{\frac{2ik\xi}{\varepsilon^2}}Q_2^\varepsilon(\omega,\xi), \tag{4.22}$$

$$\frac{\partial T^\varepsilon}{\partial \xi} = -T^\varepsilon\left(e^{\frac{2ik\xi}{\varepsilon^2}}Q_2^\varepsilon(\omega,\xi)R^\varepsilon + Q_1^\varepsilon(\omega,\xi)\right), \tag{4.23}$$

with the initial conditions at $\xi = -L$:

$$R^\varepsilon(\omega,-L,\xi=-L) = 0, \quad T^\varepsilon(\omega,-L,\xi=-L) = 1.$$

Note that Eq. (4.21) implies the conservation of energy relation

$$|R^\varepsilon|^2 + |T^\varepsilon|^2 = 1 \tag{4.24}$$

and in turn the uniform boundedness of the transmission and reflection coefficients. Note also that $R^\varepsilon$ and $T^\varepsilon$ are the reflection and transmission coefficients for the modified characteristics (4.14-4.15). In terms of the real characteristics the reflection and transmission coefficients are $R^\varepsilon$ and $T^\varepsilon \exp(-ikL/\varepsilon^2)$, respectively.

**4.6. Probabilistic modeling and tools.** In the previous subsection we formulated the nonlinear evolution equations for the reflection and transmission coefficients $R^\varepsilon(\omega,-L,\xi)$ and $T^\varepsilon(\omega,-L,\xi)$. The corresponding vector fields depend on the matrix $Q^\varepsilon$ which has random coefficients. Hence under this **probabilistic modeling** $R^\varepsilon(\omega,-L,\xi)$ and $T^\varepsilon(\omega,-L,\xi)$ are interpreted as stochastic processes. Their evolution equations have been cast in a form such that Khasminskii's theorem [38] is readily applicable.

Khasminskii's theorem reads as follows: consider a system of ODEs, being an initial value problem with a random forcing, where $\omega$ represents an element (an event) in state space (probability space): $\omega \in (\Omega, \mathcal{A}, \mathcal{P})$. We are keeping Khasminskii's notation and this is not to be confused with the Fourier frequency denoted above. Consider a random system in the form

$$\frac{dx_\varepsilon}{dt} = \varepsilon F(t, x_\varepsilon; \omega), \qquad x_\varepsilon(0) = x_0$$

together with the system

$$\frac{dy}{d\tau} = \overline{F}(y), \qquad y(0) = x_0,$$

where $F(t, \cdot; \omega)$ is a stationary stochastic process, satisfying the ergodicity hypothesis among a few other technical considerations [38], where

$$\overline{F}(x) \equiv \lim_{T\to\infty} \frac{1}{T} \int_0^T \mathbb{E}\{F(t, x; \omega)\} dt.$$

Then

$$\sup_{0\le t} \mathbb{E}\{|x_\varepsilon(t) - y(t)|\} \sim \sqrt{\varepsilon} \quad \text{on the time scale } 1/\varepsilon.$$

When several time scales are present Kohler and Papanicolaou (c.f. references within [4, 11]) considered the system

$$\frac{dx_\varepsilon}{dt} = \frac{1}{\varepsilon} F(x_\varepsilon, t, \frac{t}{\varepsilon}, \frac{t}{\varepsilon^2}; \omega), \qquad x_\varepsilon(0) = x_0$$

where

$$F(\cdot, \cdot, \cdot, \frac{t}{\varepsilon^2}; \omega)$$

is a stochastic process with hypothesis similar to those in Khasminskii's theorem. Note that the process is on the fastest scale, which in the wave propagation problem represents the random medium's heterogeneities [4].

Through these theorems one is able to characterize for example $\mathbb{E}\{T^\varepsilon(\omega, -L, \xi)\}$ (at each Fourier frequency $\omega$) or $\mathbb{E}\{T^\varepsilon \bar{T}^\varepsilon\}$ as $\varepsilon \downarrow 0$ [4, 11]. In these expressions we have omitted the state space parameter $\omega$. From the conservation of energy relation these results also provide $\mathbb{E}\{R^\varepsilon \bar{R}^\varepsilon\}$. An excellent text with a detailed and comprehensive presentation of the mathematical technology for *Waves in Random Media* is due by the middle of 2006 and authored by Fouque, Garnier, Papanicolaou and Sølna [31].

**4.7. Quantities of interest.** The **probabilistic results** are then readily available to be used in an integral representations as follows. The transmitted wave at time $t$, denoted by $(u^\varepsilon_{tr}, \eta^\varepsilon_{tr})$, is the left-going wave which admits the following integral representation in terms of the transmission coefficients:

$$u^\varepsilon_{tr}(t, \xi = -\frac{L}{\varepsilon^2}) = -\int \frac{\omega}{k(\omega)} \hat{f}(\omega) T^\varepsilon(\omega, -L, 0) \exp\left(i\omega t - ik(\omega)\frac{L}{\varepsilon^2}\right) d\omega, \tag{4.25}$$

$$\eta^\varepsilon_{tr}(t, \xi = -\frac{L}{\varepsilon^2}) = \int \hat{f}(\omega) T^\varepsilon(\omega, -L, 0) \exp\left(i\omega t - ik(\omega)\frac{L}{\varepsilon^2}\right) d\omega. \tag{4.26}$$

Similarly, the reflected wave $(u^\varepsilon_{ref}, \eta^\varepsilon_{ref})$ can be expressed in terms of the reflection coefficients as:

$$u^\varepsilon_{ref}(t,\xi=0) = \int \frac{\omega}{k(\omega)} \hat f(\omega) R^\varepsilon(\omega,-L,0) \exp(i\omega t)\, d\omega, \tag{4.27}$$

$$\eta^\varepsilon_{ref}(t,\xi=0) = \int \hat f(\omega) R^\varepsilon(\omega,-L,0) \exp(i\omega t)\, d\omega. \tag{4.28}$$

By linearity of the integrals, the mean values (ensemble averages) of these propagating modes follow from the frequency-by-frequency analysis described above.

**4.8. Transmitted wavefront.** We give an integral representation for the *coherent transmitted wave front* observed at $\xi = -L/\varepsilon^2$ around the effective arrival time $L/\varepsilon^2$. By (4.26), the transmitted elevation front is given by:

$$\eta^\varepsilon_{tr}(\frac{L}{\varepsilon^2}+t, \xi = -\frac{L}{\varepsilon^2}) = \int e^{i\omega t} e^{i(\omega-k(\omega))\frac{L}{\varepsilon^2}} \hat f(\omega) T^\varepsilon(\omega,-L,0) d\omega. \tag{4.29}$$

Due to dispersion, $k(\omega)$ is different from $\omega$ (see (4.8)). As a consequence, if $\beta = O(1)$, then the rapid phase $\exp(i(\omega - k(\omega))L/\varepsilon^2)$ makes the integral vanish as $\varepsilon \to 0$. This is in dramatic contrast with the hyperbolic case ($\beta = 0$) where the coherent transmitted wave persists in this regime as a manifestation of the well known O'Doherty-Anstey theory studied in [16, 42, 62] in various situations, and described earlier in the deterministic modeling.

In the dispersive case, the front will be present if the dispersion parameter $\beta$ is small enough. This has been characterized and observed numerically in [51, 52]. In particular, in the regime where $\beta = \varepsilon^2\beta_0$, we can derive its precise shape resulting from the interplay of randomness and dispersion. In that regime, by expanding the dispersion relation $\omega \mapsto k(\omega)$, we get that the front is given by:

$$\eta^\varepsilon_{tr}(\frac{L}{\varepsilon^2}+t, \xi = -\frac{L}{\varepsilon^2}) = \int e^{i\omega t} e^{-i\beta_0\omega^3 L} \hat f(\omega) T^\varepsilon(\omega,-L,0) d\omega + O(\varepsilon^2).$$

The transmission coefficients are given by $T^\varepsilon(\omega,-L,0) = 1/\overline{a^\varepsilon_1}(\omega,0)$ where $a^\varepsilon_1$ satisfies (4.16) with the initial conditions (4.20). In the case $\beta = \varepsilon^2\beta_0$, the entries of the matrix $Q^\varepsilon$ can be expanded as:

$$Q^\varepsilon_1(\omega,\xi)|_{\beta=\beta_0\varepsilon^2} = -\frac{ik}{2\varepsilon} m(\xi/\varepsilon^2) + O(\varepsilon),$$
$$Q^\varepsilon_2(\omega,\xi)|_{\beta=\beta_0\varepsilon^2} = -\frac{ik}{2\varepsilon} m(\xi/\varepsilon^2) + O(\varepsilon),$$

so that we get the same system as in the hyperbolic case up to terms of order $\varepsilon$. The limit of $\eta^\varepsilon_{tr}$ has been derived for the hyperbolic case with small fluctuations [4, 62]. In our case the derivation of the limit follows the same lines except for the deterministic phase $\exp(-i\beta_0\omega^3 L)$ due to the small dispersion. The process $(\eta^\varepsilon_{tr}(\frac{L}{\varepsilon^2} + t, \xi = -\frac{L}{\varepsilon^2}))_{t\in(-\infty,+\infty)}$ converges in the space of the continuous and bounded functions to [28]

$$\eta_{tr}(t) = \int \hat f(\omega) \exp\left( i\omega(t - \frac{\sqrt{\gamma(0)}}{2} B_L) - \frac{\omega^2\gamma(\omega)}{4} L - i\beta_0\omega^3 L \right) d\omega,$$

where $B_L$ is a standard Brownian motion and $\gamma$ is

$$\gamma(\omega) = \int_0^\infty \mathbb{E}[m(0)m(\xi)]e^{2i\omega\xi}dz. \tag{4.30}$$

We immediately can interpret the first term in the exponential as a random time of arrival for the wave. The time of arrival depends on the particular realization of the medium, which is manifested by the Brownian motion term. The second term is diffusive-like and universal in the sense that it does not depend on the particular realization for the heterogeneities. Finally the third term is dispersive. Using convolution operators the transmitted front can be written in a simpler form:

$$\eta_{tr}(t) = f * K\left(t - \frac{\sqrt{\gamma(0)}}{2}B_L\right), \tag{4.31}$$

which means that a random Gaussian centering appears through the Brownian motion $B_L$ while the pulse shape spreads in a deterministic way through the convolution by the kernel $K$

$$K(t) = K_r * K_d(t).$$

Here $K_d$ is the scaled Airy function [1]

$$K_d(t) = \frac{1}{(3\beta_0 L)^{1/3}}\mathrm{Ai}\left(-\frac{t}{(3\beta_0 L)^{1/3}}\right)$$

and the Fourier transform of $K_r$ is

$$\hat{K}_r(\omega) = \exp\left(-\frac{\omega^2\gamma(\omega)L}{4}\right).$$

Note that the kernel $K$ depends both on randomness (through the function $\gamma$) and on dispersion (through the parameter $\beta_0$). This stochastic formulation is in agreement with the formulation presented in [51, 52] for small $\beta$. Again, as expected, the theory indicates the **apparent diffusion** of waves propagating in a random medium. Diffusion is characterized by the Gaussian kernel $\hat{K}_r(\omega)$. The diffusion coefficient depends on $\gamma$.

Observe that a dispersion parameter $\beta = O(1)$ or even $O(\varepsilon^p)$ with $p < 2$ leaves a fast phase in the integral representation of the transmitted front as can be seen in (4.29). This implies a dramatic spreading of the pulse for a propagation distance of order $1/\varepsilon^2$, so that no coherent front pulse can be observed at the output $\xi = -L/\varepsilon^2$. The apparent diffusion experiments in this case are similar to those presented earlier for the deterministic case. In [28, 52] we have several dispersive experiments illustrating the expressions given above. One can then clearly see the effect of both the diffusive and dispersive kernels.

## 5. NUMERICAL MODELS.

**5.1. Numerical scheme for the Boussinesq models.** We present the numerical scheme employed in computing the solutions to the one parameter family of Boussinesq systems (1.30)-(1.31). This scheme is basically the same as that developed by Wei and Kirby [69] and which we adapted in [52]. For simplicity, let

$$g(\xi) = \frac{1}{2}(Z_0^2(\xi) - 1).$$

First we rewrite the Boussinesq system

$$M(\xi)\eta_t + \left[\left(1 + \frac{\alpha\ \eta}{M(\xi)}\right) u\right]_\xi + \frac{\beta}{2}\left[\left(Z_0^2 - \frac{1}{3}\right) u_{\xi\xi}\right]_\xi = 0, \tag{5.1}$$

$$u_t + \eta_\xi + \alpha\left(\frac{u^2}{2M^2(\xi)}\right)_\xi + \frac{\beta}{2}(Z_0^2 - 1)u_{\xi\xi t} = 0. \tag{5.2}$$

in a more convenient way, as

$$\begin{aligned} \eta_t &= E(\eta, u), \\ V_t &= F(\eta, u), \end{aligned} \tag{5.3}$$

where

$$\begin{aligned} E(\eta, u) &= -\frac{1}{M(\xi)}\left(\left(1 + \frac{\alpha\eta}{M(\xi)}\right) u\right)_\xi + \frac{\beta}{M(\xi)}((g(\xi) + 1/3)u_{\xi\xi})_\xi, \\ F(\eta, u) &= -\eta_\xi - \frac{\alpha}{2}\left(\frac{u^2}{M(\xi)^2}\right)_\xi. \end{aligned} \tag{5.4}$$

The intermediate (auxiliary) variable $V$ is defined as

$$V = u - \beta g(\xi) u_{\xi\xi}.$$

We now approximate the solution of system (5.3) by using a high-order predictor-corrector solver. The space-time domain $\{\xi \in [\xi_1, \xi_J]\ ,\ t \geq 0\}$ will be discretized by $\xi_j = \xi_1 + (j-1)\Delta\xi,\ 1 \leq j \leq J$ and $t_n = (n-1)\Delta t,\ 1 \leq n \leq N_0$, respectively. The discretizations of the variables $u, \eta, V$ will be denoted by $u_j^n, \eta_j^n, V_j^n$. As mentioned above this strategy is basically the same as that presented in [52], the difference being that the Sturm-Liouville type problem, for inverting the change of variables from $V$ back to $u$, has the new coefficient $g(\xi)$.

As suggested in [69] we use a third-order explicit Adams-Bashforth solver to produce a predicted value for $(V, \eta)$ and then a fourth-order implicit Adams-Moulton scheme is applied to obtain a corrected solution. The **predictor** is given by

$$\begin{aligned} \eta_j^{n+1} &= \eta_j^n + \frac{\Delta t}{12}(23E_j^n - 16E_j^{n-1} + 5E_j^{n-2}), \\ V_j^{n+1} &= V_j^n + \frac{\Delta t}{12}(23F_j^n - 16F_j^{n-1} + 5F_j^{n-2}). \end{aligned} \tag{5.5}$$

The notation $E_j^n = E(\eta_j^n, u_j^n)$ and $F_j^n = F(\eta_j^n, u_j^n)$ is used. The first-order derivatives in equation (5.4) and $u_{\xi\xi\xi}$ are approximated by appropriate differences schemes [52].

Recall that for evaluating the fluid velocity $u_j^{n+1}$ we must solve the (spatial) ordinary differential equation

$$u - \beta g(\xi) u_{\xi\xi} = V, \tag{5.6}$$

which is forced by the known left handside $V_j^{n+1}$. The second derivative in equation (5.6) is discretized by a centered approximation giving rise to a tridiagonal system of algebraic equations which is solved very efficiently. We remark that this system's matrix is constant in time and thus only one $LU$ decomposition must be performed at the starting point.

When the boundary values $u_1^{n+1}$ and $u_J^{n+1}$ and $\eta_1^{n+1}$ and $\eta_J^{n+1}$ are required, we use the linear radiation conditions (B. Engquist and A. Majda [24])

$$\begin{aligned} u_t - u_\xi = 0, \quad \text{at} \quad \xi = \xi_1, \\ u_t + u_\xi = 0, \quad \text{at} \quad \xi = \xi_J, \end{aligned} \tag{5.7}$$

where $\xi_1$ and $\xi_J$ denote the left and right ends of the computational domain. Analogous conditions are applied on the function $\eta$. Conditions above play the role of absorbing the waves arriving at the boundaries of the computational domain. This allows us to perform numerical simulations without introducing a too long computational spatial domain. These conditions work well for small amplitude waves propagating in the linear regime in the absence of a topography. Therefore at the extremes of our computational domain the channel has a short flat bottom region.

Once the predicted values $\eta_j^{n+1}, u_j^{n+1}$ are obtained we compute $E_j^{n+1}, F_j^{n+1}$ from equations (5.4). The **corrected values** are calculated from

$$\begin{aligned} \eta_j^{n+1} &= \eta_j^n + \frac{\Delta t}{24}(9E_j^{n+1} + 19E_j^n - 5E_j^{n-1} + E_j^{n-2}), \\ V_j^{n+1} &= V_j^n + \frac{\Delta t}{24}(9F_j^{n+1} + 19F_j^n - 5F_j^{n-1} + F_j^{n-2}), \end{aligned} \tag{5.8}$$

where the quantities at level $n+1$ are computed iteratively by using the predicted approximation as the initial guess. The new $u_j^{n+1}$ is computed from $V_j^{n+1}$ as in the predictor step. We stop the iteration process when the relative error between two successive corrected values $\eta^{n+1}$, $u^{n+1}$ and $\eta^{(n+1)^*}$, $u^{(n+1)^*}$ are smaller than a given tolerance.

To verify the stability and the accuracy of this numerical scheme we perform a simulation with constant depth, taking alternatively $Z_0 = \sqrt{1/5}$, $Z_0 = 0.469$.

As mentioned earlier, adapting the strategy described in [69] an approximate solitary wave solution for system (1.30)-(1.31) can be written as

$$\begin{aligned} \eta(\xi,t) &= A_1 sech^2(B(\xi - Ct - \xi_o)) + A_2 sech^4(B(\xi - Ct - \xi_o)), \\ u(\xi,t) &= A sech^2(B(\xi - Ct - \xi_o)), \end{aligned} \tag{5.9}$$

where

$$A_1 = \frac{C^2-1}{\frac{3}{2}\alpha(Z_0^2 - 1/3 - (Z_0^2-1)C^2)}, \quad A_2 = -\frac{(C^2-1)^2(\frac{1}{2}(Z_0^2-1/3) + (Z_0^2-1)C^2)}{\alpha C^2(Z_0^2 - \frac{1}{3}) - (Z_0^2-1)C^2}$$

$$B = \left\{ \frac{C^2-1}{2\beta(Z_0^2 - 1/3 - (Z_0^2-1)C^2)} \right\}^{1/2}, \quad A = \frac{C^2-1}{\alpha C}.$$

The parameter $\xi_o$ indicates the location of the solitary wave at $t = 0$. The constant $C$ is the wave velocity and it is calculated from the equation

$$(5.10)2(Z_0^2-1)C^6-((3+2\alpha)(Z_0^2-1)+\frac{2}{3})C^4+2\alpha(Z_0^2-\frac{1}{3})C^2+Z_0^2-\frac{1}{3}=0.$$

Observe that the wave speed and the amplitude of the wave are connected. We point out that (5.9) corresponds to an exact solitary wave for the Benney-Luke type equation

$$\phi_{tt}-\phi_{\xi\xi}+\alpha(2\phi_\xi\phi_{\xi t}+\phi_t\phi_{\xi\xi})-\beta\left(\frac{Z_0^2-1/3}{2}\phi_{\xi\xi\xi\xi}-\frac{Z_0^2-1}{2}\phi_{\xi\xi tt}\right)=0,$$

which is formally equivalent to system (1.30)-(1.31) (with $u=\phi_\xi$) up to order $O(\alpha,\beta)$.

We now perfom a numerical experiment. When $\alpha=\beta=0.03$, and $Z_0=\sqrt{1/5}$ or $Z_0=0.469$, the wave speed (computed from (5.10)) is approximately $C\approx 1.01485$. In the simulation the discretization parameters used were $\Delta\xi=0.0333$, $\Delta t=0.0267$ and the computational domain is taken as [0,100]. In these experiments, we observe that the solitary wave preserves its shape after propagating over a distance of approximately 13 times its effective width ($\ell_p\approx 6$). There is no indication of numerical attenuation nor spurious dispersion. The solitary wave speed coincides with good accuracy with the speed of the numerical solitary solution. This was systematically observed in several numerical experiments with different values of the parameters $\alpha$, $\beta$ and of the intermediate depth $Z_0$ in system (1.30)-(1.31). We remark that the dispersion and nonlinearity values $\alpha=\beta=0.03$ are not negligible [51, 52] in this problem. Thus, we conclude that the numerical scheme is describing very well both nonlinear and dispersive effects present in the (one parameter family) Boussinesq models (1.30)-(1.31).

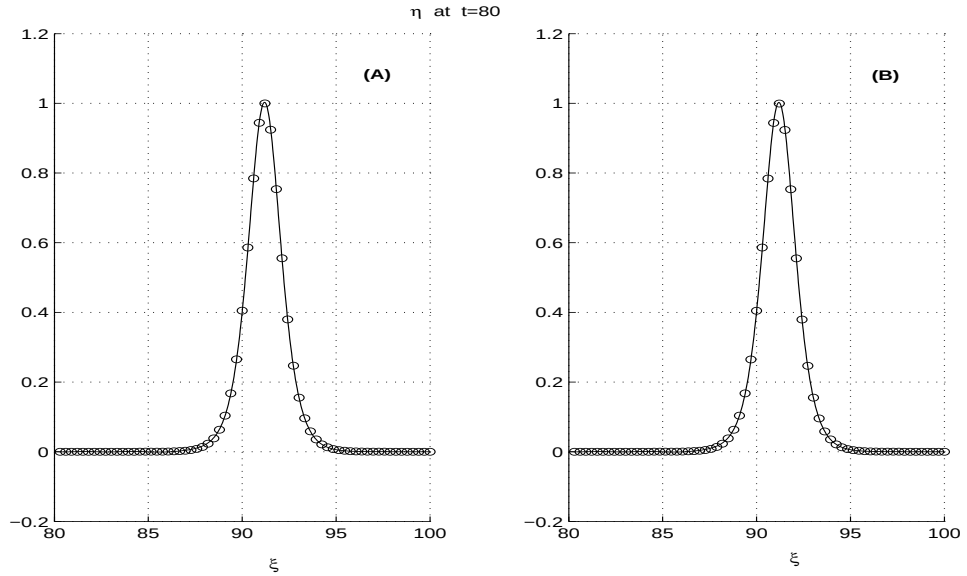


FIG. 5.1. *Propagation of the solitary wave for model (1.30)-(1.31) with $\alpha=\beta=0.03$. Convention: solid line indicates the numerical solution and the dots profile (5.9).* **(A)** *Boussinesq model with depth parameter $Z_0=\sqrt{1/5}$.* **(B)** *with $Z_0=0.469$.*

**5.2. Preconditioning through complex variables.** In this subsection we show how the range of eigenvalues can be changed by reformulating the dispersive system of partial differential equations. Namely by going from a cartesian to a curvilinear coordinate system [57]. In some sense this strategy has already been explored successfully, as for example, by Hou, Lowengrub and Shelley [37]. Hou *et al.* used an equal arclength spacing in their mathematical formulation for the evolution of Lagrangian particles along a fluid interface. Their clever change of variables (from a nonuniform distribution to an equally spaced one) removed the problem's stiffness by eliminating high frequency components generated due to particle compression. Here we use a disordered (conformal mapping) change of variables [57]. The new coordinate system removes the stiffness promoted along the domain's boundary due the presence of the orography's microscale. Namely in the new coordinate $\xi$ the mesh is equally spaced while the smooth metric term $M(\xi)$ incorporates the disorder, hence eliminating (by averaging) some high frequency components. Another advantage is that the variable coefficient, and its derivatives, move away from the equation's highest derivative (i.e. the third order dispersive term) and positions itself at the first order transport term.

To put the above comments in a more quantitative framework we start with the (cartesian) linear version of the dispersive model by Peregrine [63]:

$$\begin{aligned} &\eta_t + \left[(h(x/\gamma)\ u)\right]_x = 0, \\ &u_t + \eta_x + \beta\left(\frac{h^2(x/\gamma)}{6}u_{xxt} - \frac{h(x/\gamma)}{2}\partial_x^2(h(x/\gamma)\ u_t)\right) = 0. \end{aligned} \tag{5.11}$$

This system is valid when

$$O\left(\frac{\delta n'(x/\gamma)}{2\pi\sqrt{\beta}}\right) \ll \gamma. \tag{5.12}$$

Taking a Fourier transform in time we have that

$$\begin{aligned} &(-i\omega)\hat{\eta} + (h(x/\gamma)\ \hat{u})_x = 0, \\ &(-i\omega)\hat{u} + \hat{\eta}_x = \beta\left[\frac{h(x/\gamma)}{2}\left(-i\omega h(x/\gamma)\hat{u}\right)_{xx} - \frac{h^2(x/\gamma)}{6}(-i\omega)\hat{u}_{xx}\right]. \end{aligned} \tag{5.13}$$

Using the first equation we can rewrite it as a first order system

$$\begin{aligned} &\hat{u}_x = -(\frac{h_x}{h})\ \hat{u} + (\frac{i\omega}{h})\ \hat{\eta}, \\ &\hat{\eta}_x = \frac{1}{1-\frac{\beta}{3}\omega^2 h}\left[i\omega\left(1 - \frac{\beta}{6}hh_{xx} + \frac{\beta}{3}h_x^2\right)\hat{u} + \left(\frac{\beta}{3}\omega^2 h_x\right)\hat{\eta}\right], \end{aligned} \tag{5.14}$$

where $h_x \equiv h'/\gamma$. The characteristic polynomial for the variable coefficient matrix is

$$p(\lambda) = \lambda^2 - \lambda\left[\frac{h_x}{h} - \frac{\frac{\beta}{3}\omega^2 h_x}{1-\frac{\beta}{3}\omega^2 h}\right] + \frac{\omega^2}{h}\left[\frac{1 - \frac{\beta}{6}hh_{xx} + \frac{\beta}{3}h_x^2}{1-\frac{\beta}{3}\omega^2 h}\right] = 0.$$

The eigenvalues are

$$\lambda^{\pm}(x) = -\frac{h'}{\gamma}\left(1 - \frac{1/2}{1-\frac{\beta}{3}\omega^2 h}\right) \pm \left[\frac{i\omega/h(x/\gamma)}{\sqrt{1-\omega^2\frac{\beta}{3}h(x/\gamma)}}\right] \times$$

$$\times \sqrt{1 - \frac{\beta}{6\gamma^2} h h'' + \frac{\beta}{3\gamma^2} h'^2 - \frac{h'^2}{\gamma^2} \frac{(1 - (2/3)\beta\omega^2 h)^2}{h(1 - \frac{\beta}{3}\omega^2 h)}}. \tag{5.15}$$

If $h(x/\gamma) \equiv 1$ we recover the usual dispersion relation [70] for the wavenumber ($k = -i\lambda$) in terms of the frequency:

$$k^{\pm}(\omega) = \pm \frac{\omega}{\sqrt{1 - \omega^2 \frac{\beta}{3}}}.$$

In practice (i.e., in our experiments) the initial data is generated in space so that the frequencies are bounded by $(3/\beta)^{1/2}$:

$$\omega^{\pm}(k) = \pm \frac{k}{\sqrt{1 + k^2 \frac{\beta}{3}}}.$$

On the other hand for the regime of long waves ($\beta \ll 1$) propagating over topographies of decreasing length scales ($\gamma \downarrow$) we observe that

$$\lambda^{\pm}(x) \sim O\left(\frac{1}{\gamma}\right) \pm i \left[\frac{\omega/h(x/\gamma)}{\sqrt{1 - \omega^2 \frac{\beta}{3} h(x/\gamma)}}\right] \cdot \sqrt{1 - O\left(\frac{1}{\gamma^2}\right)}. \tag{5.16}$$

The leading order imaginary part plays the role of a local wavenumber, in analogy to the unforced case. Note that as $\gamma$ tends towards the microscale the spectrum will broaden. But we should bear in mind that this system was not designed to capture rapidly varying topographies. Nevertheless in [52] we saw the onset of numerical noise even in the proper regime of validity.

In contrast now consider the linear terrain-following Boussinesq system

$$\begin{aligned} M(\xi)\eta_t + u_\xi &= 0, \\ u_t + \eta_\xi - \frac{\beta}{3} u_{\xi\xi t} &= 0, \end{aligned} \tag{5.17}$$

which was designed for a broad range of topographies [57]. Taking a Fourier transform in time we have that

$$\begin{aligned} (-i\omega) M(\xi)\hat{\eta} + \hat{u}_\xi &= 0, \\ (-i\omega)\hat{u} + \hat{\eta}_\xi - (-i\omega)\frac{\beta}{3}\hat{u}_{\xi\xi} &= 0. \end{aligned} \tag{5.18}$$

By differentiating the first equation and substituting into the second we obtain the following system of ordinary differential equations:

$$\begin{aligned} \hat{u}_\xi &= i\omega \; M(\xi) \; \hat{\eta}, \\ \hat{\eta}_\xi &= \frac{1}{1 - \omega^2 \frac{\beta}{3} M(\xi)} \left( i\omega \;\; \hat{u} + \omega^2 \frac{\beta}{3} M'(\xi) \;\; \hat{\eta} \right). \end{aligned} \tag{5.19}$$

The characteristic polynomial for the variable coefficient matrix of this system is

$$p(\lambda) = \lambda^2 - \lambda \left[\frac{\omega^2 \frac{\beta}{3} M'(\xi)}{1 - \omega^2 \frac{\beta}{3} M(\xi)}\right] + \frac{\omega^2 M(\xi)}{1 - \omega^2 \frac{\beta}{3} M(\xi)}.$$

The eigenvalues are

$$\lambda^{\pm}(\xi) = \frac{\omega^2\frac{\beta}{3}M'(\xi) \pm i\omega\sqrt{M(\xi)}\sqrt{(1-\omega^2\frac{\beta}{3}M(\xi)) - \beta^2\frac{\omega^2 M'^2(\xi)}{36M(\xi)}}}{2(1-\omega^2\frac{\beta}{3}M(\xi))}. \tag{5.20}$$

If $M(\xi) \equiv 1$ we recover the usual dispersion relation. Recall that the metric term $M(\xi)$ is controlled by two parameters and defined by

$$M(\xi;\beta,\gamma) \equiv 1 + \frac{\pi}{4\sqrt{\beta}} \int_{-\infty}^{\infty} \frac{\delta n(x(\xi_0,-\sqrt{\beta})/\gamma)}{cosh^2\frac{\pi}{2\sqrt{\beta}}(\xi_0-\xi)} d\xi_0 = O(1).$$

Moreover

$$M'(\xi) \equiv \frac{\pi}{2\sqrt{\beta}} \int_{-\infty}^{\infty} \delta n(x(\frac{2\sqrt{\beta}}{\pi}s,-\sqrt{\beta})/\gamma)\frac{senh(s-\tilde{s})}{cosh^3(s-\tilde{s})}ds, \quad \text{where } \tilde{s} \equiv \frac{\pi}{2\sqrt{\beta}}\xi.$$

Since $\delta < 1$ and $|n| < 1$, clearly for small $\beta$, $|M'|$ scales as

$$|M'(\xi)| \sim \frac{\pi}{\sqrt{\beta}}\int_0^{\infty} \frac{senh(s-\tilde{s})}{cosh^3(s-\tilde{s})}ds = \frac{\pi}{\sqrt{\beta}} \quad \Rightarrow \quad M'(\xi) = O(1/\sqrt{\beta}).$$

Using these results in the dispersion relation (for the eigenvalues) we have that

$$\lambda^{\pm}(\xi) \sim O(\sqrt{\beta}) \pm \; i \left[\frac{\omega\ \sqrt{M(\xi;\beta,\gamma)}}{\sqrt{1-\omega^2\frac{\beta}{3}M(\xi;\beta,\gamma)}}\right] \cdot \sqrt{1+O(\beta)}. \tag{5.21}$$

Again the leading order imaginary part plays the role of a local wavenumber, similar to the unforced case. But now the spectrum's range is not sensitive to the microscale as $\gamma \downarrow$. The metric term $M(\xi;\beta,\gamma)$ takes care of it. Moreover, for long waves ($\beta \ll 1$) the spectrum for the multiscale problem remains near the "unforced spectrum". The new mathematical formulation has **preconditioned the problem** regarding multiscale simulations.

We want to point out that the analysis presented above is not really in favor of the actual solution method for the terrain-following equation. Note that we differentiate $M(\xi)$ in order to obtain the dispersion relation. This is not needed in the solution of the linear equation. A more realistic linear stability analysis corresponds to analyzing the (numerically motivated [69]) setup given through

$$\begin{aligned} \eta_t &= E(\eta,u), \\ V_t &= F(\eta,u), \\ u - \frac{\beta}{3}u_{\xi\xi} &= V \end{aligned} \tag{5.22}$$

where

$$\begin{aligned} E(\eta,u) &= -\frac{1}{M(\xi)}u_\xi, \\ F(\eta,u) &= -\eta_\xi. \end{aligned}$$

The third equation (5.22) gives rise to a Sturm-Liouville problem due to the usage of an auxiliary function $V(\xi,t)$ in the evolution equations. This is typical in the analysis of KdV-type equations [20] where the solution of (5.22) is given by

$$u(x,t) = \frac{1}{2}\sqrt{\frac{3}{\beta}}\int_{\infty}^{\infty} e^{\sqrt{\frac{3}{\beta}}|x-s|}\ V(s,t)ds.$$

On the other hand for the linear Boussinesq system in cartesian coordinates [69]

$$\begin{aligned} \eta_t &= \tilde{E}(\eta, u), \\ \tilde{V}_t &= F(\eta, u), \\ u - \frac{\beta}{2}(hu)_{xx} + \frac{\beta}{6}h^2 u_{xx} &= \tilde{V}, \end{aligned} \tag{5.23}$$

where

$$\begin{aligned} \tilde{E}(\eta, u) &= -(h(x/\gamma)u)_x, \\ F(\eta, u) &= -\eta_x. \end{aligned}$$

The associated Sturm-Liouville problem from (5.23) is nontrivial, containing rapidly varying disordered coefficients and its derivatives.

**5.3. Numerical schemes for the linear potential theory equations.** We consider the scaled **linear** ($\alpha = 0$) water wave equations:

$$\beta\phi_{xx} + \phi_{yy} = 0 \qquad in \;\; \Omega$$

$$at \;\; y \;=\; 0 \;\; \left\{ \begin{array}{lcl} \phi_t &=& -\eta \\ \eta_t &=& \frac{1}{\beta}\phi_y \end{array} \right.$$

with the "impermeability" condition along the topography given by

$$\phi_y \;+\; \frac{\beta}{\gamma}\, H'(x/\gamma)\; \phi_x \;=\; 0.$$

The harmonic part of this problem can be recast in the form of a Boundary Integral Equation (BIE) through Green's third identity [55]:

$$\sqrt{\beta}\; \theta_{\mathbf{P}} \;\; \phi(\mathbf{P}) \;\; = \;\; \oint_{\partial\Omega} \; (\; \phi(\mathbf{Q}) \; \frac{\mathrm{d}\, \ln\rho}{\mathrm{d}\bar{\mathrm{n}}} \;-\; \phi_{\bar{\mathrm{n}}}(\mathbf{Q}) \; \ln\rho \;)\; \mathrm{d}\mathbf{Q},$$

where $(x_Q, y_Q) \equiv \mathbf{Q} \in \partial\Omega$, $\rho^2 \;=\; (x_P - x_Q)^2 \;+\; \beta(y_P - y_Q)^2$ and

$$\theta_{\mathbf{P}} \;\; = \;\; \left\{ \begin{array}{ll} \pi & \text{if } \mathbf{P} \in \text{smooth part of } \partial\Omega \\ \textit{internal angle} & \text{if } \mathbf{P} \in \text{corner of } \partial\Omega \\ 2\pi & \text{if } \mathbf{P} \in \Omega. \end{array} \right.$$

The scaled normal derivative is defined as $\phi_{\bar{n}} \equiv (\beta\partial_x\phi, \partial_y\phi) \cdot \vec{n}$. The BIE is solved by using the Boundary Element Method (BEM). The functional relation between the Dirichlet and Neumann data is approximated by finite elements along the BIE [55]. This leads to numerical dispersion as will be indicated below. A linear system arises when using the collocation method for the residual of the boundary element approximation. This system is dense, nonsymmetric and ill-conditioned. In [56, 58, 55] accurate results where obtained by using double precision on a supercomputer (about 28 digits of precision).

One of the advantages of the BEM, as opposed to the Finite Difference Method, is that we may consider the normal derivative $\phi_{\bar{n}}$ as a nodal parameter, that is, as an unknown of the algebraic system of equations. This is an advantage for boundaries of complex shape as the ones considered here. Note also that this enables the linear free

surface equations to be interpreted as a system of Ordinary Differential Equations (ODE) in time:

$$\frac{d\phi}{dt}(x_j,t) = -\eta(x_j,t)$$

$$\frac{d\eta}{dt}(x_j,t) = \frac{1}{\beta}\mathcal{F}[\phi]\ (x_j,t)$$

where $\mathcal{F}[\phi]$ indicates symbolically that $\phi_y$ has a functional dependence on $\phi$. Hence solving the BIE is like computing the vector field of these "ODEs" at each time step.

The evolution scheme in time is done through an implicit scheme. For the kinematic condition at $t^{n+1/2}$ we adopt the trapezoidal rule:

$$\frac{\eta^{n+1} - \eta^n}{\Delta t} = \frac{1}{\beta}\frac{\phi_y^{n+1} + \phi_y^n}{2} + O(\Delta t^2).$$

For the dynamic condition, also at $t^{n+1/2}$, we use

$$\frac{\phi^{n+1} - \phi^n}{\Delta t} = -\left[\eta^n + \frac{\Delta t}{2\beta}\left(\theta\ \phi_y^{n+1} + (1-\theta)\ \phi_y^n\right)\right] + O(\Delta t^2),$$

where $\theta$ is the implicit scheme's parameter. In Nachbin and Papanicolaou [56] it was shown that numerical dispersion is kept to a minimum if $\theta = 1/6$. This scheme was proposed by Liu and Liggett [43] with an empirical value of $\theta = 0.17$, which is very close to $1/6$. We have only one numerical differentiation (in t) and the local truncation error is $\mathrm{O}(\Delta t^3)$ on both free surface conditions.

In contrast through the $DtN$ formulation presented in curvilienar coordinates $\xi - \zeta$ we may write the linear free surface conditions in the form

$$\frac{d\phi}{dt}(\xi_j,t) = -\eta(\xi_j,t)$$

$$\frac{d\eta}{dt}(\xi_j,t) = \frac{1}{\beta}DtN_0[\phi](\xi_j,t),$$

where $DtN_0$ denotes the linear Dirichlet-to-Neumann operator as before:

$$DtN_0[\varphi](\xi) = \sum_{\kappa\neq 0} 2\pi\kappa\tanh(2\pi\kappa\sqrt{\beta})\mathbf{F}_\kappa[\varphi]e^{2\pi i\kappa\xi}.$$

This expression is exact. In contrast with the BEM this procedure has several advantages:

(a) we only need to use two FFTs to calculate the normal derivative with great efficiency; in the BEM a dense nonsymmetric system had to be solved at each time step.

(b) the normal derivative of the potential is calculated with spectral accuracy and, for a well resolved surface wave, numerical dispersion is absent.

(c) as a consequence of the previous comment we use an explicit ($\theta = 0$) evolution scheme along the free surface without observing any kind of numerical phase lag.

(d) the use of a curvilinear coordinate system in the presence of highly corrugated boundaries improves numerical stability, namely acting as a preconditioner [52, 59].

More details on this scheme will be provided in the next section. The following numerical experiments corroborate with the comments above.

We consider a Gaussian pulse for the velocity potential's initial profile:

$$\varphi(\xi) = e^{-(\xi-\xi_0)^2/\ell_p^2}, \tag{5.24}$$

where the parameter $\ell_p$ controls the pulse's width and therefore how broadband its Fourier content is. For the other initial condition along the FS, let $\phi_t(\xi,0,0) \equiv \psi(\xi)$ and we choose $\widehat{\psi}(k) = -i\omega\widehat{\varphi}(k)$ so that the initial wave is rightgoing. The corresponding free surface elevation is therefore the derivative of a Gaussian.

We consider four levels of dispersion ($\beta = 0.01, 0.1, 1,$ e 10) and compare the numerical evolution with the exact solution. We take (5.24) with $\ell_p = \sqrt{0.3}$ together with the following discretization parameters: $\Delta\xi = 0.0625$, for a total of $J = 1024$ nodes in space; $\Delta t = 0.01$ for a total of $N = 4500$ steps in time. As mentioned all experiments where done with the explicit scheme ($\theta = 0$) presented above.

The numerical experiments are presented in figures 5.2 and 5.3, where the solid line represents the numerical solution and the dots the exact values. The agreement is very good. In particular as we increase the dispersion level the Airy-like oscillatory behavior is captured very accurately.

We are in the process of extending the numerical scheme for the nonlinear regime. Muñoz Grajales and Nachbin [51, 52] have thoroughly tested a Boussinesq solver for the terrain-following Boussinesq system [57]. In the next subsection the DtN-spectral method presented here will be compared with the family of Boussinesq solvers, as for example the one related to the system suggested by Quintero and Muñoz Grajales [65]. All these models are different Padé approximations to the full dispersion relation

$$\omega^2 = \frac{k}{\sqrt{\beta}}\tanh[k\sqrt{\beta}].$$

For example the Boussinesq model in [51, 52] is such that

$$\omega^2 = \frac{k^2}{1+\frac{1}{3}\beta k^2}.$$

This is equivalent to the regularized Korteweg-de Vries equation, also known as the BBM model [6]. Of particular interest, we have observed that in the presence of a rapidly varying disordered topography, small differences on how the full dispersion relation is truncated affect the dynamics of the wave's rapidly fluctuating components. This is considered below.

**5.4. Full versus reduced model.** Consider the linear equations from

$$\beta\phi_{\xi\xi} + \phi_{\zeta\zeta} = 0, \quad \text{for} \quad 0 < \zeta < 1, \tag{5.25}$$

$$\eta_t - \frac{1}{\beta M(\xi)}\phi_\zeta = 0, \quad \text{at} \quad \zeta = 1, \tag{5.26}$$

$$\eta + \phi_t = 0, \quad \text{at} \quad \zeta = 1, \tag{5.27}$$

$$\phi_\zeta = 0, \quad \text{at} \quad \zeta = 0, \tag{5.28}$$

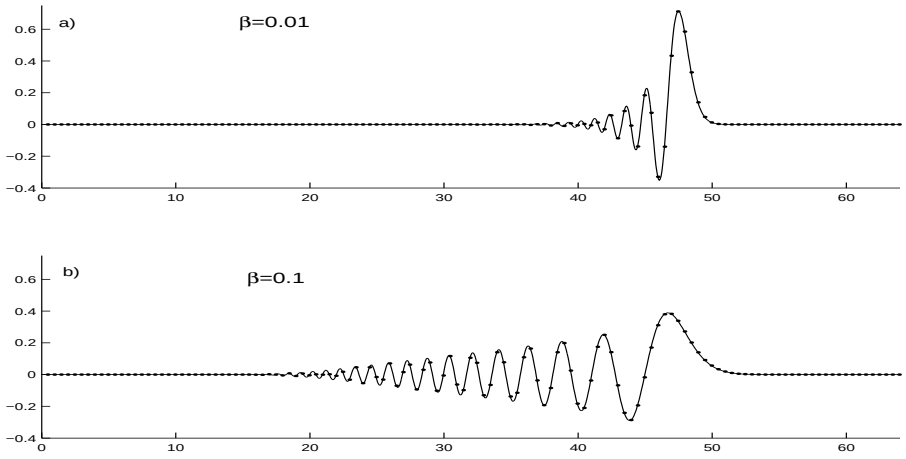


FIG. 5.2. *Snapshot for a propagating velocity potential: two weakly dispersive regimes.*

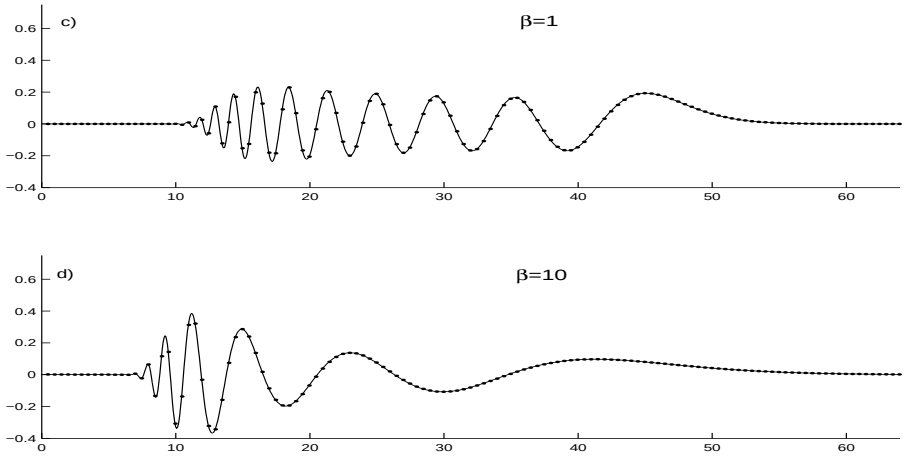


FIG. 5.3. *Snapshot for a propagating velocity potential: dispersion fully developed.*

subject to the initial conditions

$$\phi(\xi,1,0)=\phi_0(\xi), \quad \eta(\xi,0)=\eta_0(\xi).$$

At the time stage $(n+1)\Delta t$ we discretize the equations at the free surface $\zeta=1$ by

$$\frac{\eta^{n+1}-\eta^n}{\Delta t}-\frac{\phi_\zeta^{n+1}+\phi_\zeta^n}{2\beta M(\xi)}=O(\Delta t^2), \tag{5.29}$$

$$\frac{\phi^{n+1}-\phi^n}{\Delta t}+\eta^n+\frac{\Delta t}{2\beta M(\xi)}\phi_\zeta^n=O(\Delta t^2). \tag{5.30}$$

This scheme in time is basically the same as used in [58, 55, 56] and given above for the BEM. Having an expression for the $DtN_0$ operator enables writing a highly efficient and highly accurate numerical scheme, without any truncation errors in space. By

the construction of the $DtN_0$ operator presented the normal derivative at the free surface can be computed through

$$\phi_\zeta(\xi,1,t)=\frac{1}{2\pi}\int_{-\infty}^{\infty}k\sqrt{\beta}tanh(\sqrt{\beta}k)\hat{\phi}(k,1,t)e^{ik\xi}dk. \tag{5.31}$$

This expression is exact and automatically satisfies Laplace's equation (5.25). Moreover it can be easily evaluated through the FFT algorithm as indicated above. Here the hat denotes the Fourier transform with respect to the spatial coordinate $\xi$. In conclusion at any fixed time $t$ equation (5.31) transforms Dirichlet data ($\phi(\xi,1,t)$) into the corresponding Neumann data along the (linear) free surface of the fluid ($\zeta=1$).

Now we will compare model (1.30)-(1.31) with $Z_0=0.469$ (the optimal value of the depth parameter, c.f. section 1.4), the terrain-following Boussinesq system (1.25)-(1.26), both with the linear ($\alpha=0$) potential theory equations in curvilinear coordinates (1.19)-(1.22). This will be performed through a suite of numerical experiments performed by using the Boussinesq solvers described above. We only consider the linear regime for the potential theory equations in order to fully focus on the dispersion issues discussed earlier. Simulations with the full nonlinear potential equations will appear in a future work.

Given a pair $(f,g)$ of initial data for the potential theory equations (1.19)-(1.22) we will explain how to compute the corresponding initial data for the Boussinesq systems (1.30)-(1.31) and (1.25)-(1.26). This is the main difficulty in comparing the solutions of these models because the dependent variables are not the same. Recall that the Boussinesq models require monitoring the velocity at an intermediate depth. We proceed as follows.

Let $\Omega$ denote the rectangle bounded by $\zeta=0$, $\zeta=1$, $\xi=0$ and $\xi=L$, $L>0$. Let us give the free surface data $(\phi,\eta)$ for equations (1.19)-(1.22). Then we compute the corresponding initial potential profile $\phi(\xi,Z_0,0)$ (at the depth $\zeta=Z_0$ and time $t=0$) by the contour integral

$$\phi(\xi,\zeta=Z_0,0)=\frac{1}{2\pi\sqrt{\beta}}\oint_{\partial\Omega}\left(\phi(Q,0)G_{\bar{n}}(P,Q)-\phi_{\bar{n}}(Q,0)G(P,Q)\right)dQ. \tag{5.32}$$

We use the notation: $P=(\xi,Z_0)$, $Q=(\tilde{\xi},\tilde{\zeta})$, $\phi_{\bar{n}}=(\beta\phi_\xi,\phi_\zeta).\vec{n}$ ($\vec{n}$ denotes the outer normal vector at the boundary $\partial\Omega$), with the Green's function

$$G(\xi,\zeta,\tilde{\xi},\tilde{\zeta})=\frac{1}{2}ln((\xi-\tilde{\xi}^2+\beta(\zeta-\tilde{\zeta})^2)+\frac{1}{2}ln((\xi-\tilde{\xi}^2+\beta(\zeta+\tilde{\zeta})^2). \tag{5.33}$$

We recall that equation (5.32) is a consequence of Green's third identity. Details can be found in [58, 55, 56]. Note also that kernel $G$ is such that $G_{\bar{n}}=0$ at the channel bottom $\zeta=0$ and $\Delta_{(\xi,\zeta)}G(P,Q)=\delta_P(Q)$, where $\delta_P(Q)$ represents the Dirac delta function. Now, since $\phi_\zeta=0$ at the bottom $\zeta=0$, and assuming that $\phi,\phi_{\bar{n}}$ tend to zero when $|\xi|\to\infty$, we have that when $L\to\infty$, the contour integral in (5.32) needs only to be evaluated along the free surface $\zeta=1$. Namely,

$$\phi(\xi,\zeta=Z_0,0)=\frac{1}{2\pi\sqrt{\beta}}\int_{-\infty}^{\infty}\left(\phi(\tilde{Q},0)G_{\bar{n}}(P,\tilde{Q})-\phi_{\bar{n}}(\tilde{Q},0)G(P,\tilde{Q})\right)d\tilde{\xi}, \tag{5.34}$$

where $\tilde{Q}=(\tilde{\xi},1)$. By using the Method of Images (for the Green's function) we reduce the number of grid points along the contour by at least 50 percent.The bottom

*does not need to be discretized* and its effect is built into the (smooth) free surface coefficient $M(\xi)$. Once the initial velocity potential is computed by the numerical evaluation of the integral, the initial value for the velocity of the Boussinesq model (1.30)-(1.31) is calculated as $u(\xi,0) = u_0(\xi) = \phi_\xi(\xi, Z_0, 0)$. We remark that the wave elevation at $t = 0$, $\eta(\xi,0) = \eta_0(\xi)$ coincides in both models.

**5.4.1. Constant depth experiments.** The goal of our first experiment is to give evidence of some results from the dispersion analysis performed for the Boussinesq models considered, in respect to the potential theory equations (1.19)-(1.22). This is done in the case where the depth is constant. We set $\beta = 0.2$ and $\alpha = 0.001$, i.e. we have nontrivial dispersion and the regime is effectively linear.

To keep our focus on the full dispersion relation we solve the linear potential theory equations (5.25)-(5.28) on the computational domain $[0, 20\pi]$, with $\Delta t = 0.0063$ and 8192 FFT points in the spatial mesh (where $\Delta\xi = 0.00767$). The boundary conditions are periodic but no activity will be observed at the extremes of the interval $[0, 20\pi]$. The initial conditions are

$$\Phi(\xi,1,0) = \Phi_0(\xi) = \sqrt{\frac{10}{\pi}} e^{-5(\xi-20)^2},$$
$$\eta(\xi,0) = \eta_0(\xi) = -10\sqrt{\frac{10}{\pi}}(\xi-20)e^{-5(\xi-20)^2}.$$

These conditions produce right and left going waves when $\beta \neq 0$. Nevertheless the left going wave tends to zero as $\beta \downarrow 0$ [55, 70]. Remark that once the solution to the equations (5.25)-(5.28) are known, then the initial fluid velocity for the Boussinesq models is computed through the equation (5.34) as explained above. The parameters for solving the system (1.25)-(1.26) are $\Delta t = 0.0063$, $\Delta\xi = 0.0077$. In figure 5.4 we superimpose the solutions of models (5.25)-(5.28) and (1.25)-(1.26) at time $t = 25$. We observe that they coincide with good accuracy in the interval [36,50] corresponding to the wavefront, namely of low wavenumber content [70]. As expected, the signals in the interval [5,35] differ due to the analytical (not numerical!) truncation errors introduced by neglecting the terms of order $O(\beta^2)$ in the Boussinesq model (1.30)-(1.31).

In figure 5.5 the solution of system (1.30)-(1.31) with the optimal value of the depth parameter $Z_0 = 0.469$ is compared with the original equations (5.25)- (5.28). The numerical parameters are the same as before. In contrast to the previous experiment, the solutions match with good accuracy in the whole interval [5,50]. The Boussinesq system (1.30)-(1.31) captures well the dispersive details of the oscillatory coda of the propagating signal. In figure 5.4 the mismatch along the coda is due to the large phase errors as depicted in figure 1.4.

These experiments are in agreement with the linear dispersion analysis performed.

**5.4.2. Highly variable topography.** We have tested the different models over a flat bottom and now we are in a position to perform experiments in the presence of an irregular bottom. We will consider two levels of dispersion in the models. The variable coefficient is taken to be of the form

$$M(\xi) = 1 + \delta n(\xi/\gamma),$$

where $n(\xi/\gamma)$ is a mean-zero piecewise linear function constructed by using a random number generator in the interval [-1,1] and $\delta$ measures the amplitude of the fluctuations. The constant $\gamma$ measures the relative scale of variation of the bottom

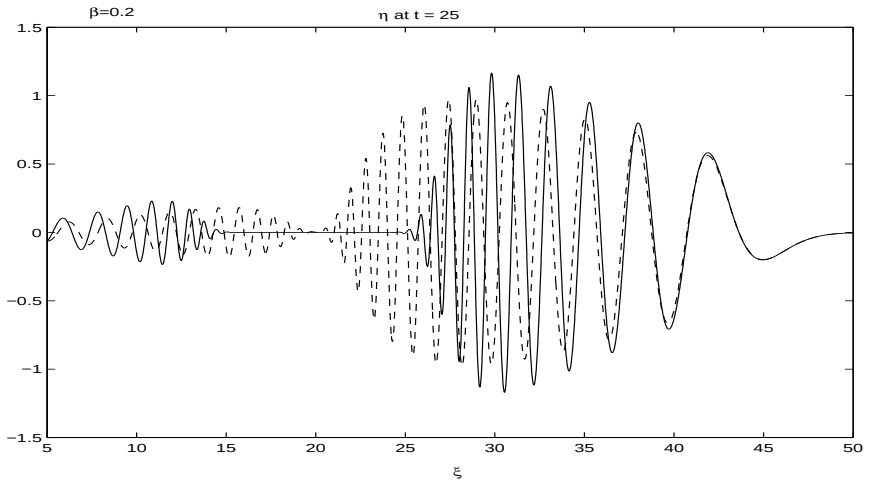


FIG. 5.4. *A rightgoing wavetrain to the right and a small leftgoing wavetrain to the left. Dashed line: Numerical solution of the terrain-following system (1.25)-(1.26). Solid line: Numerical solution of the equations (5.25)-(5.28). Model parameters:* $\alpha = 0$, $\beta = 0.2$.

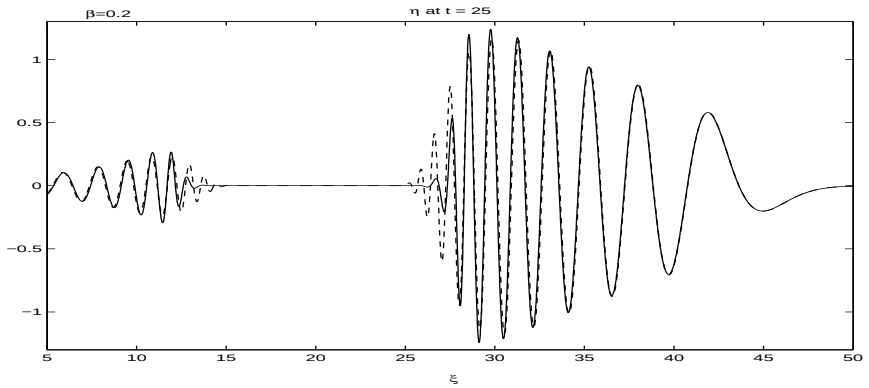


FIG. 5.5. *Dashed line: Numerical solution of system (1.30)-(1.31) with* $Z_0 = 0.469$. *Solid line: Numerical solution of the equations (1.19)-(1.22). Model parameters:* $\alpha = 0$, $\beta = 0.2$.

irregularities. We consider $\gamma$ to be small. This type of synthesized function has been employed by several researchers in order to validate pulse shaping theory in random media [8, 13, 27, 12]. Maintaining our focus on the linear regime we will examine how the reduced Boussinesq model captures the fine features of the topography in contrast with the potential theory model.

We start by fixing a very small dispersion parameter value $\beta = 0.002$. In figure 5.7 we compare the solution (i.e. a multiply scattered segment of the wave) of equations (5.25)-(5.28) with the solution of the model (1.25)-(1.26). The numerical parameters for equations (5.25)-(5.28) are $\Delta t = 0.01$, $2^{12}$ FFT points in space where the computational domain is [0,150]. The numerical parameters for solving system (1.25)-(1.26) are $\Delta\xi = 0.024$, $\Delta t = 0.0125$ and the computational domain is [0,120]. The irregularities of the coefficient $M(\xi)$ covers the interval [67,107] and the fluctuations are such

that $\delta = 0.5$ and $\ell = 0.1$. The initial conditions for equations (1.19)-(1.22) are

$$\Phi(\xi, 1, 0) = \Phi_0(\xi) = e^{-20(\xi-60)^2},$$
$$\eta(\xi, 0) = \eta_0(\xi) = -40(\xi - 60)e^{-20(\xi-60)^2}.$$

Here we are considering a shorter pulse (hence having a broader band in wavenumber space) to show the broad range of applicability of the numerical method and also of the dispersion analysis presented. The corresponding initial velocity at $Z_0 = \sqrt{1/3}$ for the system (1.25)-(1.26) is calculated from equation (5.34). Observe in figure 5.7 that the solutions of the original potential theory equations and the approximated Boussinesq model agree well. We are graphing the region where we measured the maximum value of the error. Over the rest of the computational domain the solutions

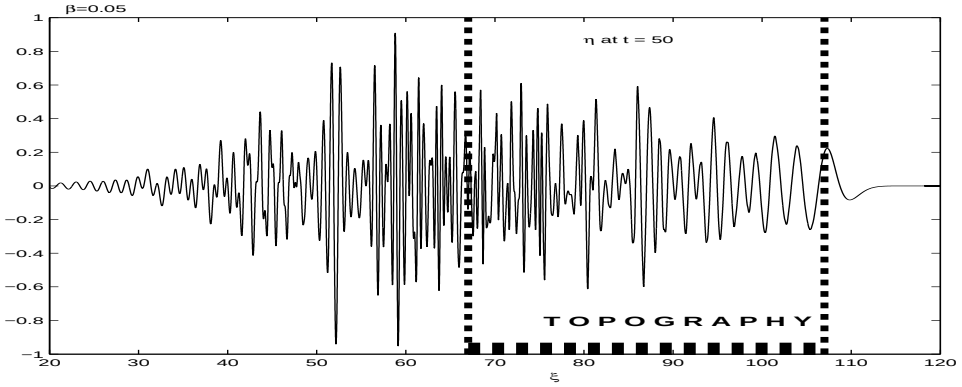


FIG. 5.6. *An example of the entire wave profile, computed from the potential theory equations (5.25)-(5.28).*

agree even better. In figure 5.8 we compare the solution of equations (5.25)-(5.28) to the solution of the model (1.30)-(1.31) for the optimal value of the depth parameter $Z_0 = 0.469$. The numerical parameters for the model equations are the same as in the previous experiment. The corresponding solutions of the two models agree with even better accuracy.

An additional experiment (figure 5.9) is performed for $Z_o = \sqrt{2/3}$, keeping $\alpha = 0.001$, $\beta = 0.002$. This is the best value for the depth parameter in order to prove theorems regarding solution properties in function space [10, 65]. Nevertheless the comparison with potential theory is not as good as for $Z_0 = 0.469$.

Now we increase the dispersion parameter to $\beta = 0.05$. In figure 5.10 we contrast the solution for equations (5.25)-(5.28) with the solution of model (1.25)-(1.26). We use the same numerical parameters as in the preceding experiments. We take a different realization of the metric coefficient $M(\xi)$ in this set of experiments to show that the results are generic. In this case, the error introduced when the dispersive terms are truncated in the Boussinesq model (1.30)-(1.31) (with $Z_0 = \sqrt{1/3}$) is appreciable.

To contrast with the preceding experiment, in figure 5.11 we compare the solutions for equations (5.25)-(5.28) with those for system (1.30)-(1.31) with $Z_0 = 0.469$. For this particular value of the depth parameter $Z_0$, the smaller relative error in phase velocity for the models considered makes the difference. Now, the solutions agree well inside the region [67,107] where the fluctuations of the topography are located. This experiment provides strong evidence that the new Boussinesq formulation (1.30)-(1.31) (with $Z_0 = 0.469$) enables an improved prediction for the pulse reflection with

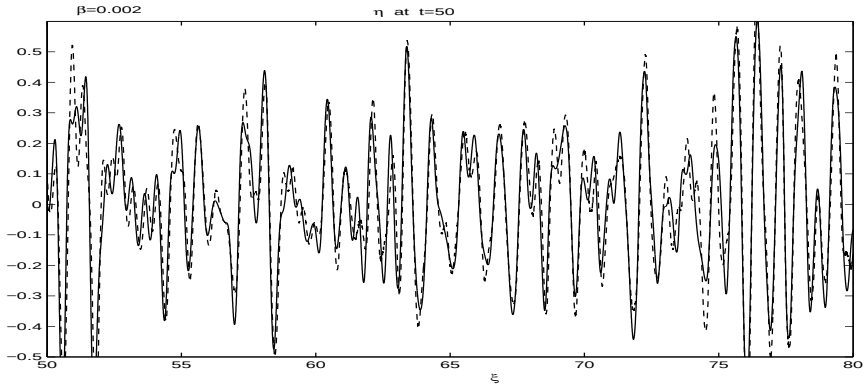


FIG. 5.7. *Dashed line: Numerical solution of the terrain-following system (1.25)-(1.26). Model parameters:* $\alpha = 0.001$, $\beta = 0.002$. *Solid line: Numerical solution of the equations (5.25)-(5.28). Model parameters:* $\alpha = 0$, $\beta = 0.002$.

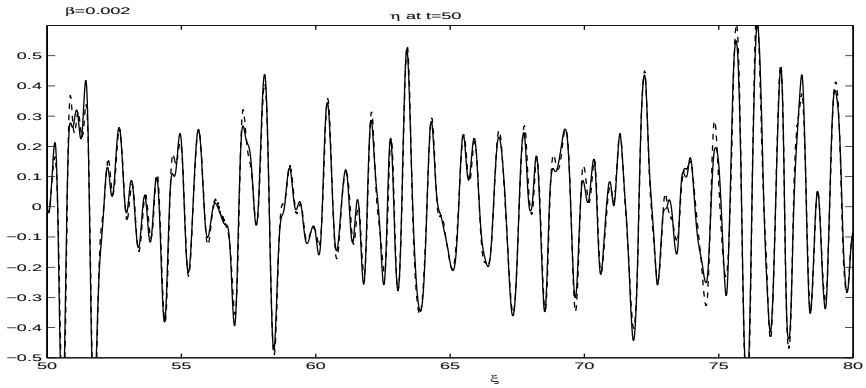


FIG. 5.8. *Dashed line: Numerical solution of the Boussinesq system (1.30)-(1.31). Model parameters:* $\alpha = 0.001$, $\beta = 0.002$, $Z_0 = 0.469$. *Solid line: Numerical solution of the equations (5.25)-(5.28). Model parameters:* $\alpha = 0$, $\beta = 0.002$.

respect to the terrain-following system (1.25)-(1.26). This behaviour was observed systematically in several numerical experiments performed for different levels of the dispersion parameter $\beta$.

Finally consider the (optimal $L^2$ norm) value $Z_o = \sqrt{1/5} = 0.447$. This value is no that different from 0.469. Nevertheless some differences in the highly fluctuating part of the scattered signal can be noticed (c.f. figure 5.12).

**5.5. Waveform inversion by time reversal refocusing.** Time-reversal experiments can be performed for the transmitted (TRT) or for the reflected (TRR) signal as schematically indicated in figure 5.13. The transmitted (or reflected signal) is recorded at the corresponding extreme of the inhomogeneous medium. The data is time reversed and sent back into the same medium through the exact same model. By *time reversion* it is meant that information recorded last is sent out first. In other words the recorded signal is used as a new initial data, for *the same system* of partial differential equations, but it is propagated backwards into the (same) inhomogeneous medium, as indicated in figure 5.13. Much mathematical and experimental work has

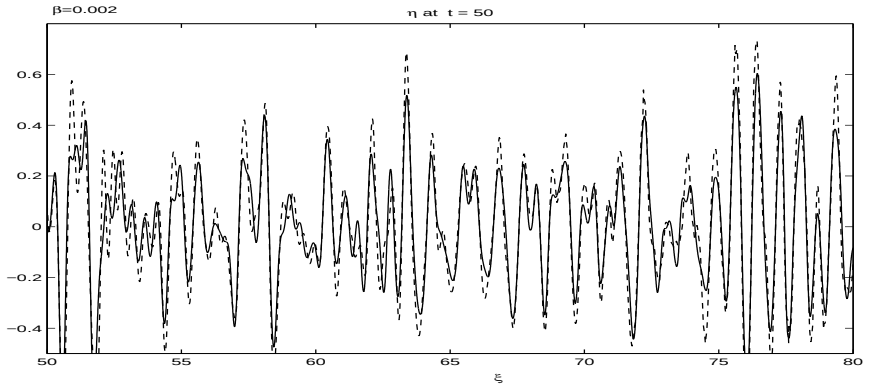


FIG. 5.9. *Dashed line: Numerical solution of the system (1.35)-(1.36). Model parameters:* $\alpha = 0.001$, $\beta = 0.002$, $Z_o = \sqrt{2/3}$. *Solid line: Numerical solution of the equations (5.25)-(5.28). Model parameters:* $\alpha = 0$, $\beta = 0.002$.

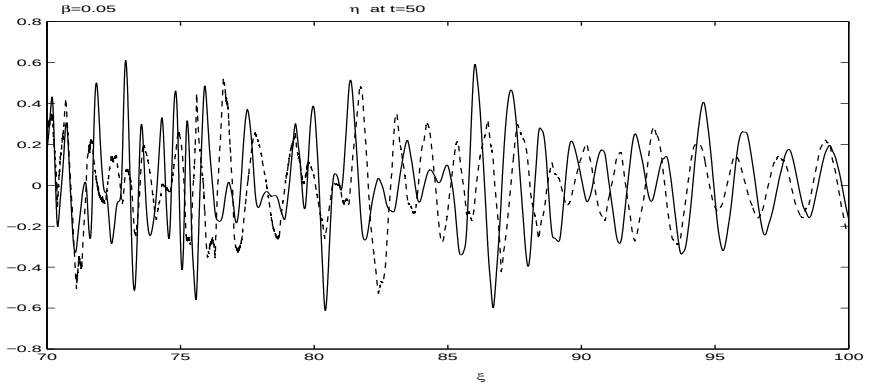


FIG. 5.10. *Dashed line: Numerical solution of the terrain-following system (1.25)-(1.26). Model parameters:* $\alpha = 0.001$, $\beta = 0.05$. *Model parameters:* $\alpha = 0.001$, $\beta = 0.05$. *Solid line: Numerical solution of the equations (5.25)-(5.28). Model parameters:* $\alpha = 0$, $\beta = 0.05$.

been done showing that this process leads to the recompression of the noisy signal into the original pulse shape. In particular laboratory experiments were done for acoustic waves [25]. For mathematical details please consult [52, 28, 31] and the references therein, which include several leading work by Papanicolaou and collaborators. One of our recent goals has been to study the time-reversal refocusing for solitary waves. In previous work, we have mathematically analysed the effect of dispersion [28] and the effect of nonlinearity [29] separately. Nevertheless only recently Garnier, Muñoz and Nachbin (manuscript) have derived a theory for the time-reversed refocusing of solitary waves. Numerical simulations with solitary waves have been presented in [52, 30] and are further explored in the present paper through the improved Boussinesq model.

Regarding applications in water waves, the problem of waveform inversion has been studied by adjoint methods as in Pires and Miranda [64] and the references within. Their goal is to characterize the initial sea surface displacement due to tsunamigenic earthquakes. In other words one would like to recover (numerically) relevant details of a tsunami source from tidal gauge observations. In our case, instead of performing the backward numerical integration for the corresponding adjoint

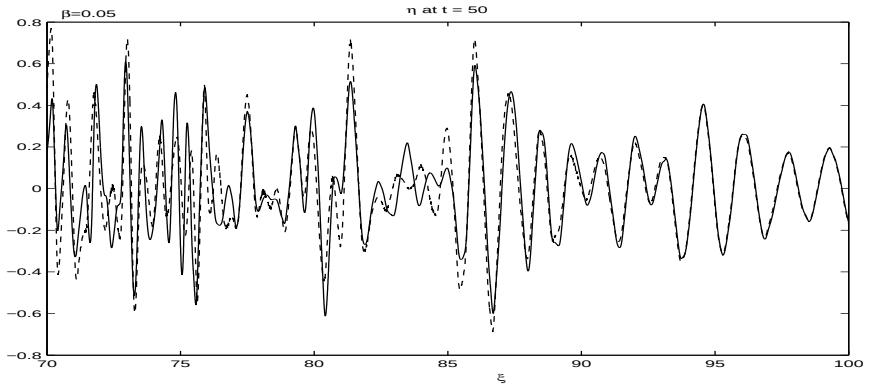


FIG. 5.11. *Dashed line: Numerical solution of system (1.30)-(1.31) with* $Z_0 = 0.469$. *Model parameters:* $\alpha = 0.001$, $\beta = 0.05$. *Solid line: Numerical solution of the equations (5.25)-(5.28) . Model parameters:* $\alpha = 0$, $\beta = 0.05$.

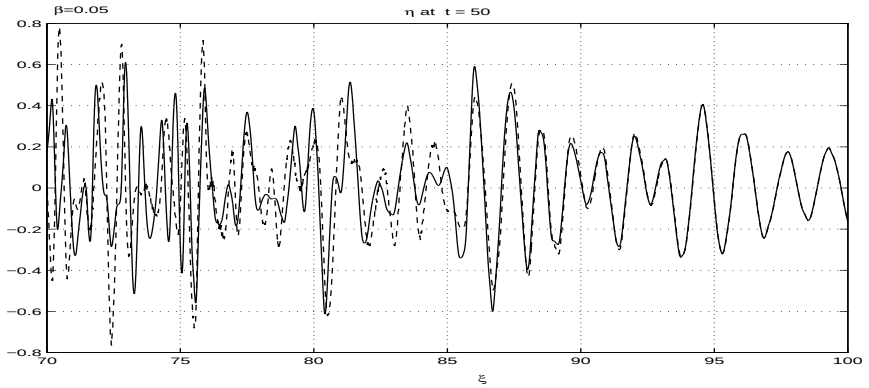


FIG. 5.12. *Dashed line: Numerical solution of the system (1.30)-(1.31) with* $Z_0 = \sqrt{1/5}$. *Model parameters:* $\alpha = 0.001$, $\beta = 0.05$. *Solid line: Numerical solution of the equations (1.19)-(1.22). Model parameters:* $\alpha = 0$, $\beta = 0.05$.

equations, we use the (same) forward numerical model but with the time-reversed data as explained above. Waveform inversion is obtained through the time-reversed refocusing effect. The advantage regarding time-reversal methods is for nonlinear problems. For adjoint methods there are technical difficulties involved with nonlinearity as reported by Pires and Miranda [64].

The purpose of this section is to illustrate the refocusing phenomenon, now in the case of the system (1.30)-(1.31) with the optimal depth $Z_0 = 0.469$. We also present time reversal simulations with the potential theory equation. We note that this has never been done before until recently in [53]. The goal is to observe the improved waveform inversion procedure in comparison with earlier experiments. Namely, up to now, all the dispersive time reversal refocusing experiments were performed for the depth-averaged Boussinesq system, which amounts to $Z_0 = \sqrt{1/3}$ [52, 28, 30]. In addition, we will further explore the refocusing of solitary waves, for different values of the amplitude of the topography fluctuations and of the correlation length of the irregularities.

Throughout this section, the numerical parameters for equations (5.25)-(5.28) are

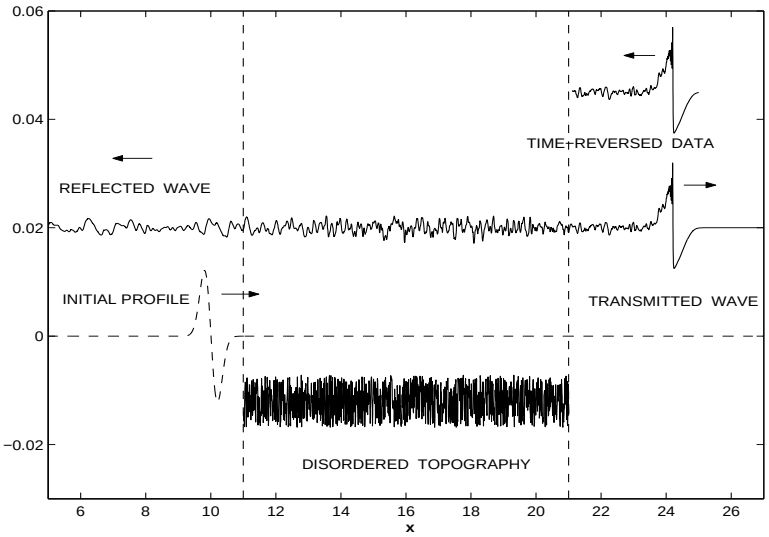


FIG. 5.13. *Schematic figure for time reversal simulations.*

$\Delta t = 0.01$, $2^{12}$ FFT points in space and the computational domain is [0,150]. The numerical parameters for systems (1.25)-(1.26) and (1.30)-(1.31) are $\Delta\xi = 0.024$, $\Delta t = 0.0125$ and the computational domain is [0,120].The irregularities of the coefficient $M(\xi)$ are located in the interval [67,107] and again $\delta = 0.5$ and $\ell = 0.1$.

**5.5.1. TRR refocusing of Gaussian pulses.** The first experiment uses $\beta = 0.002$ and $\alpha = 0.001$ indicating a weakly dispersive, effectively linear regime. The pulses are the same as before, namely

$$\Phi(\xi, 1, 0) = \Phi_0(\xi) = e^{-20(\xi-60)^2},$$
$$\eta(\xi, 0) = \eta_0(\xi) = -40(\xi - 60)e^{-20(\xi-60)^2}.$$

Note that for a time-reversal in reflection (TRR) experiment we only record the reflected signal, recorded to the left of the topography (c.f. figure 5.13). Hence this fluctuating signal has no indication whatsoever of the original pulse shape, say as opposed to the transmitted wave. These fluctuating signals (for $\eta$ and $u$) are sent back into the inhomogeneous medium and by the refocusing phenomenon they recompress into a (reduced) copy of their initial pulse shapes.

We emphasize that the pulse shape is exactly the same [28]: in the present experiment it is the derivative of a Gaussian as shown in figure 5.14. In figure 5.14 the refocused pulse obtained from model (5.25)-(5.28) is superimposed to the one obtained from system (1.25)-(1.26). Observe that the refocused pulses obtained from both models agree with very good accuracy and that they are derivatives of a Gaussian (as expected) of a reduced amplitude. The reduction in amplitude is intuitive since there is a nontrivial amount of energy being transmitted to the other side of the topography. Hence TRR recompresses only a fraction of the initial energy [30].

In an analogous way, in figure 5.15 we observe that the refocused pulse obtained with the model (1.19)-(1.22) coincides to that of system (1.30)-(1.31) with $Z_0 = 0.469$. This is expected since the dispersion level is low ($\beta = 0.002$).

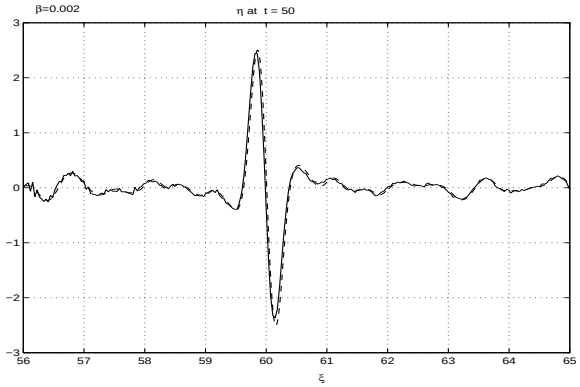


FIG. 5.14. *In solid line: TRR refocusing for system (5.25)-(5.28). Model parameters:* $\alpha = 0$, $\beta = 0.002$. *In dashed line: TRR refocusing for system (1.25)-(1.26). Model parameters:* $\alpha = 0.001$, $\beta = 0.002$.

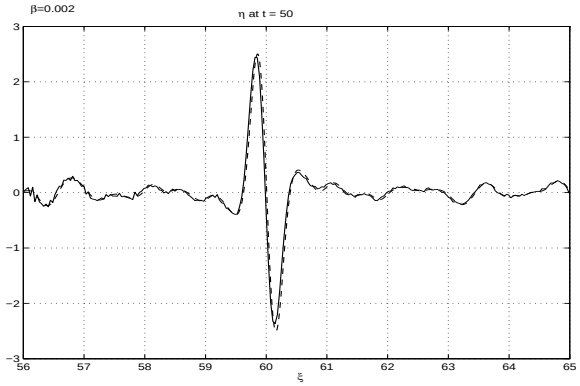


FIG. 5.15. *In solid line: TRR refocusing for system (5.25)-(5.28). Model parameters:* $\alpha = 0$, $\beta = 0.002$. *In dashed line: TRR refocusing for system (1.30)-(1.31). Model parameters:* $\alpha = 0.001$, $\beta = 0.002$, $Z_0 = 0.469$.

In the second experiment we increase the level of dispersion by a factor of 25 ($\beta = 0.05$). Again we adopt a different realization of the coefficient $M(\xi)$ in this experiment to show that the results are generic. In figure 5.16 we compare the refocused pulse obtained with model (5.25)-(5.28) with that of system (1.25)-(1.26). Now observe that the corresponding solutions are quit different. In particular, the relative error in the pulses' peaks is roughly 40 percent.

In figure 5.17 we compare the refocused pulse obtained with the model (5.25)-(5.28) to that of system (1.30)-(1.31) with $Z_0 = 0.469$. In contrast with the previous experiment, observe that the Boussinesq prediction agrees very well at the pulses' peak and even along the fluctuating part of the signal. The TRR refocusing phenomenon highlights, in a quite dramatic fashion, the improvements of the Boussinesq system: waveform inversion with another Boussinesq system (as the one we used in [28, 30]) can **underestimate**, say, the **initial amplitude of a tsunami** [64]. It is important to say that the theory and computations in [28, 30] were correct but, as shown here and in [53], done with a restrictive model. The TRR refocusing phenomenon also works well for $Z_0 = \sqrt{1/5}$.

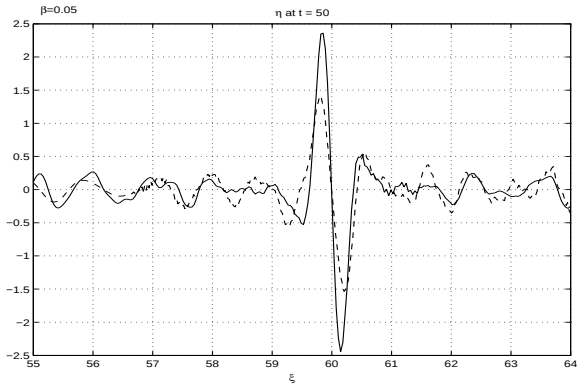


FIG. 5.16. *In solid line: TRR refocusing for system (1.19)-(1.22). Model parameters:* $\alpha = 0$, $\beta = 0.05$. *In dashed line: TRR refocusing for system (1.25)-(1.26). Model parameters:* $\alpha = 0.001$, $\beta = 0.05$.

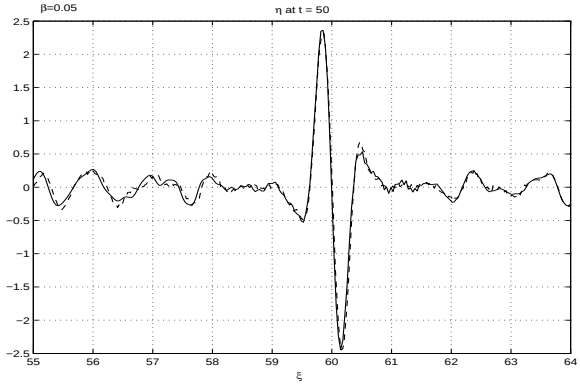


FIG. 5.17. *In solid line: TRR refocusing for system (1.19)-(1.22). Model parameters:* $\alpha = 0$, $\beta = 0.05$. *In dashed line: TRR refocusing for system (1.30)-(1.31). Model parameters:* $\alpha = 0.001$, $\beta = 0.05$, $Z_0 = 0.469$.

**5.5.2. TRT refocusing of Gaussian pulses.** We now perform TRT as schematically indicated in figure 5.13. In this case usually we observe a leading wavefront followed by a fluctuating coda. The fluctuating coda consists of a dispersive tail as well as of a disordered component, generated due to the forward scattering. This can be clearly seen in figure 5.6 where the smooth (Airy-like) wavefront is about to leave the region where the topography is located. The wavefront, the dispersive tail and the disordered coda are all recorded to the right of the topography. We set $\beta = 0.05$. The numerical parameters for the potential theory equations(5.25)-(5.28) are $\Delta t = 0.01$, $2^{13}$ FFT points in space and the computational domain is [0,290]. The numerical parameters for systems (1.25)-(1.26) and (1.30)-(1.31) are $\Delta t = 0.013$, $\Delta\xi = 0.029$ and the computational domain is [0,290]. The initial conditions for equations (1.19)-(1.22) are

$$\Phi(\xi, 1, 0) = \Phi_0(\xi) = e^{-20(\xi-150)^2},$$
$$\eta(\xi, 0) = \eta_0(\xi) = -40(\xi - 150)e^{-20(\xi-150)^2}.$$

Observe that the initial pulses are located at the position $\xi = 150$. We recall that the corresponding initial velocity at the level $Z_0$ for systems (1.25)-(1.26) and (1.30)-(1.31) is calculated from equation (5.34).

In figure 5.18 we compare the refocused pulse obtained with the model (5.25)-(5.28) to the one obtained with system (1.25)-(1.26). In figure 5.19 we compare the refocused pulse obtained with potential theory to that of system (1.30)-(1.31) with $Z_0 = 0.469$. One can see some improvement. The improvement for TRT is not so dramatic as for TRT. The reason is that for TRT the bulk of the energy is still contained in the leading wavefront. In other words most of energy resides on low wavenumbers and therefore the dispersive effects are less noticeable.

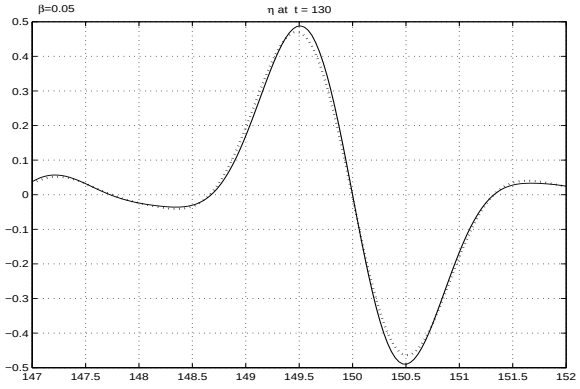


FIG. 5.18. *In solid line: TRT refocusing for system (5.25)-(5.28). Model parameters:* $\alpha = 0$, $\beta = 0.05$. *In dashed line: TRT refocusing for system (1.25)-(1.26). Model parameters:* $\alpha = 0.001$, $\beta = 0.05$.

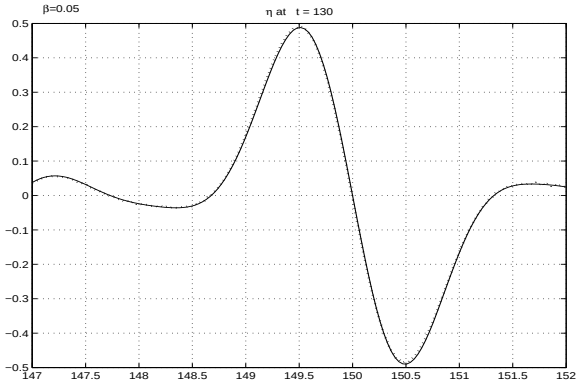


FIG. 5.19. *In solid line: TRT refocusing for system (5.25)-(5.28). Model parameters:* $\alpha = 0$, $\beta = 0.05$. *In dashed line: TRT refocusing for system (1.30)-(1.31). Model parameters:* $\alpha = 0.001$, $\beta = 0.05$, $Z_0 = 0.469$.

**5.5.3. TRR refocusing for solitary waves.** In this section we analyze the refocusing property for solitary waves of system (1.30)-(1.31). Recall that equation (5.9) furnishes a solitary wave solution for a second order Boussinesq-type equation formally equivalent to equations (1.30)-(1.31). The length scale for the irregularities of the coefficient $M(\xi)$ is $\ell = 0.6$ because the effective support of the solitary wave

(5.9) is $\ell_p = 6$. Thus, we preserve the ratio $\gamma = \ell/\ell_p = 1/10$. The initial solitary wave is located at the position $\xi = -5$. The amplitude of the irregularities is $\delta = 0.5$. The irregularities of the metric coefficient $M(\xi)$ are in the interval [5,305]. In this set of experiments, the numerical parameters are $\Delta t = 0.0375$, $\Delta\xi = 0.04266$, and the computational domain is [-320,320].

In the first experiment we adopt $\alpha = \beta = 0.01$. Just as for the Gaussian pulse we record the reflected signal to the left of the topography. We time reverse the data and use it as the initial condition for the exact same problem. This time reversed fluctuating data travels towards the rough region and, after interacting with the topography, it recompresses into the smooth pulse shown at the center of figure 5.20. There is no theory to tell us what kind of pulse we are seeing after refocusing. It is not clear that we have a reduced copy of the solitary wave.

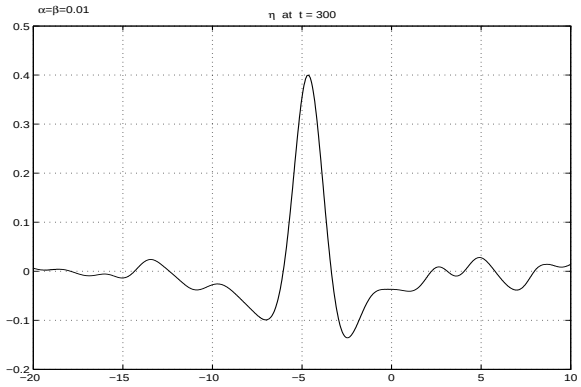


FIG. 5.20. *TRR refocusing of the solitary wave (5.9) of the system (1.30)-(1.31) with* $Z_0 = 0.469$. *Numerical parameters:* $\alpha = \beta = 0.01$.

In the second experiment we repeat the previous experiment but now we set $\alpha = \beta = 0.03$. This experiment is more dispersive and nonlinear than the previous one. The refocused pulse is presented in figure 5.21 and very much resembles the previous case. The phenomenon is robust regarding the dispersion and nonlinearity levels.

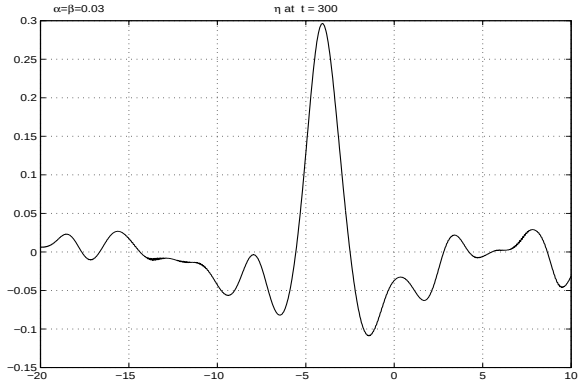


FIG. 5.21. *TRR refocusing of the solitary wave (5.9) of the system (1.30)-(1.31) with* $Z_0 = 0.469$. *Numerical parameters:* $\alpha = \beta = 0.03$.

Now we vary some other parameters related to the propagation medium (i.e. topography) rather than the wave. We repeat the previous experiment (keeping $Z_o = 0.469$) but now with a smaller fluctuation level: $\delta = 0.25$. This implies in a weaker reflected signal. A plausible question is to whether the weak reflected signal will contain enough energy to produce a well defined refocused pulse. The answer is clearly seen in figure 5.22 where we have a clean refocused pulse, but of a smaller amplitude (since it contains less energy).

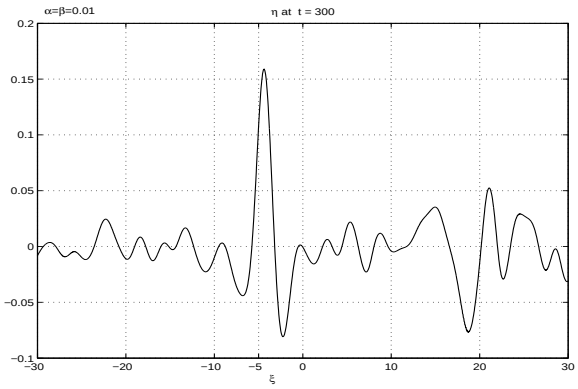


FIG. 5.22. *TRR refocusing of the solitary wave (5.9) of system (1.30)-(1.31) with* $Z_o = 0.469$. *Model's parameters:* $\alpha = \beta = 0.01$, *fluctuation level* $\delta = 0.25$.

Next we change the correlation length adopted to be $\ell = 0.3$, which is half of that in the previous experiments. Now the topography is even more rapidly varying and long waves can not feel it in detail. The amplitude of fluctuations is back to $\delta = 0.5$. Observe that the amplitude of the refocused pulse is approximately 30% of the initial solitary wave (5.9). Compare with figure 5.20 where ($\ell = 0.6$, $\delta = 0.5$) and the refocused pulse amplitude was at the 40% level. As mentioned above, here the topography is on an even finner scale, so that the solitary wave feels less the details and therefore sheds less reflection.

The important fact about all these experiments is that the refocusing phenomenon is very robust for solitary waves.

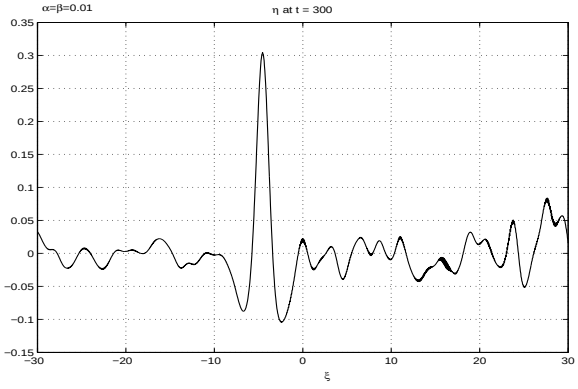


FIG. 5.23. *TRR refocusing of the solitary wave (5.9) of system (1.30)-(1.31) with* $Z_o = 0.469$. *Model's parameters:* $\alpha = \beta = 0.01$.

## Appendix A. Solutions for the linear KdV equation and the linear Boussinesq model.

### The linear KdV equation

Consider the initial value problem

$$u_t + u_x + \gamma u_{xxx} = 0, \tag{A.1}$$

$$u(x,0) = f(x), \tag{A.2}$$

where $\gamma$ is a nonzero constant. Using Fourier transform in $x$ the solution for equations (A.1) and (A.2) is given by

$$u(x,t) = \frac{1}{2\pi}\int_{-\infty}^{\infty}\left(\int_{-\infty}^{\infty} e^{i(k(x-t-y)+\gamma k^3 t)}dk\right) f(y)dy. \tag{A.3}$$

Making a convenient change of variables, the inner integral in equation (A.3) can be expressed in terms of the Airy function to give

$$u(x,t) = \frac{1}{(3t\gamma)^{1/3}}\int_{-\infty}^{\infty} \mathrm{Ai}\left(\frac{x-t-y}{(3t\gamma)^{1/3}}\right) f(y)dy. \tag{A.4}$$

The Airy-kernel gives the rate in time at which a pulse $f(x)$ will spread due to dispersion. This is an useful information for the invariant imbedding technique used in the O'Doherty-Anstey theory.

### The linear Boussinesq model

Now we study the linearization of system (3.27) for constant depth:

$$\begin{aligned} &\eta_t + u_\xi = 0, \\ &u_t + \eta_\xi - \frac{\beta}{3}u_{\xi\xi t} = 0, \end{aligned} \tag{A.5}$$

with the initial conditions

$$\eta(\xi,0) = u(\xi,0) = f(\xi).$$

Analogously to the KdV equation we can apply the Fourier transform technique to obtain the Fourier coefficients

$$\begin{aligned} \hat{\eta}(k,t) = \frac{\hat{f}(k)}{2}\Big[&\left(1-\sqrt{1+(\beta/3)k^2}\right)e^{\frac{ikt}{\sqrt{1+\beta/3k^2}}} + \\ &\left(1+\sqrt{1+(\beta/3)k^2}\right)e^{\frac{-ikt}{\sqrt{1+\beta/3k^2}}}\Big], \end{aligned} \tag{A.6}$$

$$\begin{aligned} \hat{u}(k,t) = \frac{\hat{f}(k)}{2\sqrt{1+(\beta/3)k^2}}\Big[&\left(1+\sqrt{1+(\beta/3)k^2}\right)e^{\frac{-ikt}{\sqrt{1+\beta/3k^2}}} \\ &-\left(1-\sqrt{1+(\beta/3)k^2}\right)e^{\frac{ikt}{\sqrt{1+\beta/3k^2}}}\Big]. \end{aligned} \tag{A.7}$$

We point out that in the hyperbolic case ($\beta = 0$) the above initial data gives rise to (only) a right propagating mode. In the dispersive case a negligible left propagating mode is always present in this type of data. Notice that because of (A.6), (A.7) and

$$\frac{1}{\sqrt{1+(\beta/3)k^2}} = 1 - (k^2/6)\beta + O(\beta^2),$$

we have that

$$\widehat{L}(t,k) = \hat{\eta}(t,k) - \hat{u}(t,k) = O(\beta) \approx 0,$$

provided that $\beta$ is small enough. For the hyperbolic case the left propagating mode is identically zero.

The dispersion relation for system (A.5) is

$$\omega_\pm = \omega_\pm(k) = \pm \frac{k}{\sqrt{1+\frac{\beta}{3}k^2}}, \tag{A.8}$$

where $\omega_+$ and $\omega_-$ represent Fourier modes propagating to the right and left, respectively. In opposition to the KdV equation the phase velocity is

$$C_k^\pm = \frac{\omega_\pm}{k} = \pm \frac{1}{\sqrt{1+\frac{\beta}{3}k^2}},$$

which does not switch signs and is bounded by one. Furthermore, $\omega_+ = \omega_+(k)$ coincides up to $O(k^3)$ with the dispersion relation for the KdV equation above with $\gamma = \beta/6$. Note also that, for waves generated in space, the range of possible time frequencies is bounded by $(3/\beta)^{1/2}$ for all $k$. As a consequence, solutions $u, \eta$ of system (A.5) are band-limited functions in $t$. This fact justifies why frequencies $\omega$ higher than $\sqrt{3/\beta}$ are not considered in the analysis presented in section 3.3.

**Appendix B. Computation of coefficients $a_\beta(x_o,\omega)$ and $b(x_o,\omega)$.** As mentioned in section 3.3, the numerical computation of the dispersive coefficient $a_\beta(x_o,\omega)$ is expensive. To override this difficulty we approximated it by the hyperbolic medium's correlation function $a_0(x_o,\omega)$, which corresponds to the leading order term of a Taylor series expansion of $a_\beta$ around $\beta = 0$. The numerical experiments in section 3.4 showed the high accuracy of this approximation.

To compute coefficient $a_0(x_o,\omega)$ as in equation (3.25) we rewrite it as

$$a_0(x_o,\omega) = \int_0^X \Phi(\eta) e^{-2i\omega\eta} d\eta, \tag{B.1}$$

where

$$\Phi(\eta) = \frac{1}{x_o}\int_0^{x_o} r(x)r(x+\eta)dx.$$

We know by the correlation theorem that

$$\int_{-\infty}^{\infty} r(x)r(x+\eta)dx = F^{-1}[\hat{r}\overline{\hat{r}}](\eta),$$

where the hat denotes the Fourier transform, $F^{-1}$ the inverse Fourier transform and the bar indicates complex conjugation. Therefore function $\Phi$ defined above can be

computed by using the FFT algorithm letting the coefficient $r(x)$ be zero outside the interval $[0, x_o]$. This is consistent with the invariant imbedding approach. We must append enough zeros to the tail of the sampled coefficient $r(x)$ (zero padding) in order to eliminate the overlapping phenomenon that appears due to the fact that $r(x)$ is not a periodic function. The Fast Fourier transform (FFT) assumes periodicity in both physical and frequency domains (see Brigham [14]). The cost of computing the discrete correlation function results in only three FFT evaluations which is faster than an ordinary computation of the integral defining $\Phi$ for each value of $\eta$. The numerical code to perform the discrete correlation can be found in [14].

Once the function $\Phi$ is known, the windowed Fourier transform in equation (B.1) is evaluated by using only one FFT. Analogously to the discrete correlation zero padding outside the inverval $[0, X]$ is required on the sampling of function $\Phi$.

To evaluate the generalized O'Doherty-Anstey approximation presented in section 3.3 we also need the dispersive coefficient $b(x_o, \omega)$. To make its computation faster we rewrite it in the more compact form

$$b(x_o,\omega) = -\frac{\beta}{6x_o}\int_0^{\xi(x_o)} \frac{-i\omega^3 M^{3/2}(\xi) + M'(\xi)\omega^2}{1-(\beta/3)M(\xi)\omega^2} d\xi, \tag{B.2}$$

where the upper limit $\xi(x_o)$ denotes the spatial position in the medium corresponding to the travel time $x_o$. Thus we must compute only once the coefficients $M(\xi)$, $M^{3/2}(\xi)$ and $M'(\xi)$ which can be stored at the beginning. The integral in (B.2) is approximated by the trapezoidal method for roughly $2^{14}$ frequencies in the range $|\omega| < C_o(x_o)\sqrt{3/\beta}$. Since $b(x_o, -\omega) = \overline{b(x_o, \omega)}$ only positive frequencies must be evaluated.

## REFERENCES


[1] M. Abramowitz and I. Stegun, *Handbook of mathematical functions* (Dover, New York, 1965).

[2] W. Artiles and A. Nachbin, *Nonlinear evolution of surface gravity waves over highly variable depth*, Phys. Rev. Lett., Vol. 93 (2004), 234501.

[3] W. Artiles and A. Nachbin, *Asymptotic nonlinear wave modeling through the Dirichlet-to-Neumann operator*, Meth. Appl. Anal., Vol. 11, No. 3 (2004), pp. 1-18.

[4] M. Asch, W. Kohler, G. C. Papanicolaou, M. Postel and B. White, *Frequency content of randomly scattered signals*, SIAM Review, V 33, (1991) pp. 519-625.

[5] P.G. Baines, *Topographic Effects in Stratified Flows*, Cambridge Univ. Press, 1995.

[6] T.B. Benjamin, J.L. Bona and J.J. Mahony, *Model equations for long waves in nonlinear dispersive systems*, Phil. Trans. Roy. Soc., **A272** (1972), pp. 47-78.

[7] K.M. Berger and P.A. Milewski, *Simulation of wave interactions and turbulence in one-dimensional water waves*, SIAM J. Appl. Math., Vol. 63, No. 4 (2003), pp. 1121-1140.

[8] L. Berlyand and R. Burridge, *The accuracy of the O'Doherty-Anstey approximation for wave propagating in highly disordered stratified media,* Wave Motion 21 (1995), pp. 357-373.

[9] J.L. Bona and M. Chen, *Comparison of model equations for small-amplitude long waves*, Nonlinear Analysis,38 (1999), pp. 625-647.

[10] J.L. Bona, M. Chen and J.C. Saut, *Boussinesq Equations and other systems for small-amplitude long waves in nonlinear dispersive media. I: Derivation and linear theory.* J. Nonlinear Science, Vol. 12 (2002), pp. 283-318.

[11] R. Burridge, G. Papanicolaou, and B. White, Statistics for pulse reflection from a randomly layered medium, SIAM J. Appl. Math. **47** (1987) pp. 146-168.

[12] R. Burridge, G.C. Papanicolaou and B.S. White, *One dimensional wave propagation in a highly discontinuous medium.* Wave Motion, 10(1988), pp. 19-44.

[13] R. Burridge and H.W. Chang, *Multimode, one-dimensional wave propagation in a highly discontinuous medium.* Wave Motion 11 (1989), pp. 231-249.

[14] E.O. Brigham, *The Fast Fourier Transform and its Applications*, Prentice Hall, 1988.

[15] J.G.B. Byatt-Smith, *An integral equation for unsteady surface waves and a comment on the Boussinesq equation*, J. Fluid Mech., **Vol. 49** (1971), pp. 625-633.
[16] J.F. Clouet and J. P. Fouque, *Spreading of a pulse travelling in random media.*, Annals of Applied Probability, V 4, (1994) pp. 1083-1097.
[17] J.F. Clouet and J.P. Fouque, A time-reversal method for an acoustical pulse propagating in randomly layered media, Wave Motion **25** (1997), pp. 361-368.
[18] W. Craig and C. Sulem, *Numerical simulation of gravity waves*, J. Comput. Phys., **108** (1993), pp. 73-83.
[19] R. Dean and R.A. Dalrymple, *Water Waves Mechanics for Engineers and Scientists*, World Scientific, 3rd. ed., 1993.
[20] P.G. Drazin and R.S. Johnson, *Solitons: an introduction*, Cambridge University Press, (1989).
[21] T. Driscoll, http://www.math.udel.edu/driscoll/software.
[22] T. Driscoll and L.N. Trefethen, *Schwarz-Christoffel Mapping*, Cambridge Univ. Press, 2002.
[23] European Centre for Medium-Range Weather Forecasts (ECMWF),*Orography*, Proceedings of a Workshop held at ECMWF, 1998.
[24] B. Engquist and A. Majda, *Absorbing boundary conditions for the numerical simulation of waves,* Math. Comp., 31 (139) (1977), pp. 629-651.
[25] M. Fink, *Time reversal mirrors*, J. Phys. D: Appl. Phys., 26 (1993), pp. 1333-1350.
[26] M. Fink, Time reversed acoustics, Scientific American (November 1999) pp. 91-97.
[27] J.P. Fouque, and A. Nachbin, *Time-reversed refocusing of surface water waves.* SIAM Multiscale Modeling and Simulation, Vol. 1, No. 4 (2003), pp. 609-629.
[28] J.P. Fouque, J. Garnier. and A. Nachbin, *Time reversal for dispersive waves in random media*, SIAM J. Appl. Math. Vol., 64, No. 5 (2004), pp. 1810-1838.
[29] J.P. Fouque, J. Garnier, and A. Nachbin, *Shock structure due to stochastic forcing and the time reversal of nonlinear waves*, Physica D, vol. 195 (2004), pp. 324-346.
[30] J.P. Fouque, J. Garnier, J.C. Muñoz, and A. Nachbin, *Time reversing solitary waves.* Phys. Rev. Lett. 92, No. 9 (2004), 094502-1.
[31] J.P. Fouque, J. Garnier, G.C. Papanicolaou and K. Sølna, *Wave Propgation and Time Reversal in Randomly Layered Media*, Springer-Verlag, to appear (2006).
[32] J. Garnier, *Long-time dynamics of Korteweg-de Vries solitons driven by random perturbations*, J. Stat. Phys., Vol. 105 (2001), pp. 789-833.
[33] J. Garnier, *Exponential localization versus soliton propagation*, Proceedings of the conference *Nonlinearity and Disorder*, NATO Science Series II, Vol. 45, (2002) pp. 3-17, Kluwer.
[34] J. Garnier and A. Nachbin, *The eddy viscosity for time reversing waves in a dissipative environment*, Phys. Rev. Lett., Vol. 93, No. 15 (2004), 154501.
[35] P. Guidotti, *A first-kind boundary integral formulation for the Laplace Dirichlet-to-Neumann map in 2D*, J. Comput. Phy., **190** (2003), pp. 325-345.
[36] J. Hamilton, *Differential equations for long-period gravity waves on a fluid of rapidly vaying depth,* J. Fluid Mech., 83 (1977), pp. 289-310.
[37] T.Y. Hou, J. Lowengrub and M. Shelley, Removing the Stiffness from Interfacial Flows with Surface Tension , J. Comput Phys. , 114 (1994), pp. 312-338.
[38] R.Z. Khasminskii, On stochastic processes defined by differential equations with a small parameter, *Theory Probab. Appl.* **11** (1966), pp. 211-228.
[39] J.B. Keller, *Shallow-water theory for arbitray slopes of the bottom*, J. Fluid Mech., **Vol. 489** (2003), pp.345-348.
[40] A.B. Kennedy, J.T. Kirby, Q. Chen and R.A. Dalrymple, (2001) *Boussinesq-type equations with improved nonlinear performance*, Wave Motion, 33, pp. 225-243.
[41] P. Lewicki, R. Burridge and M. de Hoop, *Beyond effective medium theory: Pulse stabilization for multimode wave propagation in high-contrast layered media,* SIAM J. Appl. Math., 56, No. 1 (1996), pp. 256-276.
[42] P. Lewicki, R. Burridge, and G. Papanicolaou, Pulse stabilization in a strongly heterogeneous medium, Wave Motion **20** (1994) 177-195.
[43] P.L.-F. Liu and J.A. Liggett, *Boundary element formulations and solutions for some nonlinear water wave problems*, Developments in Boundary Element Methods -2, Chap. 3, eds. P.K. Banerjee and R.P. Shaw (1984), Elsevier Applied Science Publishers.
[44] P.A. Madsen, R. Murray and O.R. Sørensen, *A new form of the Boussinesq equations with improved linear dispersion characteristics (Part1). Coastal Engineering*, 15 (1991), pp. 371-388.
[45] P.A. Madsen and O.R. Sørensen, *A new form of the Boussinesq equations with improved linear dispersion characteristics, Part 2: A slowly-varying bathymetry.* Coastal Engineering,

18(1992), pp. 183-205.
[46] Y. Matsuno, *Nonlinear evolution of surface gravity waves on fluid of finite depth*, Phys. Rev. Lett., **Vol. 69**, No. 4 (1992), 609.
[47] F. Mattioli, *Decomposition of the Boussinesq Equations for Shallow-Water into a set of Coupled Korteweg-de Vries Equations,* Phys. Fluids A 3 (10) (1991), pp. 2355-2359.
[48] F. Mattioli, *On the Hamiltonian Decomposition of the Boussinesq Equations in a pair of Coupled Korteweg-de Vries Equations,* Wave Motion, 28 (1998), pp.283-296.
[49] C.C. Mei, *The Applied Dynamics of Ocean Surface Waves*, (1983) John Wiley.
[50] G. Meyer, *Initial Value Methods for Boundary Value Problems: Theory and Application of Invariant Imbedding*, Academic Press, 1973.
[51] J.C. Muñoz Grajales and A. Nachbin, (2004) *Dispersive wave attenuation due to orographic forcing*. SIAM J. Appl. Math., 64, No. 3, pp. 977-1001.
[52] J.C. Muñoz Grajales and A. Nachbin,(2005) *Stiff Microscale forcing and solitary wave refocusing*. SIAM Multiscale Modeling and Simulation, Vol. 3, No. 3, pp. 680-705.
[53] J.C. Muñoz Grajales and A. Nachbin,(2005) *Improved Boussinesq-type equations for highly-vrible depths*, accepted at the IMA J. Appl. Math.
[54] J.C. Muñoz Grajales, *Dispersive wave attenuation and refocusing due to disordered orographic forcing*, PhD thesis (in english), IMPA, Brazil, 2002.
[55] A. Nachbin, *Modelling of Water Waves in Shallow Channels*. Computational Mechanics Publications, Southampton, U.K., (1993).
[56] A. Nachbin, *The localization length of randomly scattered water waves,* J. Fluid Mech., 296 (1995), pp. 353-372.
[57] A. Nachbin, *A terrain-following Boussinesq system*, SIAM Appl. Math., Vol. 63, No.3 (2003), pp. 905-922, 2003.
[58] A. Nachbin and G.C. Papanicolaou *Water waves in shallow channels of rapidly varying depth*, J. Fluid Mech., Vol. 241 (1992), pp. 311–332.
[59] D.P. Nicholls and F. Reitich, *Stability of high-order pertubative methods for the computation of Dirichlet-Neumann operators*, J. Comput. Phys., **170** (2001), pp. 276-298.
[60] O. Nwogu, *Alternative form of Boussinesq equations for nearshore wave propagation*. J. Waterway, Port, Coastal and Ocean Engineering, 119 (1993), pp. 618-638.
[61] R.F. O'Doherty and N.A. Anstey, *Reflections on amplitudes*, Geophysical Prospecting, V. 19, (1971) pp. 430-458.
[62] G.C. Papanicolaou and K. Sølna, *Ray theory for a locally layered random medium*, Waves in Random Media, V. (2000) pp. 151-198.
[63] D.H. Peregrine, *Long waves on a beach,* J. Fluid Mech., 27 (1967), pp. 815-827.
[64] C. Pires and M.A. Miranda, *Tsunami waveform inversion by adjoint methods*, J. Geophys. Res., vol. 106, No. C9 (2001), pp. 19733–19796.
[65] J.R. Quintero and J.C. Muñoz Grajales, *Existence and uniqueness for a system of Boussinesq equations*. Methods and Applications of Analysis, Vol. 11, No. 1 (2004), pp. 15-32.
[66] R.R. Rosales and G.C. Papanicolaou, Gravity waves in a channel with a rough bottom, Studies in Appl. Math., **68** (1983), pp. 89–102.
[67] H.A. Schäffer and P.A. Madsen, *Further enhancements of Boussinesq-type equations*. Coastal Engineering, 26(1995), pp. 1-14.
[68] M.E. Taylor, *Partial Differential Equations I: Basic Theory*, Springer Verlag, 1996.
[69] G. Wei and J. Kirby, *Time-Dependent Numerical Code for Extended Boussinesq Equations,* J. of Waterway, Port, Coastal, and Ocean Engineering, Vol. 121, No. 5 (1995), pp. 251-261.
[70] G.B. Whitham *Linear and nonlinear waves*, John Wiley, (1974).
[71] Yoon, S.B. and Liu, P.L.F. (1989) *Interaction of currents and weakly nonlinear waves in shallow water*. J. Fluid Mech., 205, pp. 397-419.
[72] V.E. Zakharov, A.I. Dyachenko and O.A. Vasilyev, *New method for numerical simulation of a nonstationary potential flow of incompressible fluid with a free surface*, Euro. J. Mech. B/Fluids, **21** (2002), pp. 283-291.